# General Relativistic Radiative Transfer

Steven Von Fuerst

Mullard Space Science Laboratory
Department of Space and Climate Physics
University College London

A thesis submitted to the University of London
for the degree of Doctor of Philosophy





ProQuest LLC
789 East Eisenhower Parkway
P.O. Box 1346
Ann Arbor, MI 48106-1346

*To*

*everyone*

*for everything*

# Abstract

In this thesis I explore the radiative transfer process where relativistic effects are important. Strong gravity modifies the observable properties of the light emitted by an object. A photon no longer travels in straight lines, and its frequency is shifted as it propagates. Gravitational lensing may make multiple images of the emitter, further modifying the temporal and spectral properties of its emission.

The first part of my thesis investigates the motion of particles in a strong gravitational field (near a black hole). I derive the equations of motion for massive or massless particles acted upon by external forces. Efforts are made to work out self-consistently the structure of the accreting flow around central super-massive black holes in active galactic nuclei (AGN). I calculate the line and continuum emission from accretion disks and tori around rotating black holes using a ray-tracing method. I also study the effect of line-of-sight absorption, with a model in which the absorbing medium is composed of virialised clouds.

The second part of the thesis examines situations where scattering is important. I derive a covariant transfer formulation which uses a basis set of projected symmetric tensors for a series of moments. My formulation is similar, yet simpler than an alternative method which uses projected symmetric *trace-free* tensors derived by Thorne (1981). I then calculate the emission from accretion tori where electron scattering dominates other radiative processes.

# Contents

# List of Figures

# Table of Variables

| Variable | Description |
|---|---|
| $a$ | black hole spin parameter ..... 40 |
| $a^\alpha$ | acceleration four-vector ..... 42 |
| $\mathbf{B}$ | magnetic field ..... 26 |
| $B$ | black body emissivity ..... 35 |
| $\mathcal{B}$ | relativistic black body emissivity ($B/\nu^3$) ..... 115 |
| $B_R$ | radial component of magnetic field ..... 26 |
| $B_\phi$ | axial component of magnetic field ..... 26 |
| $c$ | speed of light ..... 28 |
| $c_\mathrm{s}$ | speed of sound ..... 20 |
| $C$ | integration constant ..... 21 |
| $dN/d\mathcal{V}$ | number density of particles ..... 45 |
| $ds$ | length of a spatial element along a path ..... 45 |
| $d\tau$ | space-time interval ..... 44 |
| $d\mathcal{V}$ | phase-space volume element ..... 44 |
| $d\Omega$ | solid angle element ..... 45 |
| $D(R)$ | dissipation rate ..... 22 |
| $E$ | energy ..... 40 |
| $E_\mathrm{line}$ | rest energy of an emission/aborption line ..... 66 |
| $E_\gamma$ | photon energy ..... 66 |
| $g_{\alpha\beta}$ | metric (signature $+\ -\ -\ -$) ..... 44 |

# Chapter 1

# Introduction

## 1.1 Overview

In this thesis I investigate general relativistic radiative transfer and apply it to model the emission from Active Galactic Nuclei (AGN). AGN provide a laboratory where extreme physics is the norm. There is accumulating evidence that super-massive black holes reside in their centres. The curvature of space-time around these black holes affects the hydrodynamics of the accretion flows. It also modifies the transfer of radiation that the flows emit.

I present a derivation of a covariant formulation for radiative transfer. The formulation includes emission, absorption and scattering. I use the notation of four-vectors. By expressing quantities as relativistic invariants I avoid the complication of having the Lorentz transformation matrix, as in some other relativistic radiative transfer formulations. The Lorentz factor only ever appears here as a normalisation parameter. It results in a much simpler mathematical description. I show that the covariant radiative transfer equation that I derive preserves the structure of the corresponding split-frame transfer equation in the Newtonian regime.

To solve the transfer equations, I use the standard method of ray-tracing in the case where scattering is absent. I propose a new moment method to solve the

equations for the case where scattering is the dominant process.

The point of this thesis is to highlight the radiative transfer side of my work. I do not use magnetohydrodynamical simulations like that in De Villiers and Hawley (2002, 2003) and Koide (2003) to determine the structure of the accretion flow from which the radiation is emitted. Instead, I consider a semi-analytic approach. The AGN models employed in my study are generic, and may perhaps be relatively primitive in comparison with the latest models in the field. However, they are sufficient for the purposes of the study of radiative transfer effects in AGN environments.

The approach that I adopt provides the freedom to refine the transfer formulation with increasing complexity in the radiative processes. I start by looking at only the emission. Then, I add absorption, and consider the geometrical effects in 3D. Finally, I include scattering. At each step, I choose a relevant aspect of AGN emission to investigate the physics in radiative transfer. What results is a more complete and holistic model of the observed spectrum from AGN.

A natural extension of this study is to include thermal Compton scattering, which produces the characteristic power-law like spectrum, and a more realistic emission spectrum from an irradiated slab of plasma, which produces the spectral lines and edges. These are more complicated tasks which I will carry out in my future work. However, in this thesis I describe how the technical problems can be tackled, based on the calculation as those presented in chapter 3 and in chapter 6.

## 1.2 Active Galactic Nuclei

There are many different classes of AGN, each with different observable properties (see Krolik 1999; Kembhavi & Navliker 1999). They may show different ratios of radio, optical and X-ray flux, differing amounts of variability, and the presence or absence of narrow and broad emission lines in their optical spectra. The unified model of AGN attempts to explain these differences in terms of differing viewing inclination angles to the same basic central engine, with perhaps a second parameter

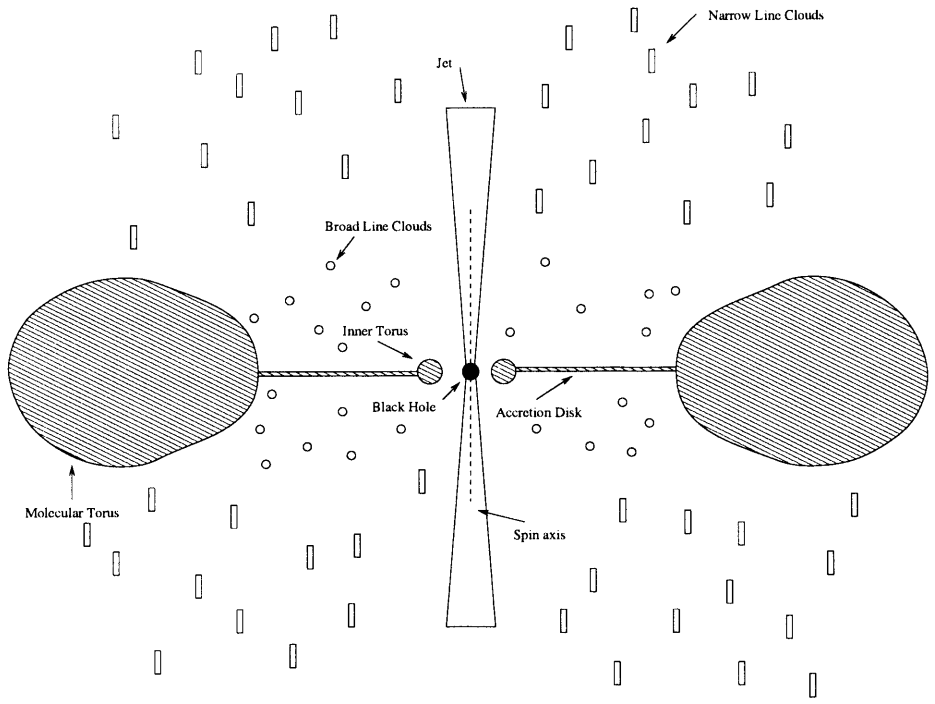


Figure 1.1: A schematic diagram of an active galactic nucleus (Not to scale). The central black hole is surrounded by an accretion disk, which may have an inner torus. The accretion disk is inside the molecular torus. The broad and narrow line clouds are somewhere above the accretion disk plane. Narrow line clouds are further from the black hole than the broad line clouds. There are a pair of jets launched from some region close to the central black hole.

being the intrinsic accretion rate of the source.

In a generic AGN model (see Fig. 1.1.) the central engine is assumed to be a super-massive black hole, surrounded by an accretion disk. There may be some form of jet out-flowing approximately perpendicular to the accretion disk plane along the black hole spin axis. Above the disk, there are the broad emission line clouds at about $10^{18}$cm from the black hole. Close to the disk plane is the molecular/dust torus at around $10^{19}$cm. There are also the narrow emission line clouds at $10^{20-21}$cm. This model contains the essence of the components, yet their linear dimension and the distance to the central black hole are approximate, depending greatly on the AGN's luminosity (see Krolik 1999).

In general, the distances to these structures can be estimated from the observed

widths of spectral lines in various wavebands. If the accretion disk extends to the molecular torus, then material outside the equatorial plane cannot be in orbit as within half an orbital period it would intersect the disk. The assumption is that it must be within some form of outflowing wind. The wind speeds are of the order of the escape velocity. However, even if the outflowing material is not in the form of a wind, the difference between the escape velocity and the velocity due to Keplerian motion is logarithmically small compared to the uncertainties. (See Blustin *et al.* (2005) for the use of the escape velocity and the ionisation parameter to constrain the location of structure in AGN.) These crude distance estimators are enough to determine that the broad line region may be due to material evaporating off the accretion disk or molecular torus, and that the narrow line region is much further out.

Another distance estimator is variability, due to light-speed being the maximum signal speed, and thus setting a distance scale. The reverberation mapping technique with iron lines is based on this principle, and is used to investigate the structure of the inner part of accretion disks around AGN (see Reynold *et al.* 1999).

If an observer is looking directly down the jet, then relativistic Doppler shifts will cause the jet emission to be greatly boosted. In BL Lac objects (Blazars) this is thought to be what happens. Because of the viewing geometry it is sometimes difficult to discern the emission from an accretion disk in such systems. The high energy continuum can be interpreted by synchrotron emission and inverse Compton scattering in the jet. BL Lac objects tend to be highly variable in the radio. Some argue that the variability is not intrinsic, but due to interstellar scintillation. Variability at higher frequencies (optical and X-ray) is also seen, and seems to be intrinsic to these sources. (See Krolik (1999) for more details.)

At inclinations further away from the jet axis, or where there is no jet from the central engine, observers will be able to see emission from the accretion disk. In many systems, the emission manifests as a big blue bump in the optical/UV part of the spectrum. The emission lines from the broad and narrow line regions are

also seen in the optical spectrum. Objects with this viewing geometry are known as Seyfert 1s. It has been suggested that radio-quiet quasars and Seyfert type 1 are the same type of object, with the only difference being that the associated galaxy is not visible in the quasar. At large redshifts, only the brightest sources will be seen, and the relatively low surface brightness of the stellar component of the galaxy may mean that it is difficult to distinguish it from the glare from the core. As observational technology advances, the above distinction was found to be arbitrary, now a distinction based on source luminosity is used: i.e. if $m_{\rm B} < -23$ then the object is classed as a quasar, and a Seyfert 1 otherwise.

At higher inclinations the molecular torus (see Fig. 1.1.) blocks the line of sight to the accretion disk. We can only see scattered light from the central engine. The scattered light is polarised. The high viewing inclination also implies that the broad line region may be obscured. If the narrow line region is visible, but the broad line region is not, then the objects are classed as Seyfert 2s.

Galactic nuclei are complicated objects and do not always fit nicely in the above classes. A problem is that there may be dust lanes and large amounts of star formation. Both of which cause obscuration of the AGN. Observationally, it can be difficult to use optical data to tell the difference between a galaxy with a weak AGN and that with no AGN at all when there is a large amount of star formation. However, from their X-ray spectra, AGN can readily be distinguished from starburst galaxies which have collections of supernova remnants and hot stars visible in the X-ray band. Note that if the intrinsic column depth is above $10^{21}$ H atoms $\rm cm^{-2}$, then photons with energies between 13.6 eV and about 1 keV will be totally absorbed. In dusty obscured AGN, all that is seen is large amounts of infra-red light from glowing dust with the luminosity characteristic to an AGN. These objects are known as 'ultra luminous infra-red galaxies' (see e.g. Krolik 1999).

## 1.3 Geometrically Thin Accretion Disks

A simple prescription to construct an accretion disk model was proposed by Shakura and Sunyaev (1973). It is non-relativistic, and it assumes that the disk is geometrically thin and the viscosity is due to subsonic turbulence. The largest eddies are smaller than the disk thickness, and hence

$$\nu = \alpha c_s H, \tag{1.1}$$

where $\nu$ is the viscosity, $c_s$ is the sound speed, $H$ is the disk thickness, and $\alpha$ is a dimensionless parameter less than one. This so called $\alpha$-disk model compartmentalises the lack of knowledge of how the viscous dissipation in an accretion disk works into the $\alpha$ parameter. This approach is still predictive even though there is a free parameter in the model since many properties of thin disks depend weakly on the exact value of $\alpha$. Conversely, because the value of $\alpha$ doesn't change the disk observables substantially, it is very hard to use disk observations to constrain its value.

The $\alpha$-disk can be modified to include a vertical structure (see e.g. Frank, King and Raine 1985). The disk is thin, i.e. the vertical extension is much smaller than the disk radius. The vertical and radial dependence of variables in the disk are separable. In addition, the disk is axisymmetric and stationary. Most parameters can then be integrated vertically yielding surface densities which depend only on $R$ (and $\alpha$).

For hydrostatic equilibrium in the vertical direction, the continuity equation gives

$$\frac{1}{\rho}\frac{\partial P}{\partial z} = \frac{\partial}{\partial z}\left[\frac{GM}{\sqrt{R^2+z^2}}\right], \tag{1.2}$$

where $\rho$ is the density, $P$ the pressure, and $M$ is the mass of the central accreting object. $R$ is the cylindrical radius, and $z$ is the height out of the equatorial plane. For a thin disk $z \ll R$, it follows that

$$\frac{1}{\rho}\frac{\partial P}{\partial z} \simeq \frac{\partial}{\partial z}\left[\frac{GM}{R\left(1+\frac{1}{2}\frac{z^2}{R^2}\right)}\right],$$

$$\simeq \frac{-GMz}{R^3} . \tag{1.3}$$

Noting that

$$\frac{\partial P}{\partial z} \simeq \frac{P}{H} , \tag{1.4}$$

where $H$ is a pressure scale-height, $z \sim H$, and

$$P = \rho c_s^2, \tag{1.5}$$

where $c_s$ is the local speed of sound. Hence,

$$H \simeq c_s R \sqrt{\frac{R}{GM}} . \tag{1.6}$$

Since the disk is thin, i.e. $H \ll R$,

$$c_s \ll \sqrt{\frac{R}{GM}} . \tag{1.7}$$

We determine the radial flow of matter and angular momentum through the thin disk from the continuity equation:

$$\frac{\partial}{\partial R} (R\Sigma v_R) = 0, \tag{1.8}$$

where $\Sigma = \int \rho \, dz$ is the surface density of the disk. Integrating this equation yields the accretion rate

$$\dot{M} = -2\pi R \Sigma v_R. \tag{1.9}$$

From conservation of angular momentum,

$$\frac{\partial}{\partial R} \left( v_R \Sigma R^3 \Omega \right) = \frac{\partial}{\partial R} \left( \nu \Sigma R^3 \frac{\partial \Omega}{\partial R} \right), \tag{1.10}$$

where $\Omega$ is the angular velocity of the gas at radius $R$. Integrating, and then simplifying gives

$$\Sigma v_R \Omega = \nu \Sigma \frac{\partial \Omega}{\partial R} + \frac{C}{2\pi R^3} , \tag{1.11}$$

where this again yields a constant, $C/2\pi$, which is determined by the inner boundary condition of the disk. At some radius, say $R_\star$, the gas stops transporting angular

momentum outwards and must form a boundary layer with the central object, so $\partial\Omega/\partial R = 0$. The angular velocity at this radius is approximately Keplerian, thus

$$\Sigma v_R \sqrt{\frac{GM}{R_\star}} = \frac{C}{2\pi {R_\star}^3} , \tag{1.12}$$

and

$$\begin{aligned} C &= 2\pi\Sigma v_R \sqrt{{R_\star}^3 GM} \\ &= -\dot{M}\sqrt{R_\star GM} . \end{aligned} \tag{1.13}$$

Substituting this into equation (1.11) and assuming the gas is in Keplerian motion everywhere gives

$$\nu\Sigma = \frac{\dot{M}}{3\pi}\left(1 - \sqrt{\frac{R_\star}{R}}\right), \tag{1.14}$$

and

$$v_R = \frac{-3\nu}{2R\left(1 - \sqrt{\frac{R_\star}{R}}\right)} . \tag{1.15}$$

For $R \gg R_\star$, $v_R$ is proportional to $\nu/R$, which in the $\alpha$-disk formulation is

$$v_R \sim \frac{\alpha c_s H}{R} \ll c_s, \tag{1.16}$$

as $\alpha < 1$. The radial motion in the thin accretion disk model is therefore a slow inwards drift, much smaller than the supersonic Keplerian motion in the rotational direction.

Using the viscosity we obtain the dissipation rate

$$D(R) = \frac{3GM\dot{M}}{8\pi R^3}\left[1 - \sqrt{\frac{R_\star}{R}}\right]. \tag{1.17}$$

We can then derive the mid-plane temperature of an opaque disk, which depends on the optical depth $\tau$:

$$\frac{4\sigma}{3\tau}T^4 \approx D(R). \tag{1.18}$$

(See Frank King and Raine (1985) for more details.)

Finally, all of these equations can be combined to obtain the radial dependence of variables, and thus the structure of a thin accretion disk. For example,

$$\frac{H}{R} = 1.7 \times 10^{-2} \alpha^{-1/10} \dot{M}_{16}^{3/20} m_1^{-3/8} R_{10}^{1/8} f^{3/5} , \tag{1.19}$$

where $\dot{M}_{16} = \dot{M}/(10^{16}\mathrm{g\ s^{-1}})$, $m_1 = M/M_\odot$, $R_{10} = R/(10^{10}\mathrm{cm})$, and

$$f = \left[ 1 - \sqrt{\frac{R_\star}{R}} \right]^{1/4} . \tag{1.20}$$

Note that the disk is indeed thin, $H \ll R$, and that the dependence of the result on the unknown $\alpha$ is weak.

## 1.4 Geometrically Thick Accretion Disks

The thin disk solution breaks down when the accretion rate, $\dot{M}$, becomes too large. This happens when the radiation pressure balances the gravitational force. For spherical accretion, the corresponding luminosity is called the Eddington luminosity, which is given by

$$L_{\mathrm{Edd}} = \frac{4\pi G M m_{\mathrm{p}} c}{\sigma_T} , \tag{1.21}$$

Defining the accretion rate that produces this luminosity as $\dot{M}_{\mathrm{crit}}$, the equation for the disk scale height, $H$, becomes

$$H \simeq \frac{3R_\star}{4\eta} \frac{\dot{M}}{\dot{M}_{\mathrm{crit}}} \left[ 1 - \sqrt{\frac{R_\star}{R}} \right] , \tag{1.22}$$

where $\eta$ is the accretion efficiency. As the accretion rate approaches the Eddington limit, the disk height increases until it is no longer negligible in the inner disk, i.e. at small $R$. Here it shows the thin disk solution easily breaks down at the inner part of the disk. Thus in AGN, we would expect that the inner accretion disk might be geometrically thick, resembling a torus.

Thick disks differ from thin disks because all parameters need to be described in terms of both $R$ and $z$. Vertically-integrated quantities are no longer physically

meaningful. Furthermore, the $\alpha$ model of viscosity breaks down when $H \approx R$, causing the system of equations to be unclosed.

To resolve this, we usually parametrise the angular velocity or angular momentum of the toroidal material instead of using the viscosity (Abramowicz 2004). This is justified as the energy dissipated in a thick torus can flow in any direction before it is radiated from the surface. We note that the flux cannot be neatly separated into radial and vertical components like in the thin $\alpha$-disk model. A proper treatment with explicit consideration of the viscosity is complicated because it can be non-local (see §1.5), but we ignore such complications here.

Assuming that the fluid in the torus has a velocity field that only contains motion in the $\hat{\phi}$ direction, and using the condition of hydrostatic equilibrium, we obtain

$$\begin{aligned} \frac{1}{\rho}\frac{\partial P}{\partial R} &= -\frac{\partial \Phi}{\partial R} + \Omega^2 R, \\ \frac{1}{\rho}\frac{\partial P}{\partial z} &= -\frac{\partial \Phi}{\partial z}\ , \end{aligned} \tag{1.23}$$

where $\Phi$ is the gravitational potential. In vector form this is

$$\frac{1}{\rho}\nabla P = -\nabla\Phi + \Omega^2 R = g_{\text{eff}}, \tag{1.24}$$

where $g_{\text{eff}}$ is the effective gravitational acceleration. For a polytropic equation of state, iso-density and pressure surfaces will be perpendicular to the effective acceleration field. (We will use this property to derive the shape of relativistic tori in chapter 4.) Note that there is a condition required in order for a polytropic equation of state to hold in these accretion tori. Taking the curl of equation (1.24) gives

$$\nabla\left(\frac{1}{\rho}\right) \times \nabla P = 2\mathbf{v}\frac{\partial \Omega}{\partial z}\ , \tag{1.25}$$

which shows that the density and pressure surfaces only coincide if $\Omega$ is purely a function of $R$. The form of the velocity law can therefore be written as a function of $r\cos\theta = R$.

In some cases, the functional form for $\Omega$ is sufficiently simple and we can integrate equation (1.24) to obtain analytic descriptions for the radial and vertical dependence

of the density and pressure. Since $\Omega$ is a free parameter, this method generates any shape of torus, from extremely fat through to wedge-like shapes, through to tori that look like normal doughnuts. This lack of constraint is problematic. To overcome this, I therefore use a shape that approximates the geometrical aspects of the tori obtained by numerical MHD simulations, rather than choosing an arbitrary model with particular mathematical simplicity.

Note that thick accretion tori are unstable to non-axisymmetric global modes (see Kojima 1986). Adding a small radial component due to accretion may invalidate this analysis (Frank King and Raine 1985). In any case, traditional thin disks are also unstable due to magnetic effects, as will be discussed in the next section. This means that accretion onto AGN is likely to be an unsteady process regardless of whether or not the disk is in the thin or thick regime, as shown in simulations by De Villiers and Hawley (2003).

## 1.5 The Magneto-Rotational Instability

It has been known for a long time that the viscosity responsible for the angular momentum transport in accretion disks cannot be normal gas kinematic viscosity. If it were, then the accretion timescales would be on the order of a Hubble time and the luminosities of AGN would be much less than observed (see Frank, King and Raine 1985).

Shakura and Sunyaev (1973) proposed that some form of turbulence leads to an effective viscosity large enough for accretion to work. However, it can be shown that purely hydrodynamic turbulence is unlikely to form in accretion disks. For turbulence to form, some form of instability is required. The Rayleigh stability criterion,

$$\frac{\partial(R^2\Omega)}{dR} > 0, \tag{1.26}$$

holds everywhere in a Keplerian disk, and the fluid flow is expected to be laminar. This implies that either there is some form of nonlinear hydrodynamic instability, or

angular momentum transport is due to some other mechanism. For example, a disk wind might be able to extract enough angular momentum for accretion to follow (Maruta 2003).

Balbus and Hawley (1991) proposed an alternative mechanism, which invokes magnetic fields to generate the turbulence, and thus angular momentum transport required for accretion disks to function as observed. The key point is that the physical character of magnetohydrodynamics (MHD) is subtly different from that of hydrodynamics. The tension forces of a magnetic field have no correspondence in the hydrodynamic regime. A weak magnetic field may act like a spring. If there is a radial field in a rotating disk, then two gas volume elements will have a force acting on them. The inner element will experience a force tending to slow it down. This causes the element to move inward, where paradoxically, the change of orbit causes it to speed up. The reverse happens to the outer gas element. As a consequence, the magnetic field 'spring' is stretched, transferring angular momentum in the process. The radial field is eventually wound into a toroidal field as the disk rotates differentially.

The Parker instability causes regions with higher than average magnetic flux to be buoyant. Thus the toroidal field will rise out of the disk, forming a poloidal component. The radial instability then causes small radial kinks in the poloidal field to grow exponentially, completing the dynamo. This is called the magneto-rotational instability (MRI).

The derivation of the growth rate of the MRI can be performed by perturbation analysis of the MHD equations:

$$\begin{aligned} -i\omega\delta v_R - 2\Omega\delta v_\phi - \frac{ikB}{4\pi\rho}\delta B_R &= 0, \\ -i\omega\delta v_\phi + \frac{1}{2}\Omega\delta v_R - \frac{ikB}{4\pi\rho}\delta B_\phi &= 0, \\ -i\omega\delta B_R - ikB\delta v_R &= 0, \\ -i\omega\delta B_\phi + \frac{3}{2}\Omega\delta B_R - ikB\delta v_\phi &= 0, \end{aligned} \tag{1.27}$$

where the perturbations in density and pressure are zero, $\omega$ refers to the frequency

of the perturbation, and $k$ to its wave number. The perturbations on the magnetic field and velocity are given by $\delta B_R, \delta B_\phi, \delta v_R$ and $\delta v_\phi$ respectively, and $B$ is the magnitude of the unperturbed magnetic field.

These equations result in the dispersion relation

$$\frac{\omega^2}{\Omega^2} = q^2 + \frac{1}{2}\left(1 \pm \sqrt{1 + 16q^2}\right), \tag{1.28}$$

where, as in Krolik (1999), the reduced wavenumber $q = kB/\Omega\sqrt{4\pi\rho}$. The positive sign of the square root corresponds to stable sound-wave like solutions, and the negative sign to growing modes. The maximum growth factor occurs when $q = \sqrt{15/16}$, $\mathrm{Im}(\omega) = (3/4)\Omega$, corresponding to an instability which happens on the order of the orbital timescale. This instability also holds in the relativistic regime around Kerr black holes (Gammie 2004).

There are two ways to halt this instability. The first is to have an extremely strong magnetic field, where the weak spring approximation breaks down, and the two gas volume elements described above are forced to move in lock-step. This happens when the MRI saturates and enters the non-linear regime. The second is for the magnetic field dissipation timescale to be comparable to the orbital timescale. This is not likely for AGN, but may be relevant to poorly ionised circumstellar disks like that which formed our solar system (Salmeron & Wardle 2004).

If there is any magnetic field in an AGN accretion disk, it is quickly amplified until nonlinear effects suppress the growing modes of the MRI. The result is a magnetically turbulent disk. This turbulence requires a different description than the standard $\alpha$-disk model. The effects of magnetic fields are non-local, as tension along field lines can transport angular momentum from one place to another. There is no well-defined description of a local viscosity for the disk, and only global properties give rise to the angular momentum transport.

## 1.6 Radiative Transfer

### 1.6.1 A Classical Description

Radiative transfer is the study of how light propagates through a medium. The ability of light to transmit information about the physical properties of matter to afar means that it is a tool in extracting information from observations. The basic processes in radiative transfer are emission, absorption and scattering. These processes also apply to the transport of gravitational waves and neutrinos.

In this thesis I investigate the situations where the wavelength of light is small compared to other characteristic length scales of the objects and the environment. For example, the wavelength of X-rays are much smaller than the gravitational radius, $R_{\rm G}$, of a super-massive black hole in AGN, which is of order of an A.U. The use of the geometrical optics approximation is therefore sufficient and we may ignore effects of diffraction. In addition, I assume that the refractive index for the frequencies of interest is unity, and the path of the light is bent only by gravitational effects. These assumptions simplify the treatment further, replacing a dispersion tensor with the constant speed of light, $c$, which I then normalise to be 1 through choice of units (Marklund 2005).

In flat space-time the equation of radiative transfer equation for the case where the medium is at rest can be expressed as

$$\frac{\partial I_\nu}{\partial \lambda} = -\chi I_\nu + \eta + \iint \sigma(\nu,\nu') I'_\nu(\Omega') d\Omega' d\nu', \tag{1.29}$$

where $I_\nu$ is the intensity, $\lambda$ is an affine parameter which describes the space-time interval along the ray-path, $\chi$ is the absorption, $\eta$ is the emissivity, and $\sigma$ is the scattering kernel. All of these variables (except $\lambda$) are functions of photon frequency, $\nu$. This is an integro-differential equation. Usually it is difficult to obtain analytic solutions, except for cases where there is a large amount of symmetry. A difficulty is the spatially non-local properties of the scattering term. Light from outside the line-of-sight may be scattered into it. In order to determine the intensity along a

particular ray, the entire radiation field throughout all of space must be calculated. Another difficulty is that scattering can lead to energy/frequency redistribution. (See Mihalas 1978, Mihalas & Mihalas 1984; Peraiah 2002) Further difficulties occur because boundary conditions in both normal space and frequency space are required.

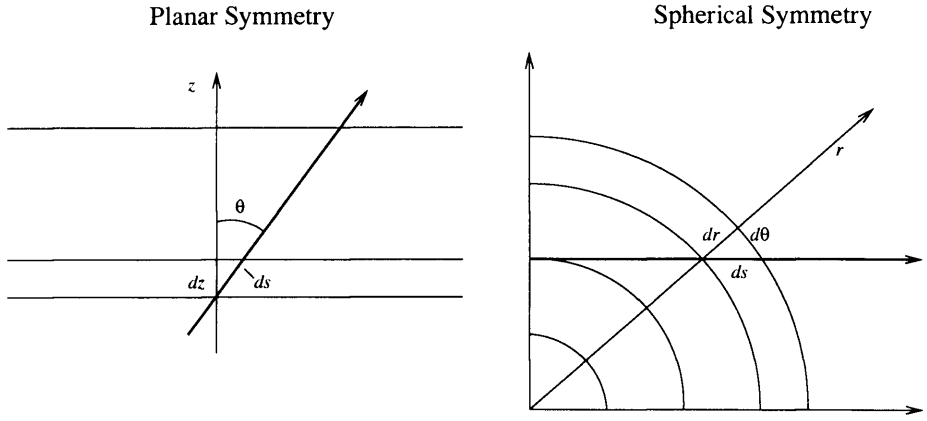


Figure 1.2: The propagation of light rays in planar and spherically symmetric radiative transfer problems.

If there is enough symmetry, the above equation can be reduced to a one-dimensional form. This happens in the plane-parallel case, where the radiation field only depends on the $z$ coordinate. Another example is spherically symmetric problems, where radiation field will only depend on the radial direction $r$. Defining $\mu = \cos\theta$ where $\theta$ is the angle between the ray and the remaining dimension of dependence yields

$$\frac{\partial I_\nu}{\partial t} + \mu \frac{\partial I_\nu}{\partial z} = -\chi I_\nu + \eta, \tag{1.30}$$

for the plane-parallel case, and

$$\frac{\partial I_\nu}{\partial t} + \mu \frac{\partial I_\nu}{\partial r} + \frac{(1-\mu^2)}{r} \frac{\partial I_\nu}{\partial \mu} = -\chi I_\nu + \eta, \tag{1.31}$$

for the spherical case. See Fig. 1.2. for the geometry of the formulation.

If there is no scattering, then the above equation can be solved in terms of

quadratures,

$$I_\nu(\lambda) = I_\nu(\lambda_0)\exp\left(-\int_{\lambda_0}^{\lambda}\chi(\lambda',\nu)d\lambda'\right) - \int_{\lambda_0}^{\lambda}\exp\left(-\int_{\lambda'}^{\lambda}\chi(\lambda'',\nu)d\lambda''\right)\eta(\lambda',\nu)d\lambda' \ . \tag{1.32}$$

Thus the emission from each element along the path are absorbed proportionally to the opacity along the line of sight. The initial intensity $I_n u(\lambda_0)$ is a special case of this, where the full path length through the medium is the relevant factor.

### 1.6.2 Radiative Processes

Radiation can arise from three different processes; free-free, free-bound, and bound-bound transitions, referring to the states of electrons before and after an atomic transition occurs. A spectral line is usually produced in bound-bound processes, when an atom (or ion) is placed into an excited state, which then decays by emitting a photon. Since the states are quantised, a specific frequency is emitted. The emitted line has a natural width due to the Heisenberg uncertainty principle ($\Delta t \Delta E \approx \hbar$) linking the half-life of the state ($\Delta t$) to the energy uncertainty of the emitted photons ($\Delta E$). The line is also broadened by microscopic Doppler shifts due to the thermal motions within the gas. Pressure also affects the intrinsic line width by introducing collisions which alter ($\Delta t$). Finally, macroscopic motions may introduce Doppler shifts which can increase the line width when the emission is integrated over a large region with an inhomogeneous velocity field.

In this thesis, much attention is paid to the Iron K$\alpha$ lines in the X-ray spectrum of AGN. The line is produced when a high energy photon ejects an inner-shell electron from an iron atom. The result is that an L shell electron makes a transition into the K shell. This transition may produce a photon, or may eject another electron. The resulting photon depends on the ionisation state of the iron atom (ion). For weakly ionised iron, the energy levels of the inner shells are only slightly affected by the ionisation state. Once large numbers of electrons have been removed from the iron atom, this process changes character due to the lack of electrons in the L shell,

and the process of electronic recombination occurs instead. For helium-like iron the energy of the transition from the L shell into the K shell rises to 6.7 keV, and for hydrogen-like iron the transition produces a line at 6.9 keV.

The reason for investigating the iron K$\alpha$ line is that it may be a tracer of the strongly relativistic physics occurring in the central engine of an AGN. (See Nandra *et al.* (1997) for an iron line seen by ASCA, and see Reynolds *et al.* (1999) for the use of iron line reverberation to study the accretion disk structure.) Reflection of X-rays from effectively neutral gas with cosmic abundances in an accretion disk produces a characteristic spectrum with relativistic lines and edges (see e.g. Fabian *et al.* 2000). Since the fluorescent yield is proportional to $Z^3$, and iron is the most abundant element with high atomic number, its line dominates. Note that high abundances of carbon, nitrogen and oxygen may also produce relativistic lines and edges into the reflection spectrum (e.g. Branduardi-Raymont *et al.* 2001). However, the latter is controversial (see Lee *et al.* 2001; Sako *et al.* 2003).

The inverse process of line emission is resonant line absorption, when a photon is absorbed, exciting an atom into a higher state. The atom may eventually de-excite and release a photon of the same energy as the initial absorbed photon, yet at a different direction. This process is known as resonant line scattering. Alternatively, the atom may be de-excited in a different means, perhaps ejecting electrons or photons as a more indirect route is taken back to the ground state. In this process, the atom effectively absorbs photons with the given line energy, re-radiating it somewhere else in the spectrum, either as a continuum (when the ejected electrons eventually scatter off of other atoms) or as other lines.

Continuum emission is usually related to free-free processes. The simplest model of a continuum is blackbody radiation whose spectrum is given by the Planck function. This is the spectrum at high optical depth in a thermal medium, where thermal equilibrium is maintained between the medium and the radiation. If the medium is non-thermal (like a power-law distribution of electrons), a blackbody spectrum will not be obtained. Likewise, emission from an optically thin region will also not have

a blackbody profile.

However, a blackbody spectrum is not always observed as emission from a real atmosphere. The fact that the radiation field is highly anisotropic at its surface drives the matter away from local thermodynamic equilibrium. This makes the assumption thermal equilibrium between the medium and the radiation field break down. If the opacity is dominated by scattering instead of absorption, the effects of the surface can be felt at very large optical depths into the medium. Only at a depth exceeding the photon destruction length will local thermodynamic equilibrium assert itself (Mihalas & Mihalas 1984). Thus the emission from a surface element of an accretion disk is not strictly described by a Plank function.

Another common continuum generating process in hot astrophysical plasma is free-free bremsstrahlung emission. For the densities and temperatures relevant to AGN central engines, free-free emission is generally optically thin, and free-free absorption in the X-ray band is negligible. Other important continuum processes in AGN include Compton scattering and synchrotron radiation. (For detailed discussion of spectral formation due to Compton scattering, see e.g. Sunyaev & Titarchuk (1980) or Pozdniakov, Sobol & Sunyaev (1983).)

## 1.7 Scattering in Radiative Transfer

### 1.7.1 The Moment Method

In AGN, the opacity of the emitting medium is due to electron scattering. This process can not be approximated properly by absorption in a ray-tracing calculation. Once scattering is considered, the radiative transfer equation is non-local and in general it can not be solved analytically. The intensity no longer separates into individual frequency and directional components.

A number of numerical methods have been proposed to solve the transfer equations in the presence of scattering (see e.g. Mihalas & Mihalas 1984, Peraiah 2002).

A naive method is to generalise the ray tracing technique described above with a Monte-Carlo algorithm. Follow the rays from the observer backwards in time, and at every time-step scatter them with a probability depending on the cross section. Unfortunately, in order to accumulate a good sampling of what is seen, many rays are required. For moderate optical depths, the rays are scattered only once or twice along their paths, and this method works fairly well. However, as the optical depth approaches unity this method becomes impractical. The number of scatterings becomes quadratic in optical depth as the photons enter the diffusion regime, and the supra-exponential explosion in ray numbers quickly grinds this method to a halt.

Another method is to use a spectral technique, and assume that the radiation field can be expanded in a series of functions of position, energy and direction. By truncating the series appropriately, a good approximation of the physics may be retained. A solution may be obtained by solving for the coefficients of these functions. The moments of the cosine of the ray angle with respect to the surface normal is a choice of function set that is often used to model plane-parallel transport.

We may define the moments:

$$\begin{aligned} J &\equiv \int I(\mu) d\Omega, \\ H &\equiv \int \mu I(\mu) d\Omega, \\ K &\equiv \int \mu^2 I(\mu) d\Omega, \qquad (1.33) \\ &\ldots \qquad (1.34) \end{aligned}$$

This simple method assumes axisymmetry in the $\hat{\phi}$ direction. For a more general treatment, the dependence on $\phi$ must be included, typically by changing the basis set to be the spherical harmonics or something similar.

Once the moment expansion is truncated there is one equation fewer than the number of variables, implying that a closure condition is required. For instance, if the flux deviates as little as possible from isotropy, in the 1D planar geometry we

may consider the approximation

$$K = 1/3J. \tag{1.35}$$

This approximation is known as the Eddington approximation, with the factor 1/3 as the 'Eddington factor'. (See Rybicki and Lightman (1979) for more details.) If a spherical atmosphere is used instead of a plane-parallel one, the expression for the Eddington factor is more complicated (see Mihalas & Mihalas 1984).

When expanding in spherical harmonics, the closure condition is simpler: just set all harmonics with higher $l$ to be zero. Other closure conditions may be used if certain physical conditions are known. For example, varying the Eddington factor with position, a method known as 'variable Eddington Factors', may be used to fit the case of a medium with a boundary more accurately than moving the extra degree of freedom into an extra moment, and using a standard isotropic closure condition (Mihalas & Mihalas 1984).

### 1.7.2 The Eddington Approximation

The Eddington approximation can be used to obtain analytic approximations for the radiation field through a static slab of matter. Since the matter is static, there are no Doppler shifts. The stationary one-dimensionality of the problem means that the only spacial dependence is in $z$, i.e.

$$\frac{\partial}{\partial x} = \frac{\partial}{\partial y} = \frac{\partial}{\partial t} = 0. \tag{1.36}$$

The Eddington approximation assumes that the intensity is a linear function of $\mu$. i.e.

$$I(\mu, z) = a(z) + \mu\, b(z). \tag{1.37}$$

The radiative moments can be extracted

$$\begin{aligned} J &= \frac{1}{2}\int_{-1}^{1} I d\mu = a, \\ H &= \frac{1}{2}\int_{-1}^{1} \mu I d\mu = \frac{b}{3}, \end{aligned}$$

$$K = \frac{1}{2}\int_{-1}^{1} \mu^2 I d\mu = \frac{a}{3}, \tag{1.38}$$

and the result $K = 1/3J$ appears as is described above.

These moments can then be used in the radiative transfer equation;

$$\mu\frac{\partial I}{\partial z} = -\kappa(I - B) + \sigma(J - I), \tag{1.39}$$

which describes a medium where absorption is specified by $\kappa$, with a corresponding thermal emissivity $\kappa B$, ($B$ being the black body emissivity), combined with isotropic scattering parametrised by $\sigma$. Integrating over all angles yields

$$\frac{\partial H}{\partial z} = \kappa(B - J), \tag{1.40}$$

and multiplying by $\mu$ before the integration gives

$$\frac{\partial K}{\partial z} = -(\kappa + \sigma)H. \tag{1.41}$$

Substituting in the closure condition, we obtain

$$\frac{\partial J}{\partial z} = -3(\kappa + \sigma)H. \tag{1.42}$$

Differentiated with respect to $z$ and combined with equation (1.40) yields

$$\frac{\partial^2 J}{\partial z^2} = 3\kappa(\kappa + \sigma)(J - B), \tag{1.43}$$

which is known as the radiative diffusion equation. The equation can be solved with suitable boundary conditions to obtain the distribution of radiation throughout the slab. By including more moments this method can be made more accurate, as second order and higher order moment functions are used to approximate $I$. In chapter 6 I will present a general relativistic version of this method, which is used to calculate emission from accretion tori with opacity dominated by electron scattering.

## 1.8 Relativistic Emission Lines from Accretion Disks

The emission lines in the X-ray spectrum are a key diagnostic of physical processes in the inner AGN environment. These lines are broadened by the Doppler shifts due

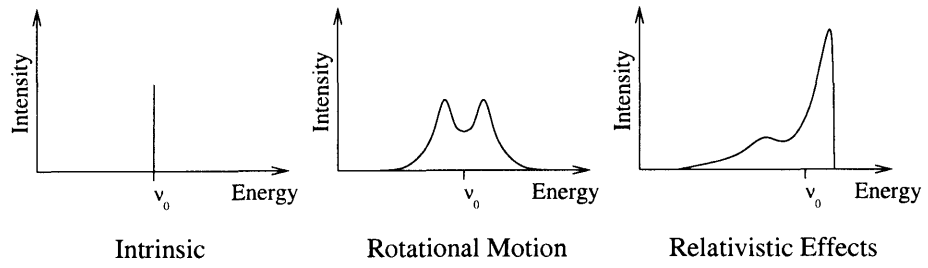


Figure 1.3: Illustration to show how a line profile from an accretion disk is formed. The intrinsic delta function shape of a line is distorted into a double-peaked profile because of opposite line-of-sight motion on two sides of the accretion disk. Relativistic effects cause the line to become asymmetric.

to the motion of the emitting gas. They are distorted by the curvature of space-time induced by the presence of a super-massive black hole. The strength and ratios of the lines provide us information about the abundances of ionic species and the properties of the radiation field.

Here, unless otherwise stated, the term 'X-ray line' is generally referring to the neutral iron K$\alpha$ line. It is the most prominent line in the X-ray spectrum. There has been much effort spent in modelling it, not only for understanding the astrophysics of AGN, but also for probing the structure of space-time in the vicinity of the black hole event horizon.

Emission lines from a non-relativistic Keplerian accretion disks usually have a double-peaked profile because of the rotational motion of the material (Smak 1969). For relativistic accretion flow, the disk lines will be asymmetric, with the blue peak stronger than red, because of the Doppler boosting effect. For lines originating from disk regions near the black-hole event horizon, gravitational redshift and time dilation also shift the lines to lower energies (see the review by Fabian *et al.* 2000). Fig. 1.3. shows how the distortions combine to form the observed line profile. Since space-time is curved near a black hole, an accretion disk may be lensed to show multiple images, hence modifying the line profiles. The emission is also subject to absorption and scattering by material along the line-of-sight. Thus the line profile could deviate significantly from the asymmetric double horn profile as predicted by

the idealised model.

There have been many studies to model the emission lines from accretion disks around black holes. In general, the calculations put emphasis on relativistic effects such as space-time curvature, and they usually employ one of the following three techniques.

The first makes use of a transfer function that maps the image of the accretion disk onto a sky plane (Cunningham 1975, 1976). The accretion disk is assumed to be Keplerian, geometrically thin and optically thick, and it is in the equatorial plane. The space-time metric is first specified, and the energy shift of photons from each point on the disk surface is then calculated. A parametric emissivity law is assumed, usually a simple power-law decreasing outward radially, and the specific intensities in the sky plane are determined from the energy shift from the specific intensities at the disk surface using the Lorentz-invariant property (see §2.3). The transfer-function formulation (Cunningham 1975, 1976) has been applied to calculate line emission from thin accretion rings (e.g. Gerbal & Pelat 1981) and accretion disks around Schwarzschild (e.g. Laor 1991) and rotating (Kerr) black holes (e.g. Bromley, Chen & Miller 1997).

The second considers the impact parameter of photon orbits around Schwarzschild black holes (Fabian *et al.* 1989; Stella 1990; Kojima 1991). The transfer function is described in terms of elliptical functions, and is derived semi-analytically. The Jacobian of the transformation from the disk to sky plane is determined numerically via infinitesimal variations of the impact parameter (Bao 1992). The method is later generalised to the case of Kerr black holes by using additional constants of motion (Viergutz 1993; Bao, Hadrava & Østgaard 1994; Fanton *et al.* 1997; Cadez, Fanton & Calvani 1998).

The third directly integrates the geodesics to obtain the energy shifts and trajectories of the photons (Dabrowski *et al.* 1997; Pariev & Bromley 1998; Reynolds *et al.* 1999). This is the method used in my study because it provides the flexibility to incorporate additional radiative transfer processes such as absorption without

alteration of the numerical algorithm.

Various aspects of the emission, e.g. reverberation and reflection (Reynolds *et al.* 1999), and effects of higher order images (Viergutz 1993; Boa, Hadrava & Østgaard 1994), have been investigated using one of the three methods mentioned above. These studies have shown how the intrinsic profiles of emission lines are shaped by the dynamics of the accretion flow and by the space-time near the black hole. They have provided a framework to interpret the observations qualitatively, in particular, the Fe lines in X-ray spectra. Absorption by line-of-sight material was addressed only in the recent studies by Ruszkowski & Fabian (2000) and Fuerst & Wu (2004), where the results are based on this work. Absorption and scattering are important in the line formation process. They must be properly considered in spectral models in order to obtain results that are useful for interpreting observations.

# Chapter 2

# General Relativistic Kinematics

One needs to determine the motion of the emitters and absorbers in order to carry out the radiative transfer calculations. In the presence of strong gravity, space-time is not flat, and the motion of particles is affected by the space-time curvature. Even massless particles, like photons, would have curved trajectories. In the vicinity of a Kerr black hole, space-time is dragged by the black hole's rotation. For example, inertial frame-dragging effects the angular velocity of particles in Keplerian orbits around spinning black holes (see equation (3.2).)

In this chapter, I present the derivation of the equations of motion for particles in curved space time. I consider two cases. The first is where the particles move around Kerr black holes under the influence of gravity with no external forces acting on them. The second case considers particle motion under an external force in the $\hat{\theta}$ direction acting away from the equatorial plane around a Kerr Black hole. These 'powered' orbits are a useful approximation to describe the motion of the absorbers along our line of sight to the accretion disk where the emission is generated.

## 2.1 Free particles

To determine the photon trajectories one must specify the metric of the space-time. (Here and hereafter, I adopt the usual convention $c = G = 1$ for the speed of light

and gravitational constant throughout this thesis.) I consider the Kerr metric in terms of the Boyer-Lindquist coordinates:

$$\begin{aligned} d\tau^2 &= \left(1-\frac{2Mr}{\Sigma}\right)dt^2 + \frac{4aMr\sin^2\theta}{\Sigma}dtd\phi - \frac{\Sigma}{\Delta}dr^2 \\ &\quad -\Sigma d\theta^2 - \left(r^2+a^2+\frac{2a^2Mr\sin^2\theta}{\Sigma}\right)\sin^2\theta d\phi^2 \ , \end{aligned} \tag{2.1}$$

where $M$ is the black hole mass, with the three vector $(r,\theta,\phi)$ corresponding to spherical polar coordinates, and $\Sigma \equiv r^2 + a^2\cos^2\theta$ and $\Delta \equiv r^2 - 2Mr + a^2$. The dimensionless parameter $a/M$ specifies the spin of the black hole, with $a/M = 0$ corresponding to a Schwarzschild (non-rotating) black hole and $a/M = 1$ to a maximally rotating Kerr black hole.

The motion of a free particle is described by the Lagrangian:

$$\begin{aligned} \mathcal{L} &= \frac{1}{2}\Big[-\left(1-\frac{2Mr}{\Sigma}\right)\dot{t}^2 - \frac{4aMr\sin^2\theta}{\Sigma}\dot{t}\dot{\phi} + \frac{\Sigma}{\Delta}\dot{r}^2 \\ &\quad +\Sigma\dot{\theta}^2 + \left(r^2+a^2+\frac{2a^2Mr\sin^2\theta}{\Sigma}\right)\sin^2\theta\dot{\phi}^2\Big] \end{aligned} \tag{2.2}$$

(here $\dot{x}^\alpha = dx^\alpha/d\lambda$), which does not depend explicitly on the $t$ and $\phi$ coordinates. The four momentum components are therefore

$$p_{\rm t} = \partial\mathcal{L}/\partial\dot{t} = -E \ , \tag{2.3}$$

$$p_{\rm r} = \partial\mathcal{L}/\partial\dot{r} = \frac{\Sigma}{\Delta}\dot{r} \ , \tag{2.4}$$

$$p_\theta = \partial\mathcal{L}/\partial\dot{\theta} = \Sigma\dot{\theta} \ , \tag{2.5}$$

$$p_\phi = \partial\mathcal{L}/\partial\dot{\phi} = L \ , \tag{2.6}$$

with $E$ being the energy of the particle at infinity and $L$ the angular momentum in the $\phi$ direction. The corresponding equations of motion are

$$\dot{t} = E + \frac{2r(r^2+a^2)E - 2aL}{\Sigma\Delta} \ , \tag{2.7}$$

$$\dot{r}^2 = \frac{\Delta}{\Sigma}(\mathcal{H} + E\dot{t} - L\dot{\phi} - \Sigma\dot{\theta}^2) \ , \tag{2.8}$$

$$\dot{\theta}^2 = \frac{1}{\Sigma^2}(Q + (E^2+\mathcal{H})a^2\cos^2\theta - L^2\cot^2\theta) \ , \tag{2.9}$$

$$\dot{\phi} = \frac{2arE + (\Sigma - 2r)L/\sin^2\theta}{\Sigma\Delta} \ , \tag{2.10}$$

where $Q$ is Carter's constant (Carter 1968), and $\mathcal{H}$ is the Hamiltonian, which equals 0 for photons and massless particles and equals $-1$ for particles with a non-zero mass. (See Reynolds *et al.* (1999) for more details.) Without losing generality, I have set the black-hole rest mass equal to unity ($M = 1$) in the equations above. This is equivalent to normalising the length to the gravitational radius of the black hole (i.e. set $R_{\rm G} \equiv GM/c^2 = 1$). Unless otherwise stated I will adopt this normalisation hereafter.

There are square terms of $\dot{r}$ and $\dot{\theta}$ in two equations of motion. They could cause problems when determining the turning points at which $\dot{r}$ and $\dot{\theta}$ change sign in the numerical calculations. I therefore consider the second derivatives of $r$ and $\theta$ instead. From the Euler-Lagrange equation, the second derivatives are

$$\begin{aligned}
\ddot{r} &= \frac{\Delta}{\Sigma}\Bigg\{\frac{\Sigma-2r^2}{\Sigma^2}\dot{t}^2+\frac{(r-1)\Sigma-r\Delta}{\Delta^2}\dot{r}^2+r\dot{\theta}^2 \\
&\quad +\sin^2\theta\left(r+\frac{\Sigma-2r^2}{\Sigma^2}a^2\sin^2\theta\right)\dot{\phi}^2 \\
&\quad -2a\sin^2\theta\frac{\Sigma-2r^2}{\Sigma^2}\dot{t}\dot{\phi}+\frac{2a^2\sin\theta\cos\theta}{\Delta}\dot{r}\dot{\theta}\Bigg\}\,, \qquad (2.11)\\
\ddot{\theta} &= \frac{1}{\Sigma}\Bigg\{\sin\theta\cos\theta\Bigg[\frac{2a^2r}{\Sigma}\dot{t}^2-\frac{4ar(r^2+a^2)}{\Sigma}\dot{t}\dot{\phi}-\frac{a^2}{\Delta}\dot{r}^2 \\
&\quad +a^2\dot{\theta}^2+\frac{\Delta+2r(r^2+a^2)^2}{\Sigma^2}\dot{\phi}^2\Bigg]-2r\dot{r}\dot{\theta}\Bigg\}\,. \qquad (2.12)
\end{aligned}$$

In terms of the momenta and the Hamiltonian, the equations above can be re-expressed as

$$\begin{aligned}
\dot{p}_{\rm r} &= \frac{1}{\Sigma\Delta}\Big[(r-1)\left((r^2+a^2)\mathcal{H}-\kappa\right)+r\Delta\mathcal{H} \\
&\quad +2r(r^2+a^2)E^2-2aEL\Big]-\frac{2{p_r}^2(r-1)}{\Sigma}\,, \qquad (2.13)\\
\dot{p}_\theta &= \frac{\sin\theta\cos\theta}{\Sigma}\left[\frac{L^2}{\sin^4\theta}-a^2(E^2+\mathcal{H})\right]\,, \qquad (2.14)
\end{aligned}$$

where $\kappa = Q + L^2 + a^2(E^2 + \mathcal{H})$. Equations (2.4), (2.5), (2.7), (2.10), (2.13) and (2.14) are the equations of motion of free particles.

## 2.2 Particle motion in the presence of external forces

In a general situation, (non-gravitational) external forces may be present. External forces require explicit specification in order to derive the equations of motion. However, in the setting of accretion disks around black holes, we can consider an implicit treatment of the external force. I will discuss this in more detail in the following subsections.

Consider a simple model in which

$$\dot{t} > \dot{\phi} \gg \dot{r} \gg \dot{\theta} \ . \tag{2.15}$$

As $\dot{r}$ and $\dot{\theta}$ are small in comparison with other quantities, they can be neglected as a first approximation.

The equation of motion reads

$$\frac{d^2x^\nu}{d\lambda^2} + \Gamma^\nu_{\alpha\beta} u^\alpha u^\beta = a^\nu \ , \tag{2.16}$$

where $a^\nu$ is the four-acceleration due to an external force per unit mass. For axisymmetry (which is a sensible assumption for accretion onto rotating black holes), $d/d\phi = 0$. If stationarity is assumed, then $a^\phi = 0$. The identity $u^\alpha a_\alpha = 0$ together with $\dot{r} = 0$ and $\dot{\theta} = 0$ imply that $a^t = 0$. One may also set $a^r = 0$ for simplicity. As there is an extra equation from the identity $u^\alpha u_\alpha = -1$, $a^\theta$ can be determined self-consistently under the approximation $\dot{\theta} = 0$. This scenario thus corresponds to flows supported by rotation in the $\hat{r}$ direction and by pressure in the $\hat{\theta}$ direction.

Inserting the affine connection coefficients for the Kerr metric into the equation of motion yields quantities identical to zero on the left hand side of the equations for the $\hat{t}$ and $\hat{\phi}$ directions. This leaves only the non-trivial momentum equation in the radial direction:

$$\begin{aligned} 0 \ = \ & -\left(\frac{\Sigma - 2r^2}{\Sigma^2}\right) \dot{t}^2 + 2\left(\frac{\Sigma - 2r^2}{\Sigma^2}\right) a \sin^2\theta \ \dot{t}\dot{\phi} \\ & - \left[r + a^2 \sin^2\theta \left(\frac{\Sigma - 2r^2}{\Sigma^2}\right)\right] \sin^2\theta \ \dot{\phi}^2 \ , \end{aligned} \tag{2.17}$$

which further simplifies to

$$\frac{r\Sigma^2 \sin^2\theta}{2r^2 - \Sigma}\dot{\phi}^2 = \left(\dot{t} - a\sin^2\theta\dot{\phi}\right)^2 . \tag{2.18}$$

We choose the positive solution,

$$\dot{t} = \left(\frac{\sqrt{r}\Sigma\sin\theta}{\sqrt{2r^2 - \Sigma}} + a\sin^2\theta\right)\dot{\phi} , \tag{2.19}$$

which corresponds to prograde rotation. This solution allows the flow to match the rotation of a prograde accretion disk.

From the metric we obtain

$$\begin{aligned} 1 &= \left(1 - \frac{2r}{\Sigma}\right)\dot{t}^2 + \frac{4ar\sin^2\theta}{\Sigma}\dot{t}\dot{\phi} \\ &\quad - \left(r^2 + a^2 + \frac{2a^2 r\sin^2\theta}{\Sigma}\right)\sin^2\theta\,\dot{\phi}^2 . \end{aligned} \tag{2.20}$$

Combining equations (2.19) and (2.20) yields

$$\Sigma\sin^2\theta\left(\frac{r(\Sigma - 2r)}{2r^2 - \Sigma} + \frac{2\sqrt{r}a\sin\theta}{\sqrt{2r^2 - \Sigma}} - 1\right)\dot{\phi}^2 = 1 . \tag{2.21}$$

The components of the four-velocity are therefore

$$\begin{aligned} \dot{t} &= \frac{1}{\zeta}\left(\Sigma\sqrt{r} + a\sin\theta\sqrt{2r^2 - \Sigma}\right) , \\ \dot{r} &= 0 , \\ \dot{\theta} &= 0 , \\ \dot{\phi} &= \frac{\sqrt{2r^2 - \Sigma}}{\zeta\sin\theta} , \end{aligned} \tag{2.22}$$

where

$$\zeta = \sqrt{\Sigma\left(\Sigma(r+1) - 4r^2 + 2a\sin\theta\sqrt{r(2r^2 - \Sigma)}\right)} . \tag{2.23}$$

The marginally stable orbit for particles is determined by the surface where

$$\frac{\partial E}{\partial r} = 0 . \tag{2.24}$$

It follows from equations (2.7), (2.10) and (2.22) that

$$E = \frac{1}{\zeta}\left((\Sigma - 2r)\sqrt{r} + a\sin\theta\sqrt{2r^2 - \Sigma}\right) . \tag{2.25}$$

After differentiation, removal of the non-zero factors in the expression yields the condition

$$\Delta\Sigma^2 - 4r(2r^2 - \Sigma)\left(\sqrt{2r^2 - \Sigma} - a\sin\theta\sqrt{r}\right)^2 = 0\ . \tag{2.26}$$

Setting $a = 0$ gives $r = 6$, which is often regarded as the limit for the inner boundary of an accretion disk around a Schwarzschild black hole. This value is the same as that derived by Bardeen, Press & Teukolsky (1972) using $\partial^2 p_r^2/\partial r^2 = 0$.

We note that the expressions for the velocity components in equations (2.22) hold only for regions "sufficiently" far from the black-hole event horizon. The approximation adopted here breaks down when the square root in the denominator ($\zeta$) approaches zero. This occurs at the light circularisation radius $r_{\rm cir}$, which is given by $\zeta = 0$, or equivalently

$$\Sigma(r+1) - 4r^2 + 2a\sin\theta\sqrt{r(2r^2 - \Sigma)}\ \Big|_{r=r_{\rm cir}} = 0\ . \tag{2.27}$$

Moreover, the assumption that $\dot{\theta} = 0$ is also invalid for radii smaller than the radius of the marginally stable orbit, where the flow is neither pressure nor rotationally supported and it follows a geodesic into the event horizon.

## 2.3 Relativistic Radiative Transfer

The radiative transfer equation can be derived from first principles based on the conservation of particles in phase space. The space-time interval is given by

$$d\tau^2 = g_{\alpha\beta}dx^\alpha dx^\beta\ , \tag{2.28}$$

where $g_{\alpha\beta}$ is the metric, and considering a bundle of particles which fill a phase-space volume element

$$d\mathcal{V} \equiv dx\,dy\,dz\,dp^x\,dp^y\,dp^z\ , \tag{2.29}$$

where $dx\,dy\,dz(\equiv dV)$ is the three-volume and $dp^x\ dp^y\ dp^z$ is the momentum range, at a given time $t$. Liouville's Theorem reads

$$\frac{d\mathcal{V}}{d\lambda} = 0. \tag{2.30}$$

(see Misner, Thorne & Wheeler 1973), with $\lambda$ here being the affine parameter for the central ray in the bundle. The volume element $d\mathcal{V}$ is thus Lorentz invariant.

The distribution function for the particles in the bundle, $F(x^i, p^i)$ is given by

$$F(x^i, p^i) = \frac{dN}{d\mathcal{V}} , \tag{2.31}$$

where $dN$ is the number of particles in the three-volume. Since $dN/d\mathcal{V}$ is Lorentz invariant, $F(x^i, p^i)$ is Lorentz invariant. From equation (2.29),

$$F = \frac{dN}{p^2 dV\, dp\, d\Omega} , \tag{2.32}$$

where $p^2\, dp\, d\Omega = dp^x\, dp^y\, dp^z$. For massless particles, $v = c = 1$ and $|p| = E$. The number of photons in the given spatial volume is therefore the number of photons flowing through an area $dA$ in a time $dt$. It follows that

$$F = \frac{dN}{E^2 dA\, dt\, dE\, d\Omega} . \tag{2.33}$$

Recall that the specific intensity of the photons is

$$I_\nu = \frac{E dN}{dA\, dt\, dE\, d\Omega} , \tag{2.34}$$

By inspection of equations (2.33) and (2.34),

$$F = \frac{I_\nu}{E^3} = \frac{I_\nu}{\nu^3} , \tag{2.35}$$

where $\nu\ (= E)$ is the frequency of the photon. The Lorentz invariant intensity, $\mathcal{I} \equiv F$ will be used to formulate the general relativistic radiative transfer formulation.

In a linear medium, the amount of energy absorbed is proportional to the radiation intensity, and the emission is independent of the intensity of the incoming radiation. Neglecting scattering, the stationary radiative transfer equation is therefore

$$\frac{d\mathcal{I}}{ds} = -\chi\mathcal{I} + \eta\left(\frac{\nu_0}{\nu}\right)^3 , \tag{2.36}$$

where $\chi$ is the absorption coefficient, $\eta$ is the emission coefficient and $ds$ is the length element that the ray traverses. The equation in this form is defined in the observer's

frame. The absorption and emission coefficients are related to their counterparts in the rest frame with respect to the medium via

$$\chi = \left(\frac{\nu_0}{\nu}\right)\chi_0 \,, \tag{2.37}$$

$$\eta = \left(\frac{\nu}{\nu_0}\right)^2 \eta_0 \,, \tag{2.38}$$

where the subscript "0" denotes quantities in the local rest frame.

The relative energy (frequency) shift in a moving medium with respect to an observer at infinity is given by

$$\frac{E_0}{E} = \frac{\nu_0}{\nu} = \frac{k_\beta u^\beta|_\lambda}{k_\alpha u^\alpha|_\infty} \,, \tag{2.39}$$

where $u^\alpha$ is the four-velocity of the medium as measured by an observer $k^\alpha$ is the four-momentum of the photon. Define

$$\begin{aligned} \frac{ds}{d\lambda} &\equiv -\left\| \left(g^{\alpha\beta} + u^\alpha u^\beta\right) k_\alpha \right\| \Big|_\infty \\ &= -\sqrt{k^\alpha k_\alpha + 2k_\alpha k_\beta u^\alpha u^\beta + u^\alpha k_\alpha u^\beta u_\beta + u^\alpha k_\alpha}\Big|_\infty \\ &= -k_\alpha u^\alpha|_\infty \,. \end{aligned} \tag{2.40}$$

It follows that the radiative transfer equation [equation (1.29)] in the co-moving frame:

$$\frac{d\mathcal{I}}{d\lambda} = -k_\alpha u^\alpha|_\lambda \left[-\chi_0(x^\beta,\nu)\mathcal{I} + \eta_0(x^\beta,\nu)\right] \tag{2.41}$$

(see Baschek *et al.* 1997).

Results in the co-moving frame can be used to determine the intensity and frequency in any other reference frame. The ray is specified by choosing $x^\alpha(\lambda_0)$ and $k^\alpha(\lambda_0)$: an initial position, and a direction of initial propagation. From the geodesic equation, $dk^\alpha/d\lambda + \Gamma^\alpha_{\beta\gamma}k^\beta k^\gamma = 0$, $\lambda$ is scaled by $m$ for massive particles, and by 1 for massless particles. The total derivative of $\mathcal{I}$ along the world-line of the ray is therefore

$$\begin{aligned} \frac{d\mathcal{I}}{d\lambda} &= \frac{\partial\mathcal{I}}{\partial x^\alpha}\frac{dx^\alpha}{d\lambda} + \frac{\partial\mathcal{I}}{\partial k^\alpha}\frac{dk^\alpha}{d\lambda} \\ &= k^\alpha\frac{\partial\mathcal{I}}{\partial x^\alpha} - \Gamma^\alpha_{\beta\gamma}k^\beta k^\gamma\frac{\partial\mathcal{I}}{\partial k^\alpha} \,. \end{aligned} \tag{2.42}$$

This result, combined with equation (2.41), yields

$$-k_\alpha u^\alpha|_\lambda \left[-\chi_0(x^\beta,\nu)\mathcal{I} + \eta_0(x^\beta,\nu)\right] = k^\alpha \frac{\partial \mathcal{I}}{\partial x^\alpha} - \Gamma^\alpha_{\beta\gamma} k^\beta k^\gamma \frac{\partial \mathcal{I}}{\partial k^\alpha} , \tag{2.43}$$

which is the same as that derived by Lindquist (1966) from the Boltzmann Equation.

The metric and the initial conditions define the rays (the photon trajectories in 3D space), and the solution can be obtained by direct integration along the ray. For simplicity, assume that the refractive index $n = 1$ throughout the medium. The solution to equation (2.41) is then

$$\begin{aligned} \mathcal{I}(\lambda) &= \mathcal{I}(\lambda_0)\exp\left(\int_{\lambda_0}^{\lambda} \chi_0(\lambda',\nu_0) k_\alpha u^\alpha|_{\lambda'} d\lambda'\right) \\ &\quad - \int_{\lambda_0}^{\lambda} \exp\left(\int_{\lambda'}^{\lambda} \chi_0(\lambda'',\nu_0) k_\alpha u^\alpha|_{\lambda''} d\lambda''\right) \eta_0(\lambda',\nu_0) k_\alpha u^\alpha|_{\lambda'} d\lambda' . \end{aligned} \tag{2.44}$$

In the non-relativistic limit, $u^\alpha k_\alpha = 1$, and the equation recovers the conventional form of equation (1.29) (see Rybicki & Lightman 1979). However, if there is a varying refractive index in the medium, then the light will be described by a dispersion relation which modifies its propagation. The equations of motion become

$$\dot{x^\alpha} = \frac{\partial \nu}{\partial k_\alpha}, \tag{2.45}$$

$$\dot{k_\alpha} = \frac{\partial \nu}{\partial x^\alpha} \tag{2.46}$$

(Marklund 2005).

# Chapter 3

# Emission from Geometrically thin Accretion Disks

## 3.1 Radiative Transfer Algorithm

Only in the simplest, most symmetric cases is it possible to solve the radiative transfer equations analytically. In general, a numerical method is required. One method that works very well when scattering is unimportant is the method of ray-tracing.

I employ the following ray-tracing algorithm to first generate the accretion disk image in the sky plane, and then calculate its radiation.

1. Integrate the equations governing the geodesics, and those describing the optical depth for each frequency, from the observer to the emitting surface, for the opaque disks/tori; or from the observer through the emitting medium for the transparent tori.

2. Once the ray hits the emitting object, or the optical depth for each observed frequency reaches some large cutoff, stop the integration.

3. Construct an image using each ray as a pixel.

4. Sum the emission over the pixels in the image to produce the observed spectrum.

I use a hybrid algorithm for integrating along the ray trajectory. In general, I use a Runge-Kutta integrator. The relative tolerance is set to $10^{-11}$, which causes it to take small steps. It samples a volumetric emitter or absorber well when that emitter/absorber varies on scales comparable to the black hole geometry, which is the case for models investigated in this thesis. For regions with slowly varying properties, a sparse sampling is sufficient to achieve the required accuracy. It allows a simple Eulerian method to be used to integrate the optical depths which increases the computational speed by orders of magnitude.

The foot points of the null geodesics (photon trajectories) on the accretion disk surface are calculated by a root-finding algorithm (see e.g. Press *et al.* 1992, p.343). The first four intersections of the null geodesics and the disk plane (corresponding to the direct and first three higher-order images), and the four-vectors of the photons emitted from there are recorded. The incorporation of an emissivity law is straightforward, as it is defined in terms of the spatial coordinates on the disk plane. Since the trajectory of the photon is also saved at each disk crossing point, I can include the effects of limb darkening, and to model a semi-transparent disk.

As the disk is projected onto a sky plane, all gravitational lensing effects on the intensity of the light are implicitly included in the image calculation. If a region of the disk is magnified then it will cover more area in the image, and thus will emit more flux than an unmagnified region. Inclination effects are also included implicitly. An inclined disk will cover less pixels than a face-on disk, where the number of pixels is roughly proportional to $\cos i$, where $i$ is the inclination angle. (Because of light bending, this Euclidean formula is only an approximation.) Gravitational lensing does not alter the observed surface brightness of an emission element.

As the method implicitly includes the changing areas of photon flux-tubes linking the observer to the emitter, the calculation of observable flux is greatly simplified. All that is required is to integrate over each pixel on the image, taking into account

the redshift of the emission regions corresponding to the pixels. If one integrates the emission over the surface of the disk, instead of over the image, then the Jacobian of the transformation from the disk to the image plane coordinates would be required. This is numerically difficult, and it requires a separate transformation for the images of each order.

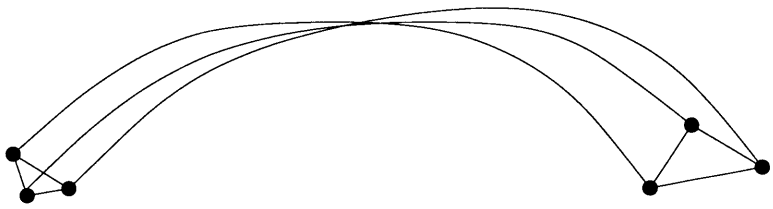

Figure 3.1: Schematic photon trajectories connecting area elements on the surface of the emitting object to areas on the sky plane. Gravitational lensing alters the apparent relative size of those area elements.

The radiative transfer equation is not fully time-symmetric. If one follows rays back from the observer to the emitter then equation (2.41) cannot be used as it stands. The emission frequency and intensity are unknown until the emitter is reached somewhere along the ray path. This problem can be solved using one of two approaches. The first, is to collate the path from emitter to observer, and then to integrate along that path forward in time using equation (2.44). The second is to collate the optical depth for $\mathcal{I}$ for a table of frequencies as one travels back in time. This optical depth can then be used to calculate the observed intensity, $I$, for each binned frequency. The results for each emission element along the path are simply summed.

The resulting emission must be binned over frequency to calculate a spectrum. I therefore choose the second method. It requires less storage space in computation, and the formulation is effectively an extension of the grey-absorber case in which $\chi_0$ and $\eta_0$ are frequency independent. Summation over the observed frequencies, rather than those in the rest frame, avoids the need to transform the distribution of frequencies along the path due to gravitational redshifts. As the mapping from

an emission frame to the observer's frame affects the intensity $I$, the invariant $\mathcal{I}$ is used instead.

The programs (written in FORTRAN) take a few hundred kilobytes of memory under Tru64 Unix on a OSF1 V5.1 1885 Alpha. One version outputs the intensity and frequency shift of the emission line for each 'pixel' in the sky plane. Another version collates the continuum as well as the line, and outputs a table of intensity verses energy integrated over the whole disk. Depending on the load on the shared computer system, and on the image size requested, a typical run takes up to a few hours per image with $1000 \times 1000$ pixels.

## 3.2 Disk Emission

When space-time curvature is important, the Keplerian angular velocity of a test particle around a gravitating object is no longer $\Omega_{\rm K} = r^{-3/2}$ . Instead, the Keplerian angular velocity in a plane containing the gravitating object can be obtained by setting $\theta = \pi/2$ in equations (2.22) and (2.23). Hence, the components of the four-velocity of the particles in an accretion disk around a Kerr Black hole are

$$\begin{aligned} \dot{t} &= \frac{r^2 + a\sqrt{r}}{r\sqrt{r^2 - 3r + 2a\sqrt{r}}} , \\ \dot{r} &= 0 , \\ \dot{\theta} &= 0 , \\ \dot{\phi} &= \frac{1}{\sqrt{r}\sqrt{r^2 - 3r + 2a\sqrt{r}}} , \end{aligned} \tag{3.1}$$

and the rotational velocity is

$$\Omega_{\rm K} = \frac{1}{r^{3/2} + a} \tag{3.2}$$

(Bardeen, Press & Teukolsky 1972).

The relative energy shift of the emission between the disk particle and an observer at a large distance is determined by equation (2.39), with $u^\alpha$ as given in equation (3.1). Keplerian disk images can be found in many existing works (e.g. Bromley,

Miller & Pariev 1998). In most of the studies, the inner edge of the disk was set at the marginally stable orbit. Maximally rotating Kerr black holes have disks that extend close to the event horizon, where gravitational and transverse redshifts are large. However, for disks with viscosity due to MRI, due to magnetic effects, this location of the inner boundary might not be correct. Krolik & Hawley (2002) showed that the location of the 'radiation edge', the smallest radius where significant flux originates, is strongly dependent on the detailed energetics of the accretion flow. It can possibly reside on either side of the marginally stable orbit. For simplicity, and to compare my results with others (i.e. Fanton *et al.* 1997; Fabian *et al.* 1989), I have ignored this complication, and chose the inner edge to be at $r_{\rm ms}$, the marginally stable orbit instead.

When relativistic effects are important the a disk image in the sky plane is characteristically asymmetric. Figure 3.2. shows what an accretion disk would look like around a Schwarzschild black hole with an outer radius of $100R_{\rm G}$. The emissivity has a radial power-law distribution with an index of $-2$. The image of the disk is distorted by gravitational lensing, and at high inclinations the bottom of the disk comes into view as an indirect image. In addition, there is a faint inner ring surrounding the black hole in the middle of the image which is the first higher order image. Due to transverse and gravitational redshift, the separatrix for the observed energy shift no longer bisects the disk image into two equal sectors.

Figure 3.3. shows the disks with an outer radius of $20R_{\rm G}$. The central object is still a Schwarzschild black hole as in the cases shown in Fig. 3.2.. The indirect emission is now clearly seen as the thin ring in the middle of the pictures. These images show the indirect flux is generally negligible for inclination angles smaller than 80°.

Figures 3.4. and 3.5. show the disk images for black holes with spin parameter $a = 0.5$ and $a = 0.998$ respectively. The images are more asymmetric than the disks around Schwarzschild black holes because the frame-dragging from the black hole breaks the left-right symmetry. This is most noticeable in the centre of the

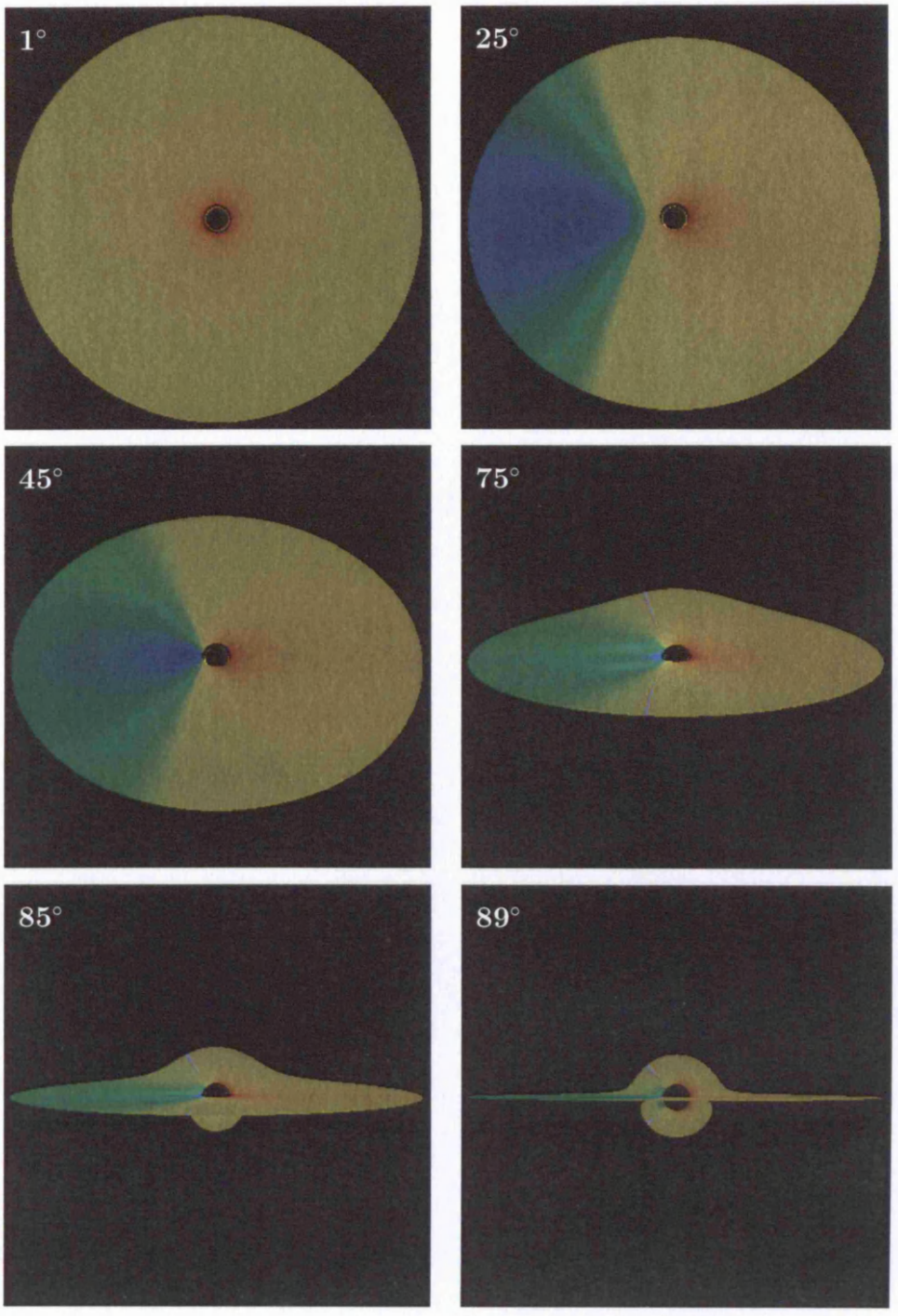


Figure 3.2: False-colour Doppler shift images of accretion disks around Schwarzschild black holes. The inner edge of the accretion disk is at the marginally stable orbit. The outer edge is set to be $100R_G$. The disk is viewed at inclination angles of $1°, 25°, 45°, 75°, 85°$ and $89°$. The emissivity power-law index is $-2$. Blue represents energy upshift; red represents energy downshift. The separatrixes (areas with no energy shift) are denoted by the grey lines. Note that due to dynamic range issues, the images have been normalized such that the brightest pixel in each image is the same intensity.

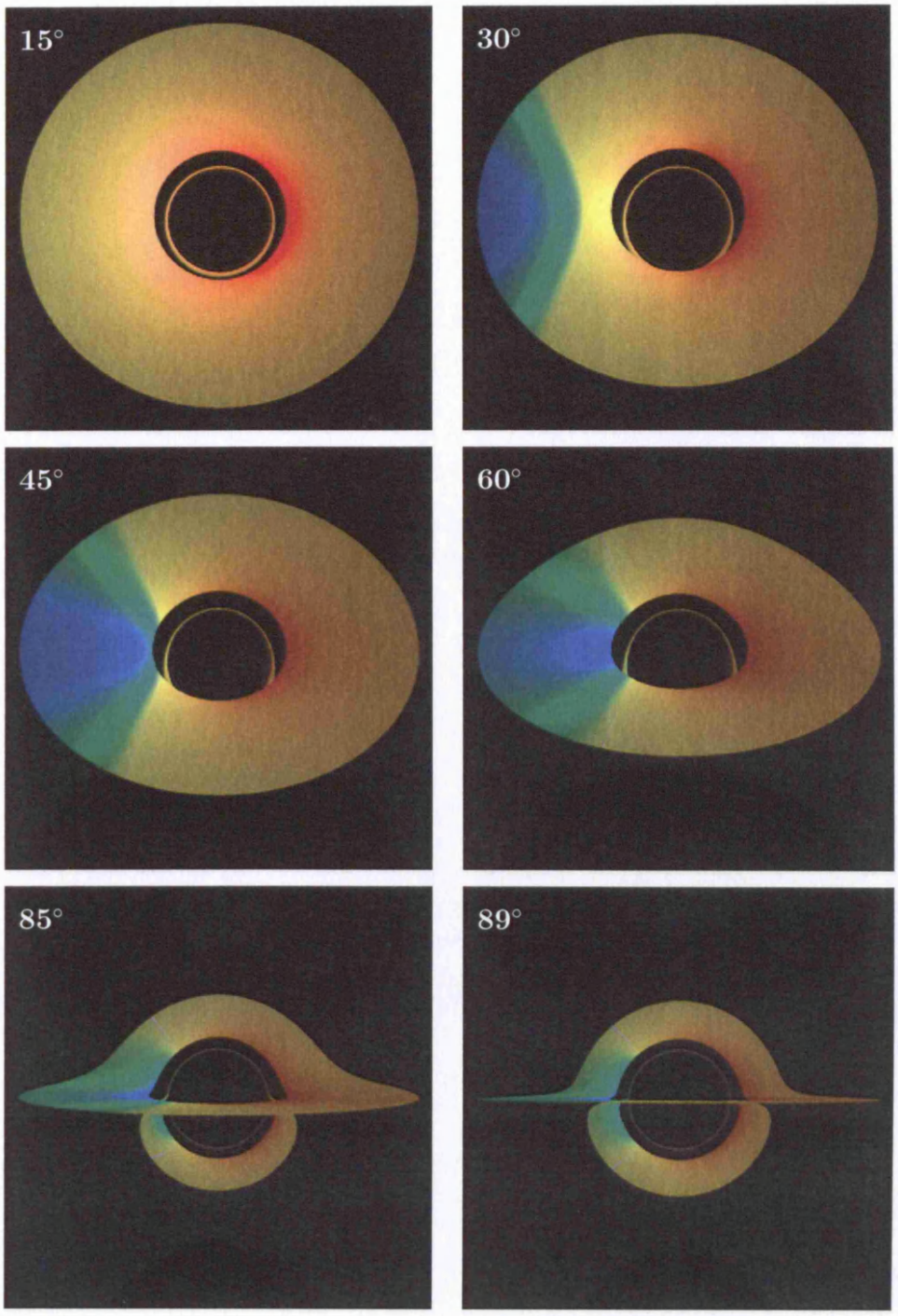


Figure 3.3: False-colour Doppler shift images of accretion disks around Schwarzschild black holes. The inner edge of the accretion disk is at the marginally stable orbit. The outer edge is set to be $20R_G$. The disk is viewed at inclination angles of $15°, 30°, 45°, 60°, 85°$ and $89°$. The emissivity radial power-law index is $-2$. Note that due to dynamic range issues, the images have been normalized such that the brightest pixel in each image is the same intensity.

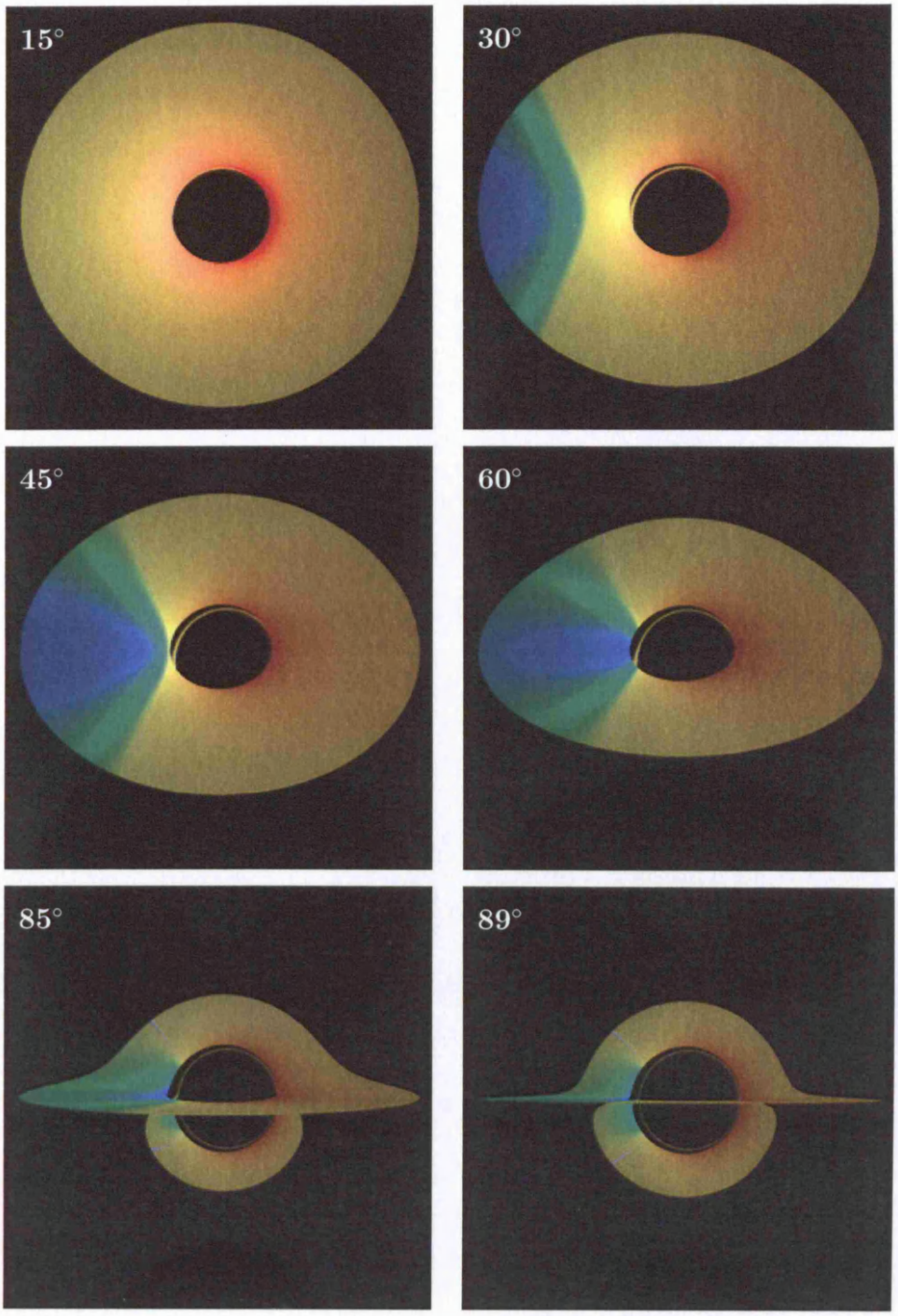


Figure 3.4: False-colour Doppler shift images of accretion disks around Kerr black holes with spin parameter $a = 0.5$. The inner edge of the accretion disk is at the marginally stable orbit. The outer edge is set to be $20R_G$. The disk is viewed at inclination angles of $15°, 30°, 45°, 60°, 85°$ and $89°$. The emissivity radial power-law index is $-2$. Note that due to dynamic range issues, the images have been normalized such that the brightest pixel in each image is the same intensity.

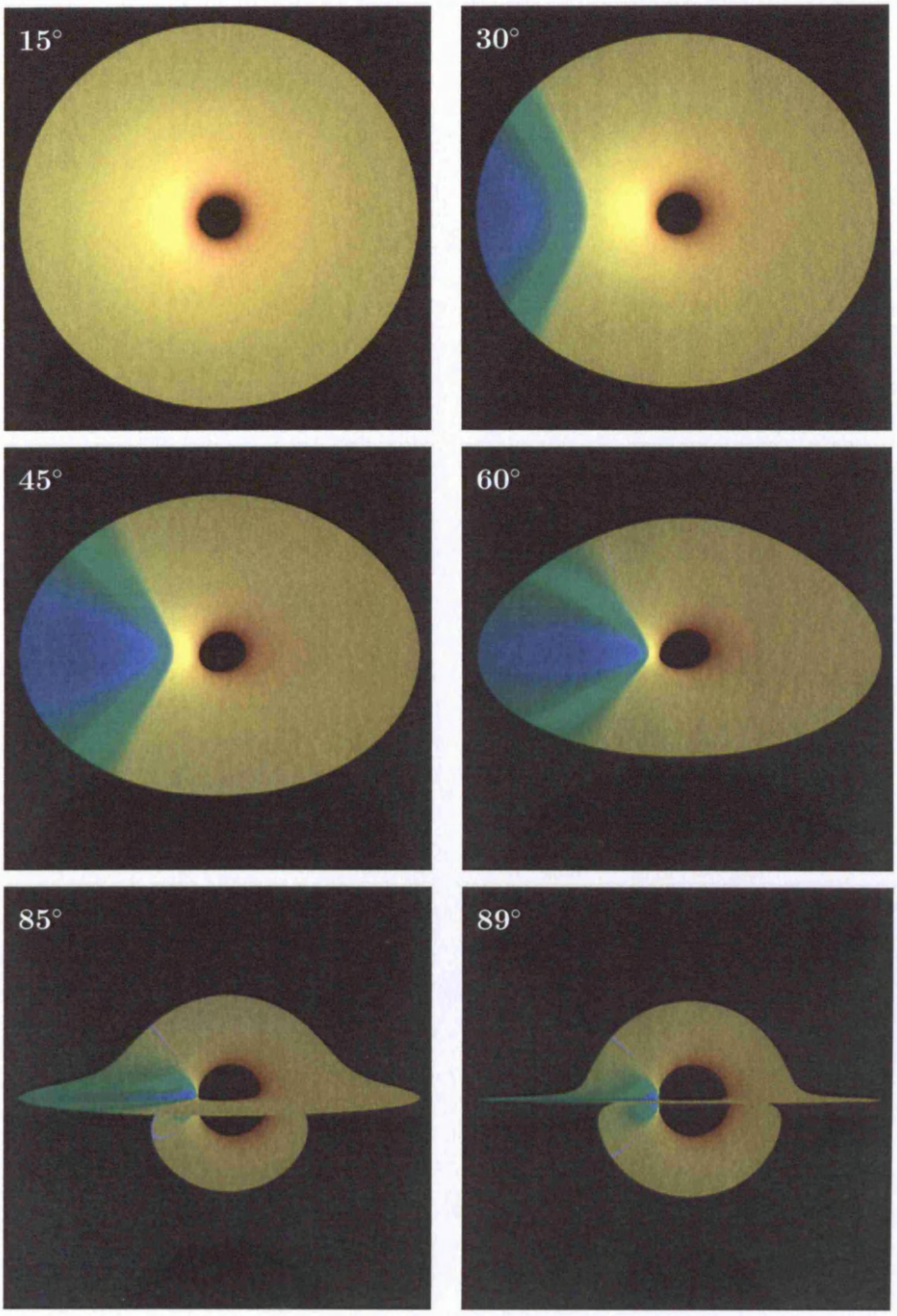


Figure 3.5: False-colour Doppler shift images of accretion disks around Kerr black holes with spin parameter $a = 0.998$. The inner edge of the accretion disk is at the marginally stable orbit. The outer edge is set to be $20R_G$. The disk is viewed at inclination angles of $15°, 30°, 45°, 60°, 85°$ and $89°$. The emissivity radial power-law index is $-2$. Note that due to dynamic range issues, the images have been normalized such that the brightest pixel in each image is the same intensity.

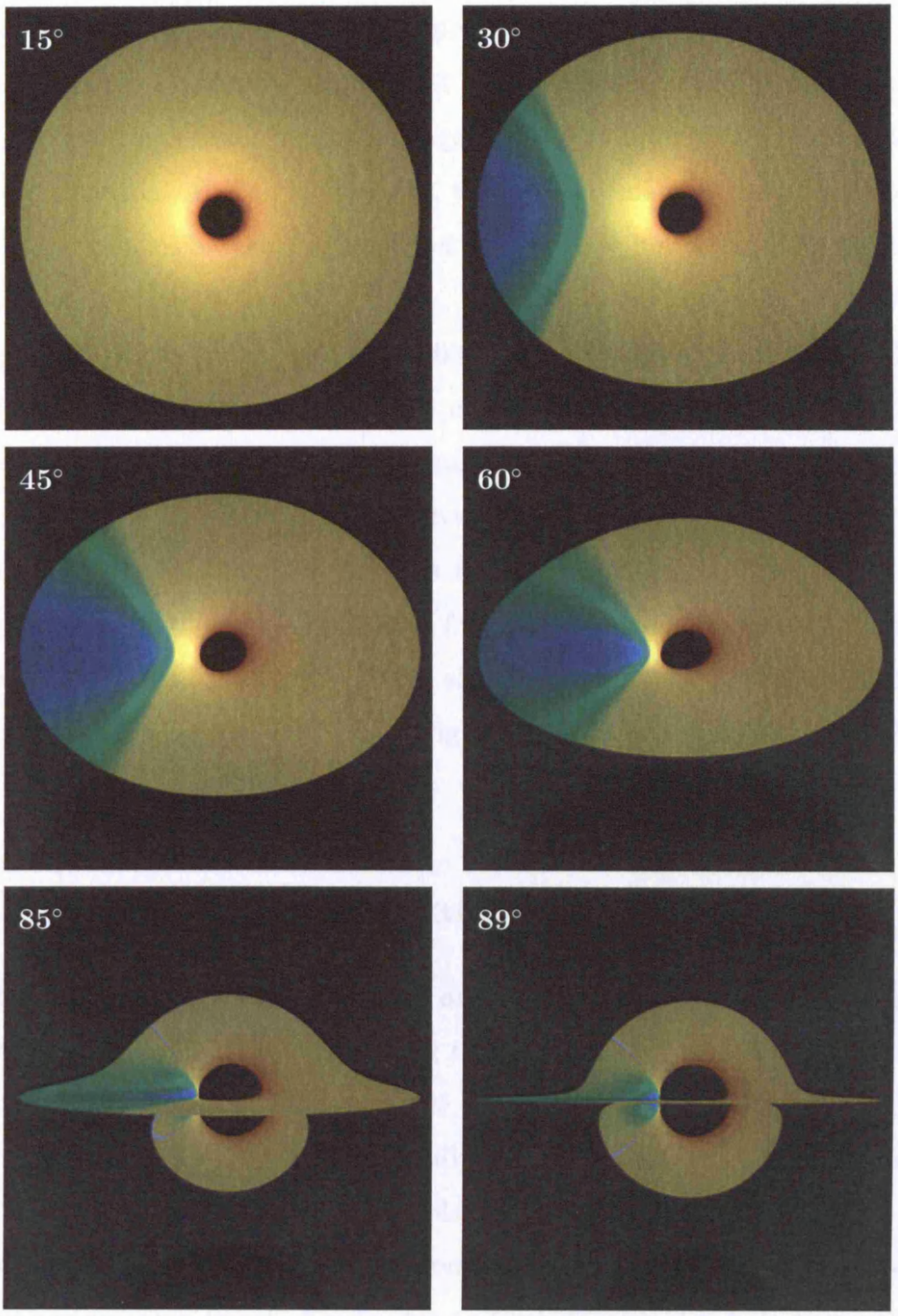


Figure 3.6: False-colour Doppler shift images of accretion disks around Kerr black holes with spin parameter $a = 0.998$. The inner edge of the accretion disk is at the marginally stable orbit. The outer edge is set to be $20R_G$. The disk is viewed at inclination angles of $15°, 30°, 45°, 60°, 85°$ and $89°$. The emissivity radial power-law index is $-3$. Note that due to dynamic range issues, the images have been normalized such that the brightest pixel in each image is the same intensity.

images. The apparent shape of the marginally stable orbit appears to be somewhat squashed. As the marginally stable orbit is much closer to the black hole in these cases, the inner high order indirects images are partially or totally obscured at low viewing inclination. At high inclinations, the indirect image at the bottom becomes visible. The conclusion that higher order images only matter at large inclinations does not change.

Figure 3.6. shows a disk with the radial emissivity power-law index of $-3$. Note that if the accretion disk with a radial emissivity power-law index of $-2$ has an infinite outer radius, there will be an infinite amount of flux observed from that disk. This is due to the logarithmic divergence in the flux integral. The power-law with index $-3$ weights the emission from the inner part of the accretion disk much more, and so the flux is finite even for an infinitely extended disk. Comparing the disks in Fig. 3.5. and Fig. 3.6. shows the centrally-dominated weighting, particularly at low inclinations. The 'bright' area of the accretion disk in Fig. 3.6. is much closer to the centre in Fig. 3.5.

## 3.3 Line Profile Calculations

The observable energy of the flux from any point on the planar disk is calculated using equation (2.39). Absorption along the ray-paths is ignored for these models. The line emissivity has a power-law profile, which decreases radially from disk centre. Figures 3.6. and 3.11. show the centrally dominant case where the power-law is $\mathcal{I}(\lambda_0) \propto r^{-3}$, and the rest of the models use an 'equal weighting', $\mathcal{I}(\lambda_0) \propto r^{-2}$, emissivity law. The intensity is proportional to the third power of the relative shift; the flux has an extra factor of $\nu_0/\nu$ due to time dilation, i.e. it is proportional to the fourth power of the relative frequency shift.

The line profiles are obtained from $750 \times 750$ pixel images. The intensity scale on the graphs in this chapter is in arbitrary units. (It is the sum of pixel intensity over the image, as a function of energy.) The $x$-axis of the graph is in units of the

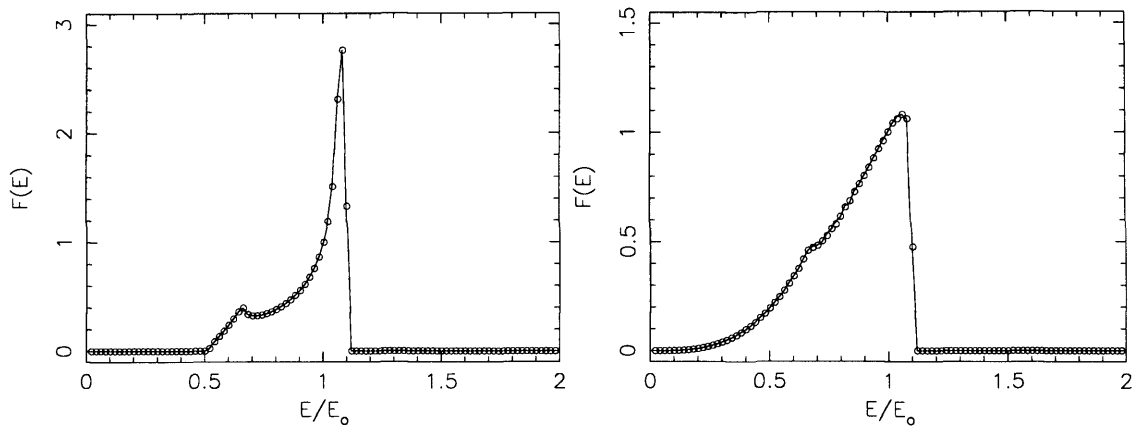


Figure 3.7: The profiles of emission lines from thin Keplerian accretion disks around a Schwarzschild black hole (left) and a Kerr black hole with $a = 0.998$ (right). The line profiles are normalised such that the flux $F(E) = 1$ at $E/E_0 = 1$. The viewing inclination angle is 45°. The inner radius of the accretion disk is at the last stable orbit, and the outer radius is $10R_G$. The line emissivity on the disk surface is a power-law which decreases radially outward, and the power-law index is $-3$. Only emission contributed by the direct disk image is considered; emission from higher-order images is not included. The solid lines correspond to the line profiles obtained by semi-analytic calculations described in Fanton *et al.* (1997), and the circles represent the line profile obtained by numerical ray-tracing calculations described in this chapter.

line rest energy, with $E/E_0 = 1$ corresponding to the unshifted line.

The resulting line profiles are distorted from the delta function at emission into double-peaked or "horn" shapes (see Fabian *et al.* 1989). In some cases there is a third peak where the indirect images contribute significant amounts of flux. This tends to produce a bump at the line rest frequency.

In general, the line is wedge-shaped due to the "Doppler boosting" effect enhancing the intensity of the blue wing relative to the red. The blue cutoff is sharp, and depends mostly on the observer's inclination angle. The shape and cutoff of the red wing depends mostly on the location of the inner edge of the accretion disk.

My calculation reproduces the line profiles shown in Fabian *et al.* (1989), Kojima (1991), Fanton *et al.* (1997), Bromley *et al.* (1997), and Reynolds *et al.* (1999). Figure 3.7. shows the comparison of line profiles from my numerical calculations, and profiles obtained by using the analytic method described in Fanton *et al.* (1997).

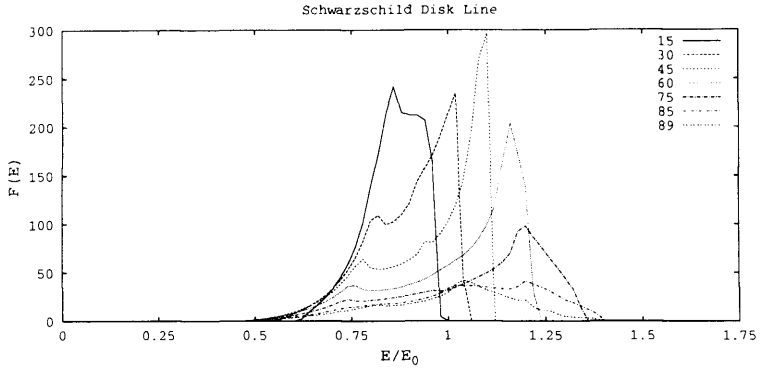


Figure 3.8: Line profiles from accretion disks around Schwarzschild black holes. The disk parameters are the same as those in figure 3.3. The viewing inclination ranges from 15° to 89°. The fluxes are in arbitrary units.

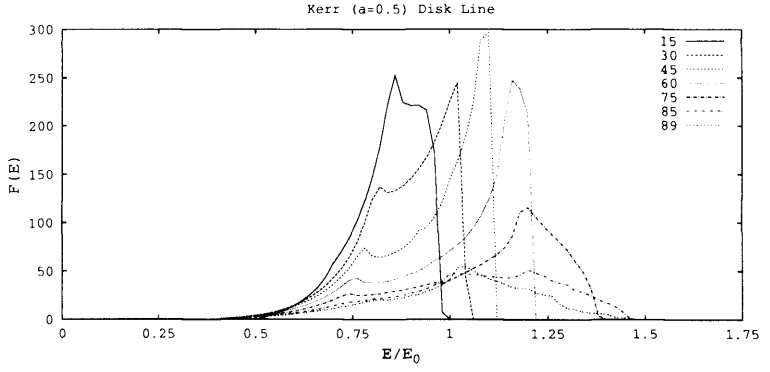


Figure 3.9: Line profiles from the accretion disks around Kerr black holes with $a = 0.5$. The disk parameters are the same as those in figure 3.4. The viewing inclination ranges from 15° to 89°. The fluxes are in arbitrary units.

The results in the two calculations are in excellent agreement.

Figures 3.8. to 3.11. shows the line profiles produced from the disk images in Fig. 3.3. to 3.6. respectively. The distinctive double-horn profiles can be seen. Increasing the black hole spin to $a = 0.5$ and $a = 0.998$ do not alter the shapes very much at low inclinations. The line profile may however change substantially with $a$ at high inclination. Note that the location of the extreme red wing changes. This is due to the location of the marginally stable orbit changing with black hole spin

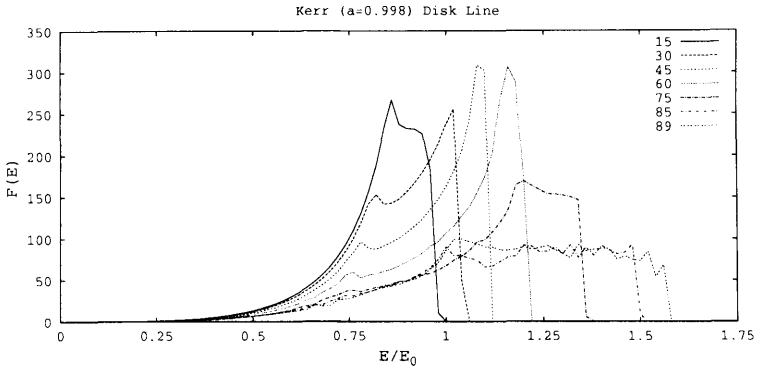


Figure 3.10: Line profiles from the accretion disks around Kerr black holes with $a = 0.998$. The disk parameters are the same as those in figure 3.5.. The viewing inclination ranges from 15° to 89°. The fluxes are in arbitrary units.

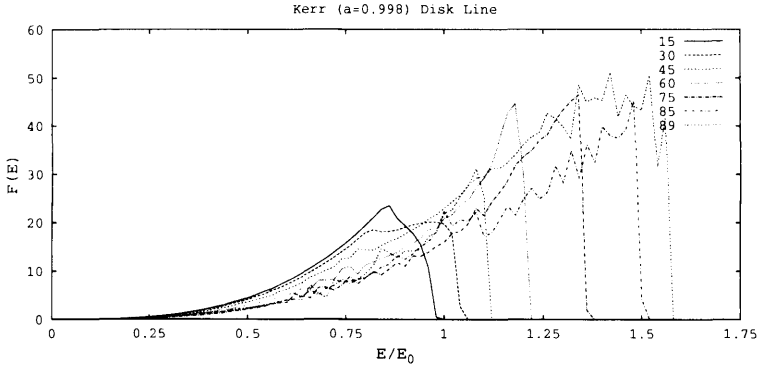


Figure 3.11: Line profiles from the accretion disks with the same parameters as those in figure 3.6., which differ by varying observer inclinations which range from 15° to 89°.

rate. Because the inner edge of the accretion disk moves inwards as the spin rate is increased, there is greater gravitational and transverse redshift in the inner part of the disk. However, the changes the line profiles at high inclination are mainly due to the different locations of the inner edge of the accretion disk. Most of the blue emission comes from a tiny spot on the accretion disk surface. The most blue-shifted part of the disk when $a = 0.998$ is inside the inner orbit when $a = 0.5$. This extra emission, highly magnified by the Doppler boosting effect, gives rise to the changes in the location of the cutoff of the blue wing of the line profile.

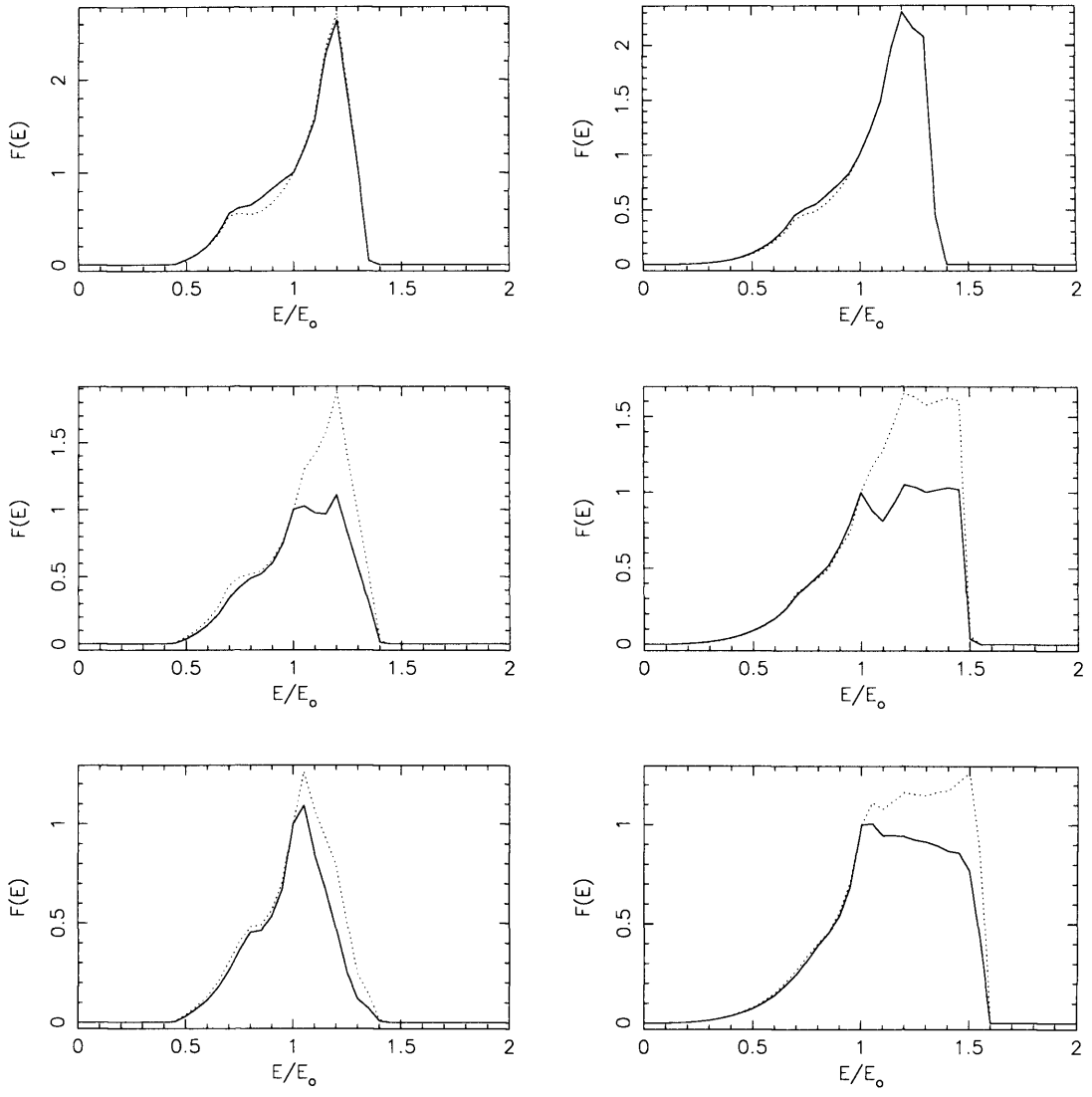


Figure 3.12: Comparison of the line profiles for cases considering only the direct disk image (dotted line) and cases including high-order images (solid line). The line profiles are normalised such that $F(E) = 1$ at $E/E_0 = 1$. The viewing inclination angles of the disks are 75°, 85° and 89° (panels from top to bottom). Line profiles for Schwarzschild black holes are shown in the left column; line profiles for the Kerr black holes with $a = 0.998$ are shown in the right column. The outer radius of the accretion disk is $20R_G$, and the index of the emissivity power-law index is $-2$.

Changing the emissivity power-law index also changes the line profile, especially at high inclination, as is seen in Fig. 3.11. The double-horned profile now becomes a wedge-like profile when the index decreases from $-2$ to $-3$. The centrally dominated emissivity law emphasises emission from the inner region of the disk where the gas is moving the fastest. This reduces the flux coming from the relatively sedate outer disk, and hence reduces the flux near the line rest frequency.

Note that the contribution of the higher-order images are significant only at high inclination angles (see Fig. 3.12.). The emission from high-order images is mostly at frequencies close to the rest frequency of the line, because the regions where highly red and blue-shifted emission originate are obscured.

## 3.4 Absorption

This section investigates systems in which there are emitters of various strengths situated in the equatorial plane of the Kerr metric, and there is a volumetric absorber outside that plane. As light propagates through the medium to the observer it may be absorbed by material along the line of sight. The emitters and the absorbers are in relativistic motion with respect to the observer and also with respect to each other. An example is illustrated schematically in Fig. 3.13., in which the emitters are the surface elements of an accretion disk and the absorbers are some clouds in the vicinity of the disk. The photon trajectories and the motion of the emitters and absorbers are affected by space-time distortions due to the central black hole. A particular process of importance in studying the X-ray line from AGN is the resonant scattering/absorption process. This process removes energy from an emission line, and redistributes it into other lines, or into the continuum. Assume that the radiation scattered into the energies of the line is insignificant. We may then ignore the line photons that are scattered into the line-of-sight. Hence scattering simply removes the line photons and causes extinction similar to true absorption. This assumption is justified because the energy lost in the line goes into

the continuum. When the flux of the continuum a t the line energies is larger than the line flux, the change in the shape of the continuum will be negligible.

Thus, hereafter I do not distinguish between resonant scattering and resonant absorption in this chapter. The two terms will be interchangeable, unless otherwise stated explicitly. In other words, despite using the term "resonant scattering" (which describes the nature of the process), I have not considered the scattering of continuum photons into the line energy bins and the energy (frequency) redistribution in my calculations.

### 3.4.1 An illustrative model

In constructing my disk within medium model, it involves determining:

(i) the rays that connect the emitters, absorbers and observer,

(ii) the four-velocities of the emitters and absorbers /scatterers,

(iii) the spatial distributions of the emitters and the absorbers/scatterers, and

(iv) the effective cross section of the absorbers/scatterers.

In the previous chapter, I have shown how to obtain (i) and (ii); in this chapter I incorporate (iii) and (iv) into the radiative-transfer calculations. I consider a model with the geometry shown in Fig. 3.13. The photons are emitted from the elements on the top and bottom surfaces of a geometrically thin disk undergoing a Keplerian rotation around a Kerr black hole. The radiation is resonantly scattered (absorbed) by plasma clouds and is attenuated in its propagation. This study omits emission from the clouds [i.e. $\eta_0 = 0$ in equation (2.41)]. The size of the clouds is small compared to the length scale of the system. They are not confined to be in the equatorial plane, and they are in orbital motion supported by some implicit forces (which may be radiation, kinematic or magnetic pressure gradients). These clouds have a large (thermal) distribution of velocities, in addition to their collective bulk velocity. See Fuerst & Wu (2004) for further discussion of this model.

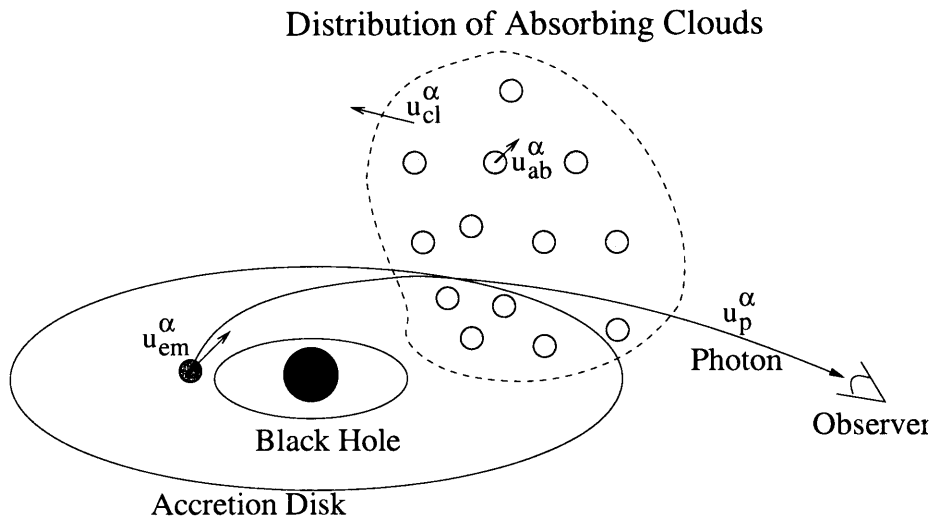


Figure 3.13: A schematic illustration of the physical setting within which the radiative-transfer formulation is constructed. The space-time curvature is determined by a gravitating body, which is a rotating black hole. The emitting object is the accretion disk around the hole. The cloudlets in the vicinity attenuate the radiation from the accretion disk. The properties of the radiation are specified by the 4-velocity of the photon, $u_{\rm p}^{\alpha}$. The other three important quantities in the model are the 4-velocity of emitting elements in the accretion disk $u_{\rm em}^{\alpha}$, the bulk velocity of the absorbing cloudlets $u_{\rm cl}^{\alpha}$ and the "microscopic" 4-velocities of the cloudlets $u_{\rm ab}^{\alpha}$ with respect to the bulk motion of the cloudlets.

The 4-momenta of the photons determine which of the rays originating from the accretion disk surface can actually reach the observer. The photon 4-momenta, $k_{\alpha}$, are calculated using equations (2.7), (2.10) and (2.13). The 4-velocities of the emitting surface elements on the accretion disk are given by equations (3.1). These determine the relative energy shifts of the photons between the emitters and the observer. Next, I determine the relative energy shifts between the emitters and the absorbers. Then, I derive the resonant absorption condition for the absorption coefficient, and use it to model the absorption mechanism

What follows is the construction of a model for the spatial distribution and the velocities of the absorbers. I consider a parametric model in which the bulk 4-velocities of the clouds are given by equations (2.22) and (2.23). In this model the bulk velocities of the clouds in the equatorial plane match the 4-velocities of the

accretion disk. The gas inside the clouds is cold, and the thermal velocity of the gas particles are much smaller than the clouds bulk motion. However, the distribution of clouds has a large velocity dispersion, given by the local virial temperature, which is comparable to the energy of the emission lines of interest. Therefore, the clouds can be considered as relativistic particles in the calculation. Using the bulk-motion velocities obtained by equations (2.22) and (2.23) together with the virial theorem, I derive this temperature and determine the velocity distribution of the absorbing clouds. The clouds fill most of space, with a radially dependent number density.

However, close to the black hole, the assumptions above break down, and the axial force cannot support the clouds out of the equatorial plane. When this happens, I assume the particles will flow along geodesics directly into the hole. In the numerical calculation, I determine the asymptotic boundaries at which the left hand sides of equations (2.27) and (2.26) vanish. This is achieved by evaluating these expressions and testing to see if they are negative at each point along the photon rays. Inside that surface, I set the number density to zero for simplicity given that it must be much less than that outside.

### 3.4.2 The absorption coefficient

I assume that the absorption is due to an ensemble of "cold" cloudlets with high virial velocities. The absorption coefficient of an individual cloudlet, $i$, is

$$\chi_{\rm i} \propto \sigma\, \delta\left(\frac{u^\alpha k_\alpha + E_{\rm line}}{E_\gamma}\right), \tag{3.3}$$

with $\sigma$ as the effective absorption cross section of the cloudlet, and $k_\alpha$ the photon four-momentum. The absorption rest frequency is $E_{\rm line}$, and $E_\gamma$ is the energy of the photon in the bulk rest frame. $\delta(...)$ is the Dirac delta function. The total effective absorption coefficient $\chi_0$ is the sum of the contribution of these cloudlets, i.e. ,

$$\chi_0 = \sum_{\rm i} \chi_{\rm i} \,. \tag{3.4}$$

Converting the sum into an integral in momentum space yields the absorption per unit length in the rest frame:

$$\chi_0 = \frac{-2\pi C\sigma}{E_{\rm line}^2} \times \iint p^2 dp\, d\mu \exp(-E/\Theta) u^\alpha k_\alpha\, \delta\left(\frac{u^\alpha k_\alpha + E_{\rm line}}{E_\gamma}\right), \quad (3.5)$$

where $\mu \equiv \cos\theta$, $C$ is a normalisation constant, $\Theta$ is the temperature in units with $k_{\rm B} = 1$, and $E$ and $p$ are the energy and momentum of a gas particle in the bulk rest frame. (This functional form of $\chi_0$ assumes isotropic thermal motion in the rest frame.)

There are three terms to be determined before evaluating the integral. They are the normalisation parameter $C$, the temperature $\Theta$ and the photon energy in the rest frame of the absorbing particle, $u^\alpha k_\alpha$. When these variables are determined, we can parametrise $\sigma$ after carrying out the integration.

### The normalisation $C$

Consider

$$N = 4\pi C \int_0^\infty p^2 dp \exp\left(-E/\Theta\right) , \quad (3.6)$$

where $N$ is the number density of absorbing clouds. This is called the Jüttner distribution and corresponds to Maxwell's distribution except in the case of a relativistically high temperature. Integration of equation (3.6) yields

$$C = \frac{N\frac{m}{\Theta}}{4\pi m^3 K_2(\frac{m}{\Theta})} , \quad (3.7)$$

where $K_z(...)$ is a modified Bessel function of order $z$, and $m$ is the average cloud mass.

### The temperature $\Theta$

The total energy in the distribution of clouds is given by

$$E_{\rm tot} = 4\pi C \int_0^\infty p^2 dp\; E \exp\left(-E/\Theta\right) . \quad (3.8)$$

Integrating this yields the energy per unit mass as

$$\frac{E_{\rm tot}}{Nm} = \frac{K_3(\frac{m}{\Theta})}{K_2(\frac{m}{\Theta})} - \frac{\Theta}{m} \ . \tag{3.9}$$

Applying conservation of energy and angular momentum, yields the thermal energy of the virialised relativistic gas of absorbing cloudlets. At infinity the cloudlets have

$$E_{\rm init} = Nm \ , \tag{3.10}$$

$$L_{\rm init} = L_{\rm fin} \ . \tag{3.11}$$

Close to the black hole

$$E_{\rm fin} = \frac{Nm}{\zeta}\left[(\Sigma - 2r)\sqrt{r} + a\sin\theta\sqrt{2r^2 - \Sigma}\right] \ , \tag{3.12}$$

$$L_{\rm fin} = \frac{Nm}{\zeta}\left[2ar\sqrt{r}\sin^2\theta - (r^2 + a^2)\sin\theta\sqrt{2r^2 - \Sigma}\right] \ . \tag{3.13}$$

The energy released by the gas falling from infinity and slamming into a wall moving with a velocity given by equation (2.22) is

$$-E_{\rm tot} = u^\alpha p_\alpha = -E_{\rm fin}\dot{t}_{\rm init} - L_{\rm fin}\dot{\phi}_{\rm init} \ . \tag{3.14}$$

It follows that

$$-\frac{E_{\rm tot}}{Nm} = \frac{1}{\zeta^2}\Big[(2r^2 - \Sigma)(r^2 + a^2) - 2ar\sin\theta\sqrt{r}\sqrt{2r^2 - \Sigma} - \left(a\sin\theta\sqrt{2r^2 - \Sigma} + \Sigma\sqrt{r}\right)\zeta\Big] \ . \tag{3.15}$$

The temperature of the media can be derived using equations (3.9) and (3.15). This yields an implicit relation of $m/\Theta$ that contains transcendental functions. The modified Bessel functions can be expanded in the limit where $\Theta \ll m$ which corresponds to an "almost relativistic" gas. Since the potential energy released in accretion is of the order of a few percent of the rest mass of the infalling material, this approximation should hold in AGN.

Expanding to second order in $\Theta/m$, cancelling the exponential factors, and then solving the resulting quadratic yields

$$\frac{\Theta}{m} \simeq \frac{2}{5}\left(-1+\sqrt{1+\frac{10}{3}\left(\frac{E_{\rm tot}}{Nm}-1\right)}\right) . \tag{3.16}$$

This is an explicit description of how the cloudlets' kinematic temperature.

### The photon energy $u^\alpha k_\alpha$

We assume the motion of the thermalised medium is isotropic in the local rest frame. Thus we may align an axis along the photon propagation vector and evaluate quantities in a local Lorentz frame, so that

$$k_\alpha = E_\gamma(-1,1,0,0) , \tag{3.17}$$

and

$$p^\alpha = mu^\alpha = (E, p\mu, p_{\rm y}, p_{\rm z}) . \tag{3.18}$$

Hence, we obtain

$$u^\alpha k_\alpha = \frac{E_\gamma}{m}(p\mu - E) . \tag{3.19}$$

### Evaluation of the $\delta-$function

Using the relation

$$\frac{d}{d\mu}\left[\frac{u^\alpha k_\alpha + E_{\rm line}}{E_\gamma}\right] = -\frac{p}{m} , \tag{3.20}$$

we evaluate the integral:

$$\begin{aligned}\int d\mu\, u^\alpha k_\alpha \delta\left(\frac{u^\alpha k_\alpha + E_{\rm line}}{E_\gamma}\right) &= \frac{u^\alpha k_\alpha}{\left|\frac{d}{d\mu}\left[\frac{u^\alpha k_\alpha + E_{\rm line}}{E_\gamma}\right]\right|}\Bigg|_{u^\alpha k_\alpha = -E_{\rm line}} , \\ &= -E_{\rm line}\frac{m}{p}\Big|_{u^\alpha k_\alpha = -E_{\rm line}} . \end{aligned} \tag{3.21}$$

Equation (3.5) can now be simplified to

$$\chi_0 = \frac{2\pi C\sigma m}{E_{\rm line}} \int_{\frac{m}{2}\left(\frac{E_\gamma}{E_{\rm line}}+\frac{E_{\rm line}}{E_\gamma}\right)}^{\infty} E\, dE \exp(-E/\Theta), \tag{3.22}$$

after changing variable from $p\ dp$ to $E\ dE$. This gives the absorption coefficient in the rest frame of the gas

$$\chi_0 = \frac{N\sigma}{2K_2(\frac{m}{\Theta})}\left[\frac{1}{2}\left(\frac{E_\gamma}{E_{\rm line}}+\frac{E_{\rm line}}{E_\gamma}\right)+\frac{\Theta}{m}\right]\times \exp\left[-\left(\frac{m}{2\Theta}\right)\left(\frac{E_\gamma}{E_{\rm line}}+\frac{E_{\rm line}}{E_\gamma}\right)\right] . \quad (3.23)$$

This equation can be expressed in terms of $\chi$ using equations (2.37) and (2.39).

**The effective absorption $N\sigma$**

The absorption coefficient depends upon $N$, the number density of the cloudlets, and on $\sigma$, the absorption cross-section per cloudlet. These are functions of position. Since the pressure gradient and the inflow velocity in the $\hat{r}$ and $\hat{\theta}$ directions are ignored in the present flow approximation, the density profile cannot be determined in a fully self-consistent manner via the mass continuity equation. To overcome this, assume a simple two-parameter profile

$$N\sigma = \sigma_0 r^{-\beta} , \quad (3.24)$$

where $\sigma_0$ can be considered as a normalisation constant fixing the density and opacity scales. Without losing generality, we consider the case with an illustrative value $\beta = 3/2$ in my calculations. The results can then easily be generalised to other values of $\beta$, or in fact to any other function of $r$ and $\theta$.

### 3.4.3 Results

The following disk model is used to illustrate the effects of resonant absorption. The marginally stable orbit is taken as the inner edge of the accretion disk, and the outer edge is assumed to be at a radius of $20R_{\rm G}$. This was chosen to accentuate the relativistic effects. The emission line profile in the local rest frame is assumed to be a delta function. Emission from the first four image orders of the accretion disk are summed.

The injection spectrum and the absorption coefficient are binned linearly with energy. There are 1000 energy bins from $E = 0$ to $E = 2E_0$. The thermal width of the line is small with a width less than one energy bin. The synthetic spectrum is smoothed over sets of ten adjacent bins to suppress numerical noise.

I include a power-law continuum, and assume that its intensity scales with the line emissivity. This means that the equivalent width of the emission line is constant across the disk. It is set to be 0.05 of the rest line frequency, a value that is roughly what is seen in AGN (see Krolik 1999). The power law index of the continuum is fixed as $\gamma = 0.5$, where $\gamma$ is defined by

$$I \equiv CE^{-\gamma}, \tag{3.25}$$

in which $I$ is the continuum intensity as a function of energy, $E$, and $C$ is determined by the line equivalent width. The continuum emission is treated as part of the injection spectrum together with the emission line, which propagates through the absorbing material suspended much higher above.

I consider two cases: one with $a = 0$ corresponding to a Schwarzschild black hole; and another with $a = 0.998$, corresponding to a maximally spinning Kerr black hole. Spectra containing the continuum and the continuum plus line are plotted for various choices of the opacity of the absorbing clouds. Figure 3.14. shows, as expected, the observed continuum does not change when inclination or black hole spin is altered. The absorption causes a dip centred on the line rest frequency. This is due to the fact that the absorbing medium is spherically distributed and moving with relatively low bulk velocities. Its velocity anisotropy is not enough to cause visible changes with inclination.

Figure 3.15. shows the case where the emission line is added to the power-law continuum. With only moderate absorption, the line profile is already significantly altered. This is due to the absorption removing the photons in the continuum under the line, as well as the line itself. The absorption does not affect the diagnostic features of the line - the red and blue wings. However, the change in flux near the

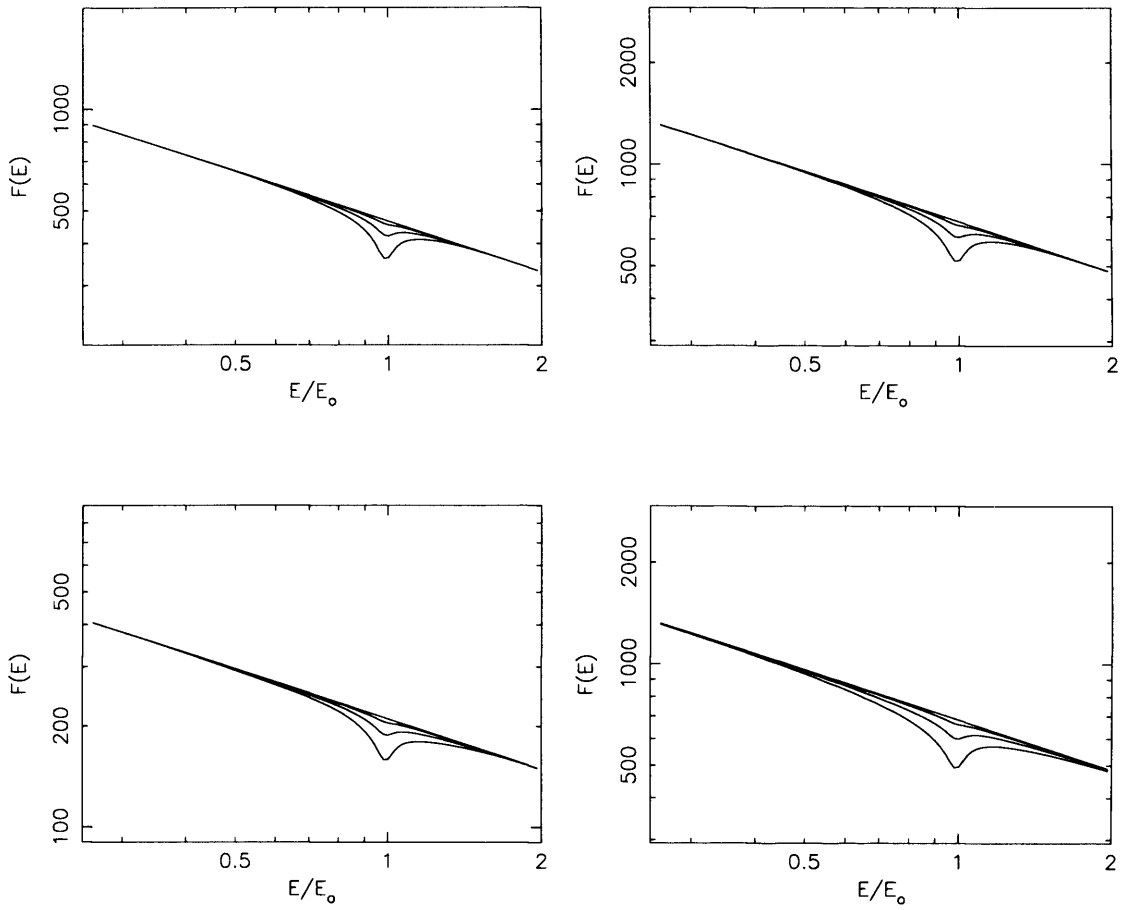


Figure 3.14: Absorbed continuum emission from accretion disks around Schwarzschild and Kerr black holes with $a = 0.998$ (left and right columns respectively), for viewing inclination $i = 45°$ and 85° (top and bottom panels respectively), and absorption parameter $\sigma_0 = 0$, 0.05, 0.2 and 0.5 (curves from top to bottom in each panel).

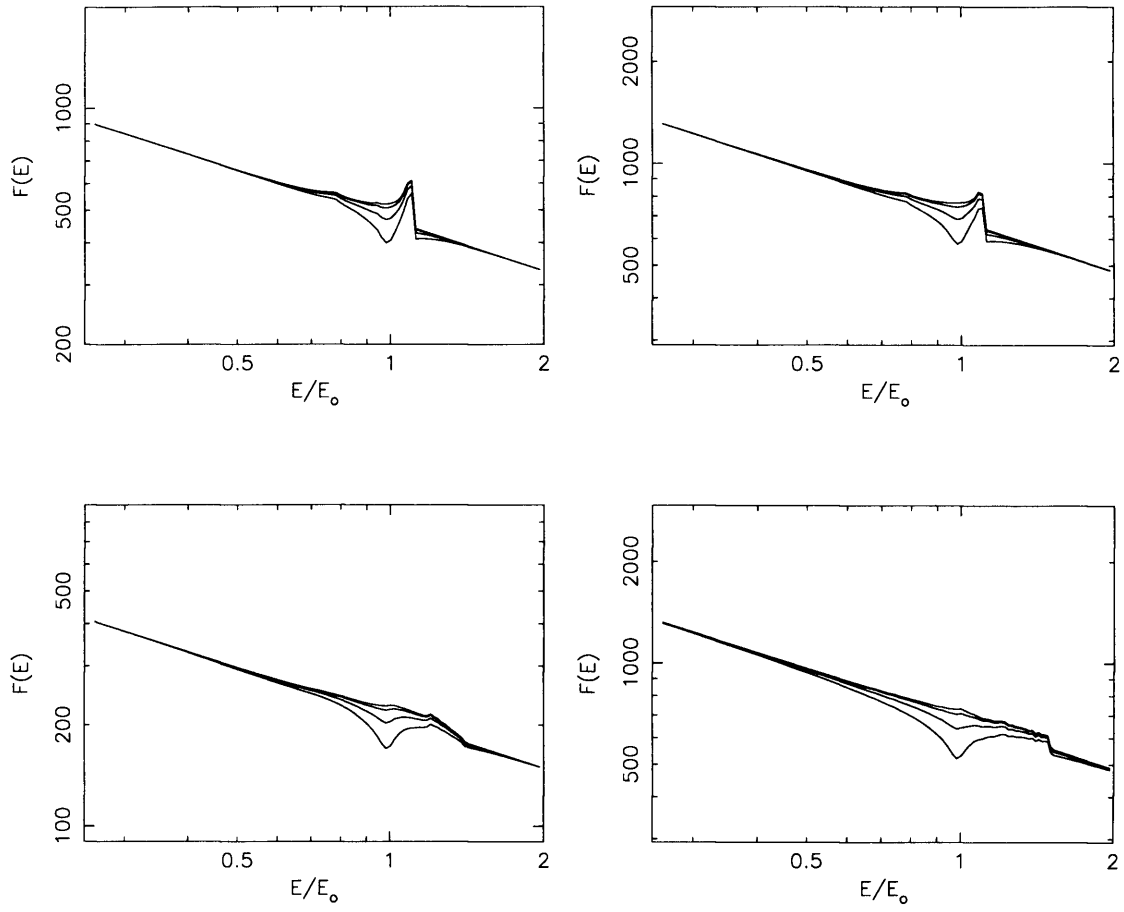


Figure 3.15: Line and continuum emission from accretion disks around Schwarzschild and Kerr black holes with $a = 0.998$ (left and right columns respectively), for viewing inclination $i = 45°$ and 85° (top and bottom panels respectively), and absorption parameter $\sigma_0 = 0$, 0.05, 0.2 and 0.5 (curves from top to bottom in each panel).

line rest frequency can emulate the removal of the non-direct images seen in §3.3.

## 3.5 Discussion

Resonant absorption/scattering of line emission from accreting black holes in the general relativistic framework had been investigated by Ruszkowski & Fabian (2000). In their study, a thin Keplerian disk was assumed and the absorbing medium is a spherical corona of constant density centred on the black hole. The corona is rotating, with local rates obtained by linear interpolation from the rotation rate of a planar Keplerian accretion disk and the rotation rate at the polar region caused by frame dragging due to the Kerr black hole. The Sobolov approximation was used in the resonant absorption calculations, and a Monte Carlo method determined the re-emission/scattering.

I have modelled spectral line profiles from accretion disks to demonstrate the use of a general formulation for transfer of radiation through relativistic media in arbitrary space-times. This model parametrises the disk to describe the emission and the space-density distribution of the absorbers. The model takes account of relativistic effects on the bulk dynamics and the microscopic kinematic properties of the absorbing medium.

My calculation is different from that of Ruszkowski & Fabian (2000) in the following ways. Firstly, the formulation is more general in that the emitters are not necessarily confined to the equatorial plane, i.e. they can be thin accretion disks or thick tori, which will be discussed in the next two chapters. Secondly, the absorbing medium is a collection of (cold) cloudlets with relativistic motions. The number density distribution of the clouds is parametrised by a power-law decreasing radially. The local bulk (rotational) velocity of the clouds is determined by general relativistic dynamics, and the velocity dispersion is calculated from the virial theorem. This is a more general setting in comparison with the spherical corona that Ruszkowski and Fabian (2000) considered. Thirdly, I do not assume the Sobolov approximation.

The resonant condition for the absorption coefficient is derived directly from the kinematics of the absorbing cloudlets. Fourthly, I ignore the contribution from re-emission to the line flux. However, I include emission from higher order disk images, in addition to the direct image.

The main difference between the two studies is the treatment of resonant absorption. Ruszkowski & Fabian use the Sobolov approximation which requires that the absorption takes place locally (see Rybicki & Lightman 1979). For the approximation to work, the line profile must be practically a delta function; otherwise, the assumption of quasi-local absorption breaks down. It also requires that the absorbing medium be a radial flow. In my calculation, the emission lines are broadened due to relativistic effects, and the motion of the medium is rotationally dominated. The locality of the absorption required by the Sobolov approximation is therefore not applicable. To overcome these difficulties, I need to employ a ray tracing method.

# Chapter 4

# Emission from Optically Thick Accretion Tori

If the accretion rate in a system is increased, eventually it will approach the Eddington limit. Once that happens, radiation pressure becomes so large that the thin disk solution used in the previous chapter breaks down. The accretion disk will puff up into a torus. In this chapter I investigate the emission from these accretion tori, and explore how a 3D geometry will affect the emission line profile.

The first requirement of this model is a description of the medium from which the radiation is emitted and transported through. In short this is the velocity and density structure of the material, combined with a description of a local emissivity and opacity. However, if the material is optically thick then all that is needed is the emissivity on an emitting surface at which the optical depth reaches infinity.

This chapter describes the derivation of the boundary of accretion tori around Kerr black holes. I will show that emission lines profiles from these accretion tori are different from those of geometrically thin accretion disks.

However, it must be noted that if the radiation pressure is too high, then photoionisation will cause the torus to be highly ionised. If this is the case, then emission lines from the torus will be weakened due electrons not existing in the required

orbitals. This effect is ignored here for simplicity.

## 4.1 The Boundary of an Accretion Torus

A method for deriving the surface of a torus around a Kerr black hole is based on the property that in the static case, the pressure is always balanced by the four-acceleration of the fluid. Thus I can trace an isobar by moving perpendicular to the four acceleration in the $r-\theta$ plane. Instead of defining the angular momentum as a function of position, a proscribed velocity field defines this model. From the velocity field, I can derive the four acceleration

$$\begin{aligned} a^{\nu} &= u^{\nu}{}_{;\beta}u^{\beta} , \\ &= u^{\nu}{}_{,\beta}u^{\beta} + \Gamma^{\nu}_{\alpha\beta}u^{\alpha}u^{\beta} \end{aligned} \tag{4.1}$$

and assuming again that the radial and poloidal components of the velocity field are negligible gives

$$a^{\nu} = \Gamma^{\nu}_{tt}u^{t}u^{t} + 2\Gamma^{\nu}_{t\phi}u^{t}u^{\phi} + \Gamma^{\nu}_{\phi\phi}u^{\phi}u^{\phi} . \tag{4.2}$$

Note that the partial derivative term drops out for an axisymmetric and stationary structure, as is the case here.

The accelerations in the $\hat{r}$ and $\hat{\theta}$ directions are therefore

$$-\frac{\Sigma}{\Delta}a^{r} = \frac{\Sigma - 2r^{2}}{\Sigma^{2}}\left(\dot{t} - a\sin\theta\dot{\phi}\right)^{2} + r\sin^{2}\theta\dot{\phi}^{2} , \tag{4.3}$$

$$-\Sigma a^{\theta} = \sin\theta\cos\theta\left[\frac{2r}{\Sigma^{2}}\left(a\dot{t} - (r^{2}+a^{2})\dot{\phi}\right)^{2} + \Delta\dot{\phi}^{2}\right] \tag{4.4}$$

in the Kerr metric. The surface of constant acceleration is given by

$$a_{\alpha}\frac{dx^{\alpha}_{\rm surf}}{d\lambda} = 0, \tag{4.5}$$

(here and hereafter $dx^{\alpha}_{\rm surf}/d\lambda \equiv dx^{\alpha}/d\lambda|_{x_{\rm surf}}$). The stationary condition implies $dt/d\lambda = 0$, and axisymmetry implies $d\phi/d\lambda = 0$. Without losing generality, let

$t = \phi = 0$ on the surface. Then, equation (4.5) becomes

$$\begin{aligned} 0 &= \frac{\Sigma a^r}{\Delta}\frac{dr_{\rm surf}}{d\lambda} + \Sigma a^\theta \frac{d\theta_{\rm surf}}{d\lambda} , \\ &= \beta_1 \frac{dr_{\rm surf}}{d\lambda} + \beta_2 \frac{d\theta_{\rm surf}}{d\lambda} , \end{aligned} \tag{4.6}$$

where

$$\begin{aligned} \beta_1 &= \frac{\Sigma - 2r^2}{\Sigma^2}\left(\frac{1}{\Omega} - a\sin\theta\right)^2 + r\sin^2\theta , \\ \beta_2 &= \sin\theta\cos\theta\left[\Delta + \frac{2r}{\Sigma^2}\left(\frac{a}{\Omega} - (r^2+a^2)\right)^2\right] , \end{aligned} \tag{4.7}$$

and $dr_{\rm surf}/d\lambda$ and $d\theta_{\rm surf}/d\lambda$ determine the intersection of the isobaric surfaces and the $(r,\theta)$ plane. Rescaling equation (4.6) by a factor of $\sqrt{\Delta/\Sigma}$ and making use of the invariance

$$-\left(\frac{d\tau}{d\lambda}\right)^2 = \frac{\Sigma}{\Delta}\dot{r}^2 + \Sigma\dot{\theta}^2 , \tag{4.8}$$

one can obtain

$$\begin{aligned} \frac{dr_{\rm surf}}{d\lambda'} &= \frac{\beta_1}{\sqrt{\beta_2^2 + \Delta\beta_1^2}} , \\ \frac{d\theta_{\rm surf}}{d\lambda'} &= \frac{-\beta_2}{\sqrt{\beta_2^2 + \Delta\beta_1^2}} . \end{aligned} \tag{4.9}$$

These two differential equations can be solved numerically and yield the isobaric surface as a parametric function of $\lambda'$.

To determine the geometry and structure of an accretion torus fully self-consistently requires a model of the energy dissipation mechanism, which is currently believed to be linked to the MHD turbulence caused by the magneto-rotational instability. See Balbus & Hawley (1991) for details. This mechanism is non-local due to the long-range interactions via magnetic tension forces. The detailed balance between the source of radiation inflating the disk into a torus and the energy loss due to the effective viscosity are difficult to express in terms of analytic functions. It seems that numerical MHD simulations are inevitably required to solve this correctly. The complexity of such numerical calculations is beyond the scope of this thesis, and deserve a separate study.

## 4.2 Parametric Torus Model

I consider a simple parametric model, with an angular velocity profile given by

$$\Omega = \frac{1}{(r\sin\theta)^{3/2}+a}\left(\frac{r_{\rm K}}{r\sin\theta}\right)^n . \tag{4.10}$$

The quantity $r_{\rm K}$ is the radius (on the equatorial plane) at which the material moves with a Keplerian velocity. The index $n$ adjusts the force term, such as a pressure gradient, to keep the disk particles in their orbits, and it determines the thickness of the torus. The torus is supported by radiation pressure. However, this support breaks down near the black hole. The inner edge the torus is determined by the intersection of the isobaric surface with either one of two surfaces. These two surfaces provide constraints, inside which the pressure-supported solution does not hold. The first is a surface defined by the orbits of marginal stability. For $\Omega(r,\theta)$, it is given by

$$\begin{aligned} 0 \;=\; & 2a\sin^4\theta\left[\frac{r^2}{\Sigma}-\left(r^2+a^2+\frac{a^2 r\sin^2\theta}{\Sigma}\right)\frac{\Sigma-2r^2}{\Sigma^2}\right]\Omega^3 \\ & +\sin^2\theta\Bigg[\left(\frac{6r(r^2+a^2)}{\Sigma}+3\Delta-\Sigma\right)\frac{\Sigma-2r^2}{\Sigma^2} \\ & \quad +r\left(1-\frac{2r}{\Sigma}\right)\Bigg]\Omega^2-\frac{6ar\sin^2\theta}{\Sigma}\left(\frac{\Sigma-2r^2}{\Sigma^2}\right)\Omega \\ & +\Delta\sin^2\theta\,\Omega\frac{\partial\Omega}{\partial r}-\left(1-\frac{2r}{\Sigma}\right)\frac{\Sigma-2r^2}{\Sigma^2} . \end{aligned} \tag{4.11}$$

The second is the limiting surface where the linear velocity approaches the speed of light. It is given by

$$\begin{aligned} 0 \;=\; & \Sigma-2r+4ar\Omega\sin^2\theta \\ & -\left((r^2+a^2)\Sigma+2a^2 r\sin^2\theta\right)\Omega^2\sin^2\theta . \end{aligned} \tag{4.12}$$

Usually the former is larger than the latter (they are equal in degenerate cases). The outermost of these two surfaces determines the inner boundary and hence the critical surface of the torus.

In this model the boundary surface of the torus is determined by two parameters, $n$, which specifies the index of the angular-velocity power law, and $r_{\mathrm{K}}$, which determines its centre. Figure 4.1. shows the critical density surfaces of two tori. The first torus is around a Schwarzschild black hole and the second torus is around a maximally rotating black hole. The tori are constructed such that their specific angular momentum has a profile similar to those of the simulated accretion disks in Fig. 3. of Hawley & Balbus (2002), corresponding to choosing $n = 0.21$.

Model tori can be constructed using various different methods. An example is the study of dynamical stability of tori around a Schwarzschild black hole carried out by Kojima (1986): the model parametrises angular momentum instead of angular velocity. The aspect ratios of the torus surfaces obtained by Kojima (1986) and those shown in Fig. 4.1. are similar. Another example are the self-gravitating tori of Usui *et al.* (1998), which again uses the constant angular momentum formulation. They obtain results similar to those found in this chapter. However, their tori are more applicable to gamma ray bursts produced by neutron star - neutron star collisions than the inner accretion disk in AGN, as the self gravity of the torus alters the metric.

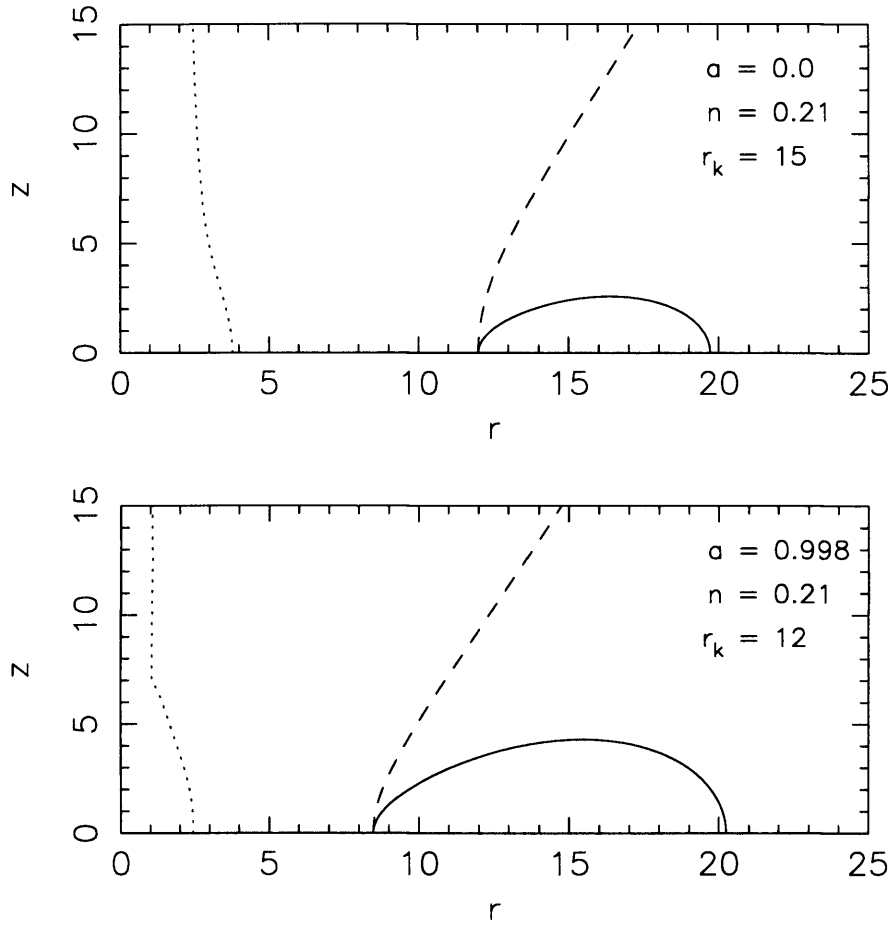


Figure 4.1: The critical emitting surface of the torus (solid line), the surface defined by the orbits of marginal stability (dashed line) and the limiting surface where the linear velocity derived from equation (4.10) approaches the speed of light (dotted line) for a Schwarzschild black hole (top panel) and a Kerr black hole with $a = 0.998$ (bottom panel). The profile index $n = 0.21$ in both cases [see Equation (4.10)], which gives the tori an angular momentum profile similar to those obtained in the accretion disk simulation of Hawley & Balbus (2002). The Kepler radius $r_{\rm K}$ is $15R_{\rm G}$ for the Schwarzschild black hole and is $12R_{\rm G}$ for the Kerr black hole.

## 4.3 Ray Tracing with a Curved Boundary

I now investigate the emission from an accretion torus. I consider a model in which the inner radius of the torus is determined by the marginally stable orbits of the particles. These marginally stable orbits, which depend on $\Omega$ and $d\Omega/dr$, form a surface in a three-dimensional space. The marginally stable orbit for particles in Keplerian motion in the equatorial plane is 6 $R_{\rm G}$ around a Schwarzschild black hole, and is 1.23 $R_{\rm G}$ around a Kerr black hole with $a = 0.998$. In equation (4.10), Keplerian motion corresponds to the case with the index $n = 0$.

In the torus model presented here, $n$ is not zero. As a consequence, the location of the marginally stable orbit of particles in the tori and conventional Keplerian disks differ. (See Fig. 4.1. in §4.2). The boundary of the torus is determined by a surface-finding algorithm. I first integrate the surface equations (4.9) are integrated, and tabulate the resulting points $(r, \theta)$ along the path of the integration. I then use spline interpolation on $(r, \theta)$ to construct the torus surface.,

In the ray-tracing algorithm, the integrator determines the intersection of the light trajectory and the torus surface. As the photon trajectory calculations may take large spatial steps, there is a possibility that the torus is not 'detected'. I use the following procedure to prevent this numerical mishap. I take note of the region where the photon is located during the trajectory calculation: either inside or outside the torus and either above or below the equatorial plane. Whenever the photon leaves one of the four regions, and enters another region, a boundary-searching algorithm is used to find the exact location where the transit occurs. If the trajectory hits the equatorial plane outside the torus, the integration will continue. If the trajectory hits the torus, the integration is terminated.

By taking smaller steps required by the boundary-finding algorithm, the integrator avoids missing the torus entirely. This algorithm is applicable even for more complicated surfaces and it works well in most circumstances. The integrator only misses intersections when the trajectory is almost tangential to the surface, or in

the region close to the equatorial plane due to peculiarities in the error analysis in the Runge-Kutta integrator. By adding a fake boundary there, and thus decreasing the step size, missed intersections can be prevented.

## 4.4 Line Emission from Optically Thick Tori

The emission model used here is similar to that of the geometrically thin accretion disk models for the accretion tori. It parametrises the line emissivity on the surface in terms of a power-law of the spherical radius, $r$. The same power-law index was chosen as in the disk models in the previous chapters. i.e.

$$\mathcal{I} \propto r^{-2}. \tag{4.13}$$

Figure 4.2. shows images of the model torus around a Kerr black hole at various viewing inclinations. The colours correspond to the energy shift like those in the accretion disk images in the previous chapter. The first four image orders are rendered. The inclusion of high order images is mandatory due to the 'mixing' caused by the extension out of the equatorial plane (Viergutz 1993). The left-right asymmetry is caused by inertial-frame dragging. The multiple images are consequences of gravitational lensing. At small inclination angles, say 30°, only the surface above the equatorial plane of the torus is seen in the direct image. At viewing inclination angles close to 90°, the surface below the equatorial plane is severely lensed and also becomes visible.

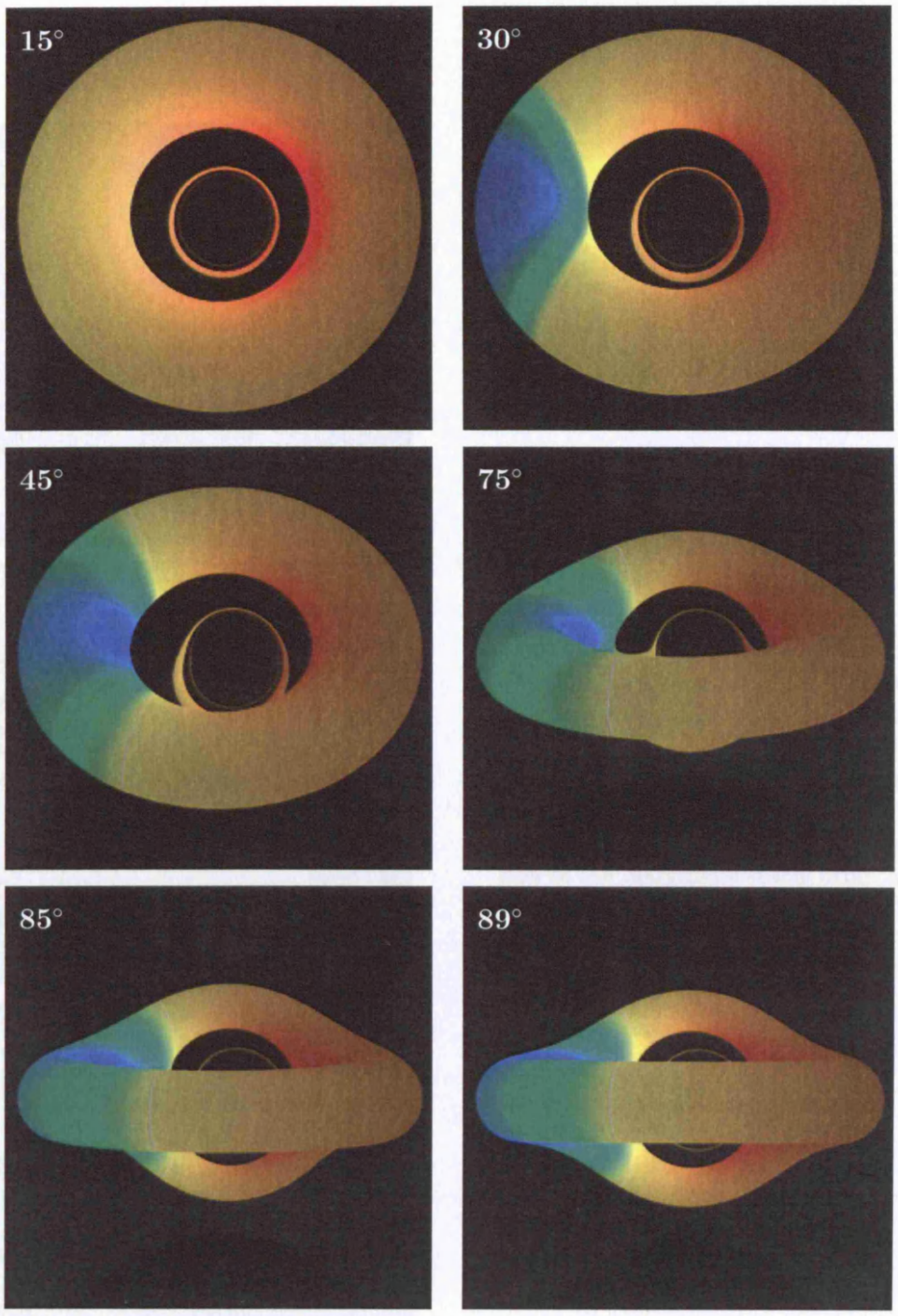


Figure 4.2: False-colour images of accretion tori around Kerr black holes viewed at inclination angles of 15°, 30°, 45°, 75°, 85° and 89°. The spin of the black hole $a = 0.998$. The torus is constructed using the velocity law in equation (4.10), with $n = 0.21$. The inner and outer radii are determined by the critical surface as described in the same section. High-order images are shown. The colour notation is the same as in Fig. 3.2.

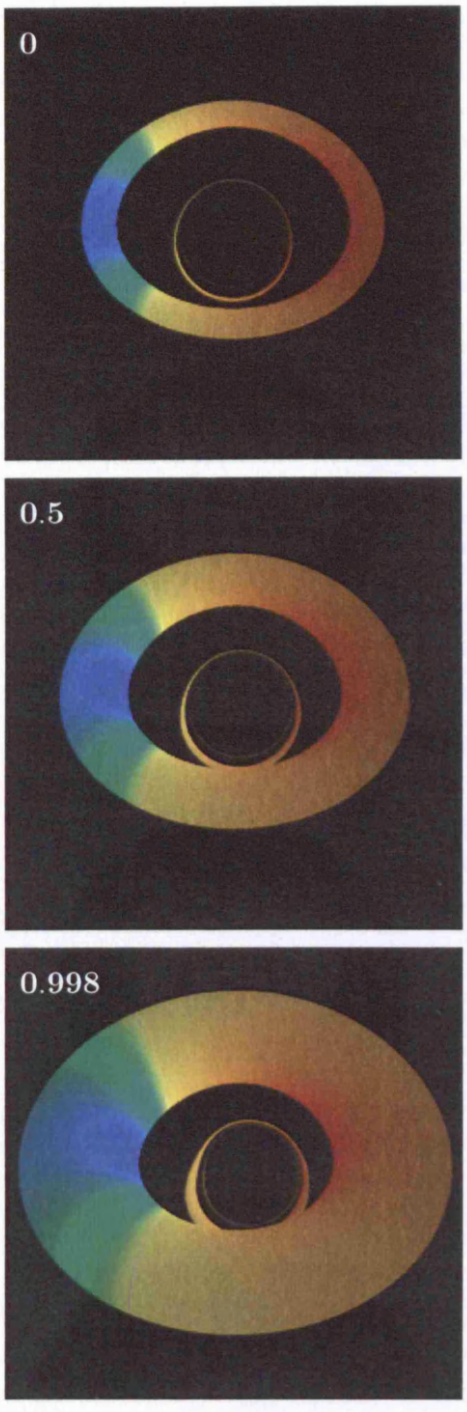


Figure 4.3: False-colour images of accretion tori around black holes viewed at an inclination angle of 45°. The spin of the black hole $a = 0, 0.5$, and 0.998 (top to bottom). The tori are constructed using the velocity law in equation (4.10), with $n = 0.21$. Changing the black hole spin alters the location of the marginally stable orbit, and here the inner edge of the torus. The colour notation is the same as in Fig. 3.2.

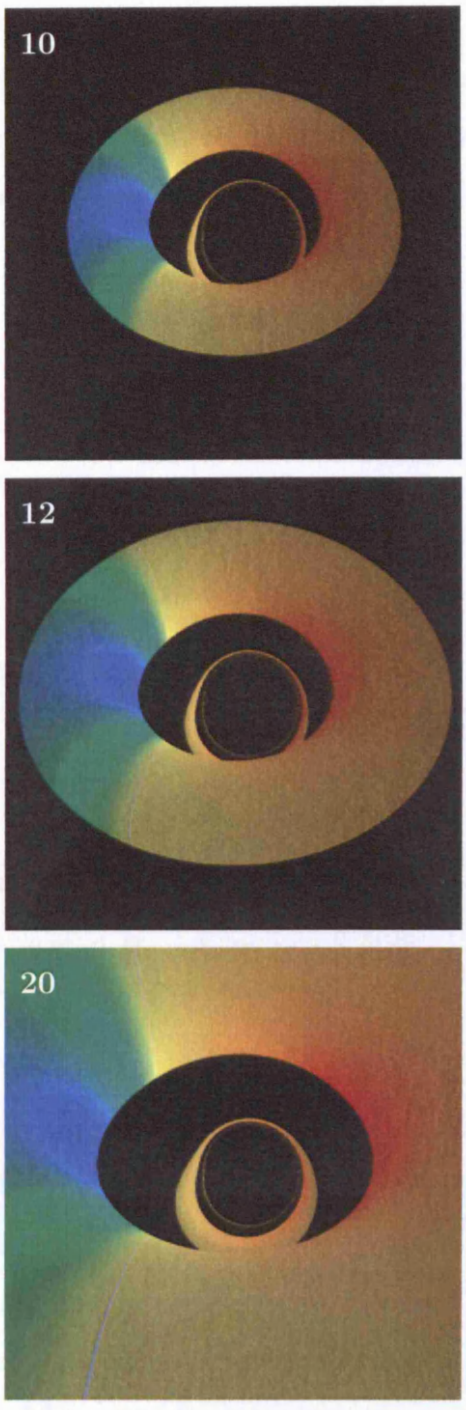


Figure 4.4: False-colour images of accretion tori around Kerr black holes viewed at an inclination angle of 45°. The spin of the black hole $a = 0.998$. The tori are constructed using the velocity law in equation (4.10), with $n = 0.21$. The ring of maximum density and Keplerian motion at radius $r_K$ is set to be $10, 12$, and $20R_G$ (top to bottom).

Figure 4.3. illustrates how the black hole spin parameter affects the appearance of the accretion torus. The asymmetry increases with $a$. The distortion is more severe in the higher order images. Fig. 4.4. shows how the torus size varies with $r_{\rm K}$. While $r_{\rm K}$ adjusts the extent of the torus in the equatorial plane, the angular velocity power-law index determines the vertical aspect, i.e. one can change the shape of the torus from 'fat' to 'thin' by altering the value of $n$.

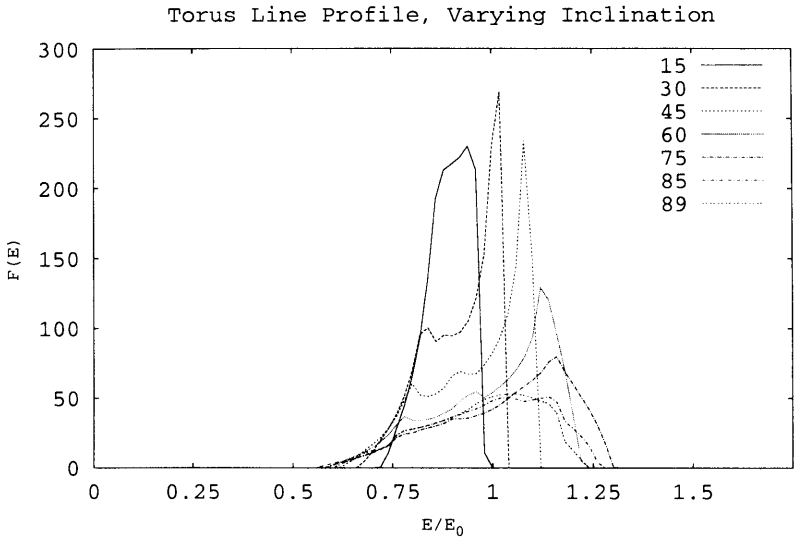


Figure 4.5: Profiles of emission lines from accretion tori around Kerr black holes with $a = 0.998$ with viewing inclination angles from 15° to 85°. The parameters of the torus are $n = 0.21$ and $r_{\rm K} = 12R_{\rm G}$ in the velocity profile equation (4.10). The emissivity power-law index is $-2$. The fluxes are in arbitrary units.

Figures 4.2., 4.3. and 4.4. also show the energy shift of the photons emitted from the torus surface [determined by equation (2.39)], as viewed by a distant observer. At large inclination angles the inner surface of the near side of the torus is not visible, and the inner surface of the far side is obscured by the near side of the torus. Thus, the emission regions with the largest energy shifts are hidden. This is very different to the situation of a planar accretion disk – regardless of the viewing inclination and the visual distortion, the emission from the innermost part of a flat disk is always visible.

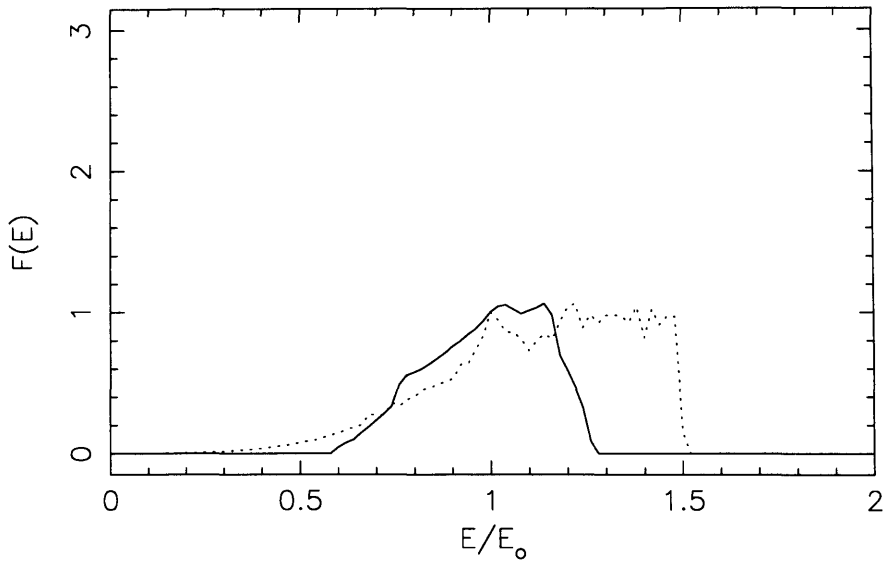


Figure 4.6: A comparison of the profiles of lines from an opaque accretion disk (dotted line) and an opaque accretion torus (solid line) around a Kerr black hole with $a = 0.998$. The disk and the torus are viewed at an inclination angle of 85°. The parameters of the torus are the same as those in Fig. 4.5. The disk has an outer radius of $20R_G$, an inner radius of $1.23R_G$, and a Keplerian velocity profile. These line profiles have been normalised so that $F(E) = 1$ when $E = E_0$, the rest energy of the line.

By integrating the contribution of emission over a torus image we can obtain a spectrum. Figure 4.5. shows the line profiles obtained for the images in Fig. 4.2. The line profile of a torus viewed at 45° is similar to that of the planar accretion disk. It has a sharp blue peak and smaller red peak. It also has an extended red wing. This is due to the fact that the projections of a torus and a disk on the sky plane are very similar at low inclination angles.

However, geometric effects are very important for large viewing inclination angles. At large viewing inclination angles, the inner surfaces of a torus can be obscured. The hidden part corresponds to the region where the maximally redshifted line-flux is emitted (due to large transverse red shift and gravitational red shift). Hiding this region makes the red wing less prominent. In contrast, the outer surface of the torus is visible from all inclinations and the corresponding emission has small

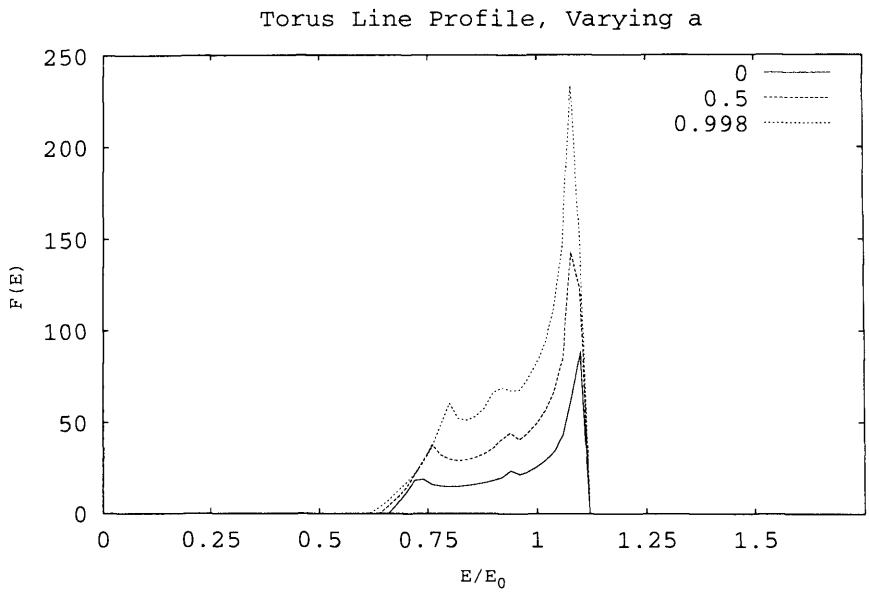


Figure 4.7: Profiles of emission lines from an opaque accretion torus around Kerr black holes with $a = 0, 0.5$, and $a = 0.998$ at viewing inclination angle of 45°. The parameters of the torus are $n = 0.21$ and $r_{\rm K} = 12R_{\rm G}$. The emissivity power-law index is $-2$.

energy shifts. As a result, the line profile tends to be singly peaked, with the maximum at the unshifted line frequency. The resulting profile is very different from that of the flat disk (see Fig. 4.6.). By varying the viewing geometry of the torus, we can obtain emission lines that look like like "'humps" centred on the line rest energy, or asymmetric double-horn profiles like those from relativistic accretion disks.

My calculations also show spectra from tori can only weakly constrain the black hole spin. Figure 4.7. shows that varying $a$ does not affect the overall shape of an emission line. The only significant change is the absolute normalisation of the flux due to the fact that the inner edge of the torus depends on the black hole spin via the location of the marginally stable orbit. Faster spinning black holes have marginal stable orbits closer to the event horizon, resulting in bigger tori if the point of Keplerian motion is unmodified.

# Chapter 5

# Emission from Semi-Transparent Accretion Tori

In general, an accretion torus would not have a well defined boundary like those modelled in the previous chapter. Even if the torus is optically thick, we would expect that it has an atmosphere characterised by a certain scale height. Moreover, the torus could be transparent or semi-transparent. In this case the density and velocity structure in the torus would play an important role in determining the properties of the radiation.

## 5.1 Polish Doughnut Model

There are various models for hydrostatic accretion tori in the Kerr metric. Abramowicz (2004) reviewed super-Eddington black hole accretion, with particular attention paid to the 'Polish doughnut' model, a name which was coined by M. Rees. An assumption in the model is that the self-gravity of the torus is negligible, which is the case for accretion flow around an AGN. Another assumption is a barotropic equation of state, which ensures the isobaric (equal pressure) and isopycnic (equal density) surfaces coincide.

Following Abramowicz *et al.* (1978), and Kozlowski *et al.* (1978), I now construct

a model of an accretion torus. The torus is assumed to be made of a perfect fluid. It rotates in the $\phi$ direction, and there is the flow in the $r$ and $\theta$ directions is negligible. The motion of the torus is aligned with the motion of the black hole. The flow is assumed to be stationary (no time dependence) and axisymmetric.

The energy-momentum tensor for a perfect fluid is given by,

$$T^{\alpha\beta} = (\rho + P + \epsilon)u^{\alpha}u^{\beta} + Pg^{\alpha\beta}, \tag{5.1}$$

where $P$ is the pressure, $\rho$ is the density, and $\epsilon$ is the internal energy of the fluid. By taking the covariant derivative, we obtain

$$T^{\alpha\beta}{}_{;\beta} = 0 = (\rho + P + \epsilon)_{,\beta}u^{\alpha}u^{\beta} + (\rho + P + \epsilon)(u^{\alpha}{}_{;\beta}u^{\beta} + u^{\alpha}u^{\beta}{}_{;\beta}) + P_{,\beta}g^{\alpha\beta}. \tag{5.2}$$

Projecting perpendicularly to the velocity using the projection tensor

$$P^{\alpha\beta} = u^{\alpha}u^{\beta} + g^{\alpha\beta}, \tag{5.3}$$

yields the momentum equations

$$(\rho + P + \epsilon)u^{\alpha}{}_{;\beta}u^{\beta} + P_{,\beta}g^{\alpha\beta} = 0. \tag{5.4}$$

If the fluid is stationary and axisymmetric, the following identity holds:

$$\begin{aligned} u_{\alpha;\beta}u^{\beta} &= u_{\alpha,\beta}u^{\beta} - \Gamma^{\delta}_{\alpha\beta}u_{\delta}u^{\beta} \\ &= -\Gamma^{\delta}_{\alpha\beta}u_{\delta}u^{\beta} \\ &= -u_{\delta}u^{\beta}\left[\frac{1}{2}g^{\delta\epsilon}\left(g_{\epsilon\beta,\alpha} + g_{\epsilon\alpha,\beta} - g_{\beta\alpha,\epsilon}\right)\right] \\ &= -\frac{1}{2}u^{\epsilon}u^{\beta}g_{\epsilon\beta,\alpha}\ . \end{aligned} \tag{5.5}$$

Since $u^{\alpha}u_{\alpha} = -1$,

$$\begin{aligned} 0 &= \left(u^{\alpha}u_{\alpha}\right)_{,\delta} \\ &= \left(u^{\alpha}u^{\beta}g_{\alpha\beta}\right)_{,\delta} \\ &= 2u^{\alpha}_{,\delta}u_{\alpha} + u^{\alpha}u^{\beta}g_{\alpha\beta,\delta}\ , \end{aligned} \tag{5.6}$$

$$\tag{5.7}$$

implying

$$-\frac{1}{2}u^\alpha u^\beta g_{\alpha\beta,\delta} = u^\alpha_{,\delta} u_\alpha \ . \tag{5.8}$$

As $u^r = u^\theta = 0$, it follows that

$$u_{\alpha;\beta}u^\beta = u^t \partial_\alpha u_t + u^\phi \partial_\alpha u_\phi \ , \tag{5.9}$$

where $\partial_\alpha$ is the gradient in the $x^\alpha$ direction.

The angular momentum per unit energy and angular velocity are defined as

$$l \equiv -\frac{u_\phi}{u_t} \ , \tag{5.10}$$

$$\Omega \equiv \frac{u^\phi}{u^t} \ . \tag{5.11}$$

With the identity $u^\alpha u_\alpha = -1$, we can show

$$\frac{-1}{u^t u_t} = \frac{1}{u^t u_t}\left(u^t u_t + u^\phi u_\phi\right) = 1 - l\Omega \ , \tag{5.12}$$

and hence

$$u^\phi u_t = -\frac{\Omega}{(1 - l\Omega)}. \tag{5.13}$$

The gradient of $l$ is

$$\partial_\alpha l = \frac{u_\phi}{u_t^2}\partial_\alpha u_t - \frac{1}{u_t}\partial_\alpha u_\phi. \tag{5.14}$$

Multiplying both sides by $u^\phi u_t$ and using equation (5.13) gives

$$\begin{aligned} u^\phi u_t \partial_\alpha l &= \frac{u_\phi u^\phi}{u_t}\partial_\alpha u_t - u^\phi \partial_\alpha u_\phi \ , \\ \frac{\Omega\ \partial_\alpha l}{(1 - l\Omega)} &= \frac{1}{u_t}\partial_\alpha u_t + u^t \partial_\alpha u_t + u^\phi \partial_\alpha u_\phi \ . \end{aligned} \tag{5.15}$$

Substituting the expression in equation (5.9), we obtain

$$u_{\alpha;\beta}u^\beta = \frac{\Omega\ \partial_\alpha l}{(1 - l\Omega)} - \frac{1}{u_t}\partial_\alpha u_t \ . \tag{5.16}$$

Now we can rewrite equation (5.4) as

$$u_{\alpha;\beta}u^\beta = \frac{-P_{,\alpha}}{\rho + P + \epsilon} \ . \tag{5.17}$$

It follows that,

$$-\partial_\alpha \ln(u_t) + \frac{\Omega\, \partial_\alpha l}{1 - l\Omega} = \frac{-\partial_\alpha P}{\rho + P + \epsilon} \,. \tag{5.18}$$

This equation is equivalent to that given in Abramowicz, Jarosyznski & Sikora (1978) for the accretion torus.

An equation of state is required to close the system of hydrodynamic equations, and a barotropic gas is assumed. The set of equations can then be solved via quadratures when the angular momentum of the fluid is given as a function of position. In general, the solution needs to be calculated numerically due to the complexity of the Kerr metric. However, in the special case when $l$ =constant, which corresponds to a marginally stable disk, then an analytic solution is possible:

$$\int_0^P \frac{dP}{\rho + P + \epsilon} = \ln(u_t) - \ln(u_t)_{\rm in} \tag{5.19}$$

(with the subscript 'in' denoting variables evaluated at the inner edge of the torus).

## 5.2 Density Profile

The transparency of the radiation implies that the local emissivity and opacity inside the accretion torus must be specified explicitly. In other words, we need to determine the velocity, temperature and the density structure before proceeding to the radiative transfer calculation.

I now construct a model for the structure of the torus. The total pressure in the torus is the sum of the gas pressure and the radiation pressure.

$$P = P_{\rm gas} + P_{\rm rad} \,, \tag{5.20}$$

which are given by

$$P_{\rm gas} = \frac{\rho k_{\rm B} T}{\mu m_{\rm H}} = \beta P, \tag{5.21}$$

$$P_{\rm rad} = \frac{4\sigma}{3} T^4 = (1 - \beta) P, \tag{5.22}$$

where $\mu$ is the mean molecular weight, and $\beta$ describes the ratio of gas pressure to total pressure, and

$$\sigma = \frac{\pi^2 k_{\rm B}^4}{60\hbar^3} \tag{5.23}$$

is the black-body emittance constant. Note that the black-body radiation profile has been assumed in the calculation of the radiation pressure. In optically thin tori, radiative thermal equillibrium will not apply, so this assumption is suspect. In addition, I assume here that $\beta$ is constant throughout the torus. This is very likely not to be the case. However, these assumptions are required to obtain an equation of state. To improve this analysis a much more complicated model of the interaction between matter and radiation is required. However, that would not yield the simple polytropic equation of state as is wanted here for an initial analysis of accretion tori.

Eliminating $k_{\rm B}T$ from the above equations yields

$$P = \hbar\rho^{4/3}\left[\frac{45(1-\beta)}{\pi^2(\mu m_{\rm H}\beta)^4}\right]^{1/3} . \tag{5.24}$$

For a polytropic equation of state

$$P = \kappa\rho^{\Gamma}, \tag{5.25}$$

and the internal energy is related to the pressure by

$$\epsilon = P/(\Gamma - 1). \tag{5.26}$$

Comparing equations (5.24) and (5.25), I obtain with $\Gamma = 4/3$, and

$$\kappa = \hbar\left[\frac{45(1-\beta)}{\pi^2(\mu m_{\rm H}\beta)^4}\right]^{1/3} \tag{5.27}$$

(See Bowers & Deeming 1984).

Recall the momentum equation for an ideal fluid, equation (5.4). Combining it with the polytropic equation of state yields

$$\left(\rho + \frac{\Gamma}{\Gamma - 1}P\right)a^{\alpha} = -P_{,\beta}g^{\alpha\beta} . \tag{5.28}$$

By differentiating (5.25) we obtain

$$\frac{\partial P}{\partial x^\alpha} = \kappa\Gamma\rho^{\Gamma-1}\frac{\partial \rho}{\partial x^\alpha} \ . \tag{5.29}$$

Hence the density structure of the torus is given by

$$\frac{\partial \rho}{\partial x^\alpha} = -a_\alpha\left(\frac{\rho^{2-\Gamma}}{\kappa\Gamma} + \frac{\rho}{\Gamma-1}\right) \ . \tag{5.30}$$

This equation has two non-trivial components, in the $\hat{r}$ and $\hat{\theta}$ directions. The equations for the other two components are identically zero because of the stationarity and axisymmetry conditions.

The contravariant acceleration terms are given by

$$\begin{aligned} -a^r g_{rr} &= r\dot{\phi}^2 - \left[\frac{\dot{t}}{r}(1-a\Omega)\right]^2 , \\ -a^\theta g_{\theta\theta} &= \sin\theta\cos\theta\left[\frac{2r}{\Sigma}\left(a\dot{t} - (r^2+a^2)\dot{\phi}\right)^2 + \Delta\dot{\phi}^2\right] . \end{aligned} \tag{5.31}$$

We may solve for $\rho$ by evaluating the line integral from $r = r_{\rm K}$, $\rho = \rho_{\rm c}$ at the torus centre, to the required $(r,\theta)$ location. As the pressure in the accretion torus is dominated by the radiation, we may consider the limit $\beta \to 0$. Inserting the above expressions for $\kappa$ and $\Gamma$ into (5.30) yields

$$\begin{aligned} \frac{1}{\rho}\frac{\partial \rho}{\partial x^\alpha} &= 3g_{\alpha\beta}a^\beta\left(\frac{1}{4\kappa(\rho)^{1/3}} + 1\right) , \\ \frac{\partial \ln\rho}{\partial x^\alpha} &= 3g_{\alpha\beta}a^\beta\left(\frac{(\mu m_{\rm H}\beta)^{4/3}}{4\hbar\left[45\rho/\pi^2\right]^{1/3}} + 1\right) . \end{aligned} \tag{5.32}$$

Here, the same velocity law is used as in the previous chapter to determine the covariant acceleration, and hence the density. When the density is determined, the pressure and temperature can be calculated from

$$\begin{aligned} P &= \hbar\left[\frac{45\rho^4}{\pi^2(\mu m_{\rm H}\beta)^4}\right]^{1/3} , \\ k_{\rm B}T &= \hbar\left[\frac{45\rho}{\pi^2\mu m_{\rm H}\beta}\right]^{1/3} . \end{aligned} \tag{5.33}$$

## 5.3 Emission Lines

In this section I present calculations of line emission from tori which are optically thin to continuum yet semi-opaque to line emission. Consider an accretion torus enveloped by a hot transparent corona. The corona provides the hard photons which cause fluorescent line emission. We assume that the corona itself does not contribute to the line emission significantly. The local emissivity of the line in the torus is proportional to the density and is independent the location of the emitting volume. This emissivity model distinct from that of the emission from geometrically thin disks in chapter 3, where the intensity depends on the radial distance of the surface area element from the central object.

As illustrations, we consider two lines in our calculations here: the iron K$\alpha$ and K$\beta$ at 6.70186 keV and 6.97325 keV. The emissivity of the K$\beta$ line is set to be 14% of the K$\alpha$ line (see Hölzer *et al.* 1997). Absorption is ignored. This is equivalent to assuming that the tori optically thin to the line emission.

The rendered images from the ray-tracing calculation contain $250 \times 250$ pixels, portraying tori around Kerr and Schwarzschild black holes. The modifying power-law index of the angular velocity is set as $n = 0.21$ so that the tori approximate those seen in Hawley & Balbus (2002). We also set the point of Keplerian rotation $r_{\rm K} = 12r_{\rm G}$, and the gas pressure fraction at $\beta = 5 \times 10^{-5}$ of the total pressure. The maximum number density at the densest point scales out of the problem, since the absorption is ignored here. The black hole gravitational radius is fixed to be $R_{\rm G} = 10^{13}$ cm.

Images of the torus are rendered at viewing inclinations from 15° to 85°. Figure 5.1. shows the surface brightness images of the line emission from tori around extreme Kerr black holes with $a = 0.998$. Figure 5.2. shows surface brightness images of line emission from tori around black holes with different spin parameters.

As shown, the torus images are distorted. The distortion depends strongly upon inclination. The far side of the torus ring is gravitationally lensed to appear much

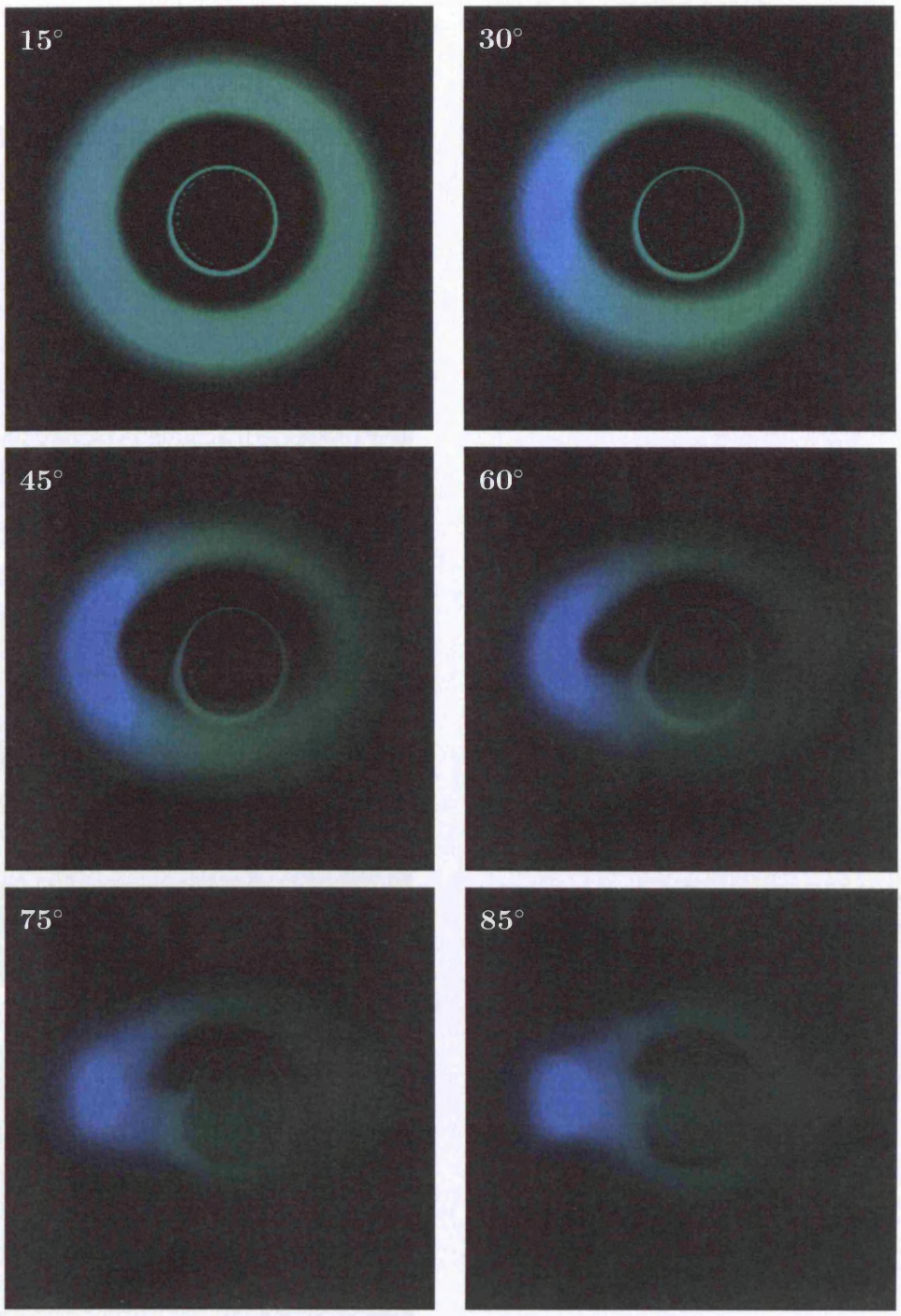


Figure 5.1: Surface brightness images of an optically thin accretion tori around black holes with $a = 0.998$ viewed at inclination angles of 15°, 30°, 45°, 60°, 75° and 85°. The emission is purely from the Iron K$\alpha$ and K$\beta$ lines. The brightness is normalised such that the maximum brightness is the same in for all the images. The Doppler 'headlight' effect makes the edge-on tori have a much higher contrast ratio than those viewed at low inclinations. Note that due to dynamic range issues, the images have been normalized such that the brightest pixel in each image is the same intensity.

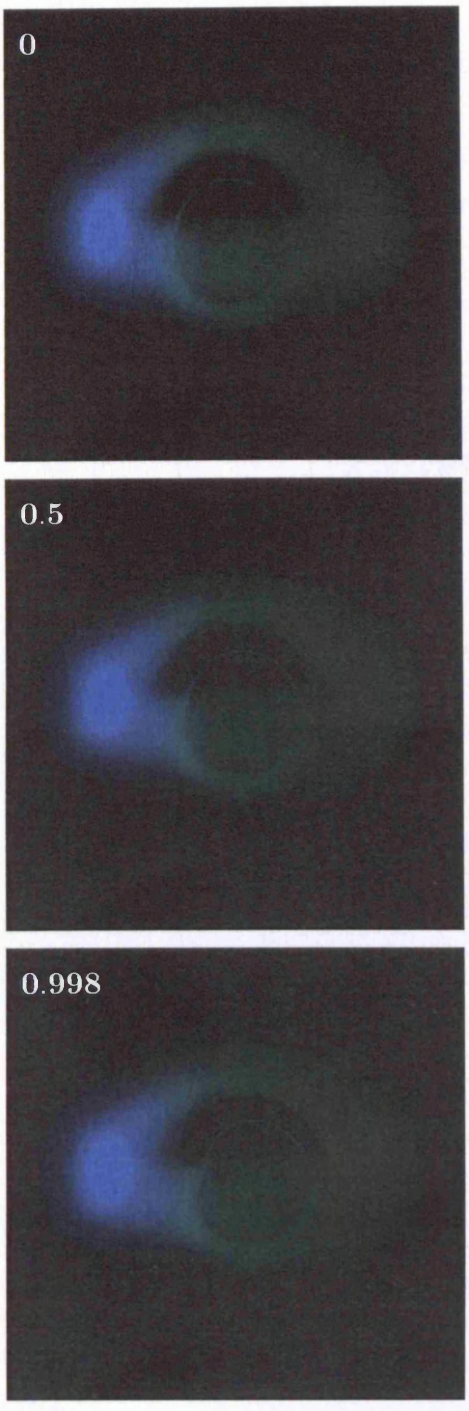


Figure 5.2: Surface brightness images of optically thin accretion tori around Kerr black holes viewed at an inclination of 75°. The spin of the black hole $a = 0, 0.5$, and 0.998 (from top to bottom). The emission is purely from the Iron K$\alpha$ and K$\beta$ lines. Note that due to dynamic range issues, the images have been normalized such that the brightest pixel in each image is the same intensity.

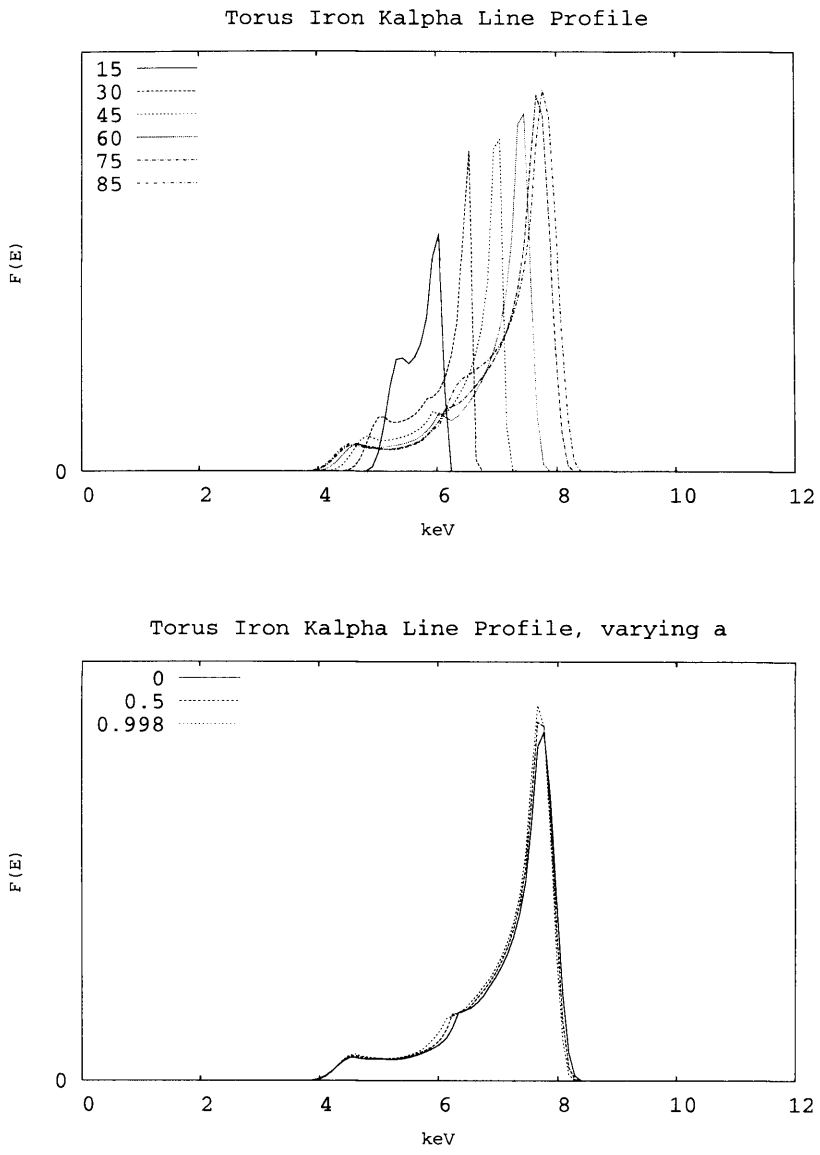


Figure 5.3: Profiles of the iron K$\alpha$ line from optically thin accretion tori. The line emissivity is proportional to the density. The top panel shows line profiles for tori with viewing inclination angles ranging from 15° to 85°. The bottom panel shows line profiles for tori around black holes with $a = 0, 0.5$ and 0.998.

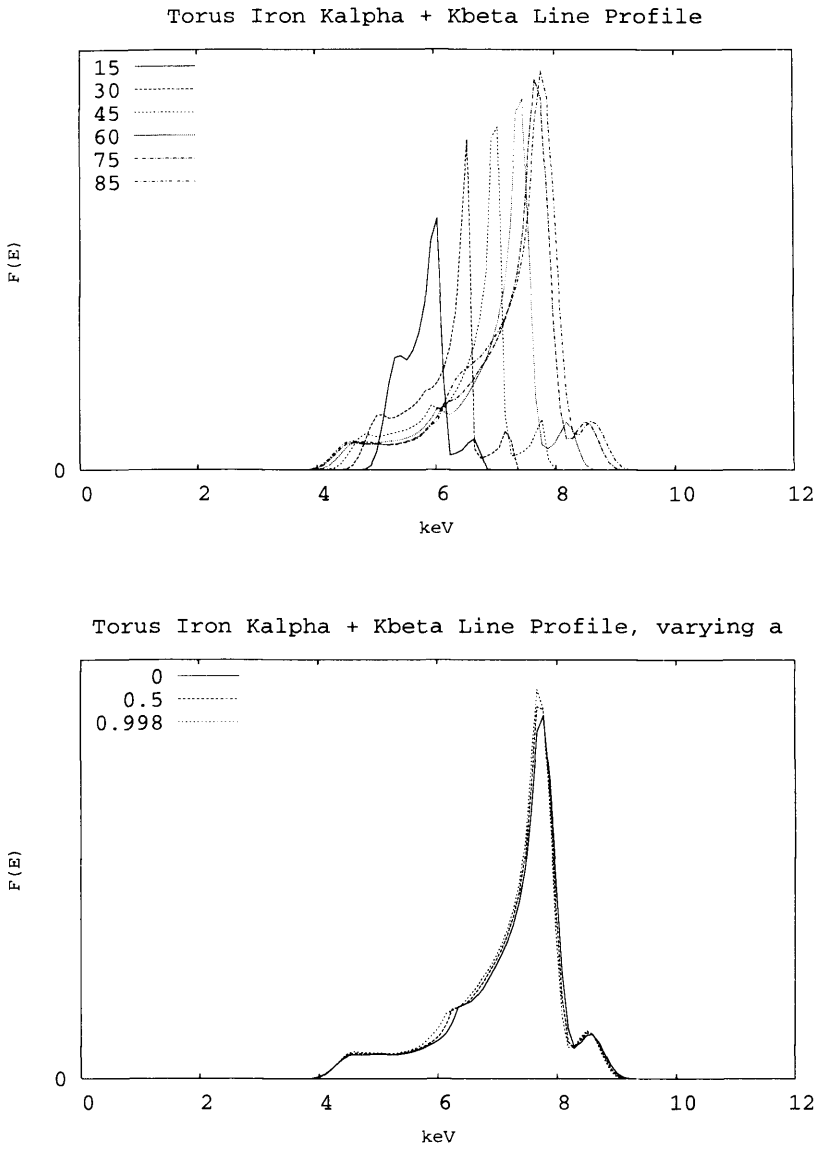


Figure 5.4: Profiles of combined Iron K$\alpha$ and K$\beta$ lines from an optically thin accretion torus. The line emissivity is proportional to the density, and the K$\beta$ line emissivity is 14% of the K$\alpha$ emission. The top panel shows profiles for tori with viewing inclination angles ranging from 15° to 85°. The bottom panel shows profiles for tori around black holes with $a = 0, 0.5$, and 0.998.

larger than the near side. It is even more noticeable that the emission from the half where the emitting gas has a receding projected velocity is dimmed, and the half where the emitting gas has a projected velocity towards us is boosted in brightness. Limb-darkening is also visible at the edges of the torus due to the density profile varying with minor radius.

For the particular parameters that we assumed in our model, the inner hole of the torus is quite large and the higher order images are unobscured. This differs from the opaque thin accretion disks in the previous chapter, where the marginally stable orbit is close to the event horizon in the Kerr black hole case. In disks, only when the observer's inclination is large do the higher order images present a relatively large fraction of the observed flux. However, in these torus models the indirect images contribute a significant amount of flux at all viewing angles. This is mostly due to the fact that the torus is optically thin, and the indirect images are not obscured. Such differences between the transparent tori considered here and the opaque thin disks described in the previous chapter implies that the profiles of their emission lines could be very different.

The line profiles from the semi-transparent tori are different from those from the disk models and also from the 'solid' torus models. The reason why they differ from the solid torus models is that there is no self-obscuration. The fast moving inner gas is visible, producing the red and blue wings of the line profile. The line profiles from the semi-transparent tori differ from those from disks at high inclination. Viewed from angles of about 60° onwards, the line profile stays virtually the same, instead of turning into a flat-topped wedge as happens for disks.

When the black hole spin parameter changes, the line profile from the semi-transparent torus does not. This is due to the inner edge of the torus being far from the black hole event horizon. The change in spin parameter does not alter the inner edge of the torus much, as it depends more on the distribution of pressure forces via the angular velocity profile.

When the iron K$\beta$ line is added to the K$\alpha$ line, the profile gains a third peak on

the blue wing. The rest of the line profile looks roughly the same as before. This extra peak appears at all inclinations, and stays at roughly the same size, shape and relative location in the line profile. The relativistic Doppler smearing is not strong enough to blur the K$\alpha$ and K$\beta$ lines together so much that they cannot be separated.

## 5.4 Partially Opaque Tori

The assumption taken above, of the absorption being negligible breaks down as the central number density increases. Eventually, the opacity due to electron scattering (and photoelectric opacity at low photon energy) becomes important and the tori become optically thick. Thus a more correct model of the radiative transfer physics will use the Thomson cross section. This isn't significantly different from the more correct Compton cross section, since the characteristic energies here are much smaller than an electron rest mass.

Constructing a 'toy' model of the radiative processes within an accretion torus in the central engine of an AGN, requires model of the continuum emission. This can be done by assuming that the low energy emissivity is dominated by Bremsstrahlung. The characteristic temperature for this emission is low - of order 0.01KeV. Since the torus is optically thick, and has a position-dependent temperature, this emission will be thermalised into some form of modified black-body spectrum. The high energy part of real spectra is dominated by a power-law caused by Compton scattering. This is emulated as a power law underlying the free-free emission spectrum.

The assumed spectral emissivities are given by

$$\sigma_p \propto \rho {E_0}^{2.5} \tag{5.34}$$

$$\sigma_B \propto \rho^2 \sqrt{E_0} \exp(-E_0/\Theta) \ , \tag{5.35}$$

where $\sigma_p$ is the power law emissivity, $\sigma_B$ is the Bremsstrahlung emissivity, $E_0$ is the photon energy in the gas rest frame, $\Theta$ is the relativistic temperature in units of the

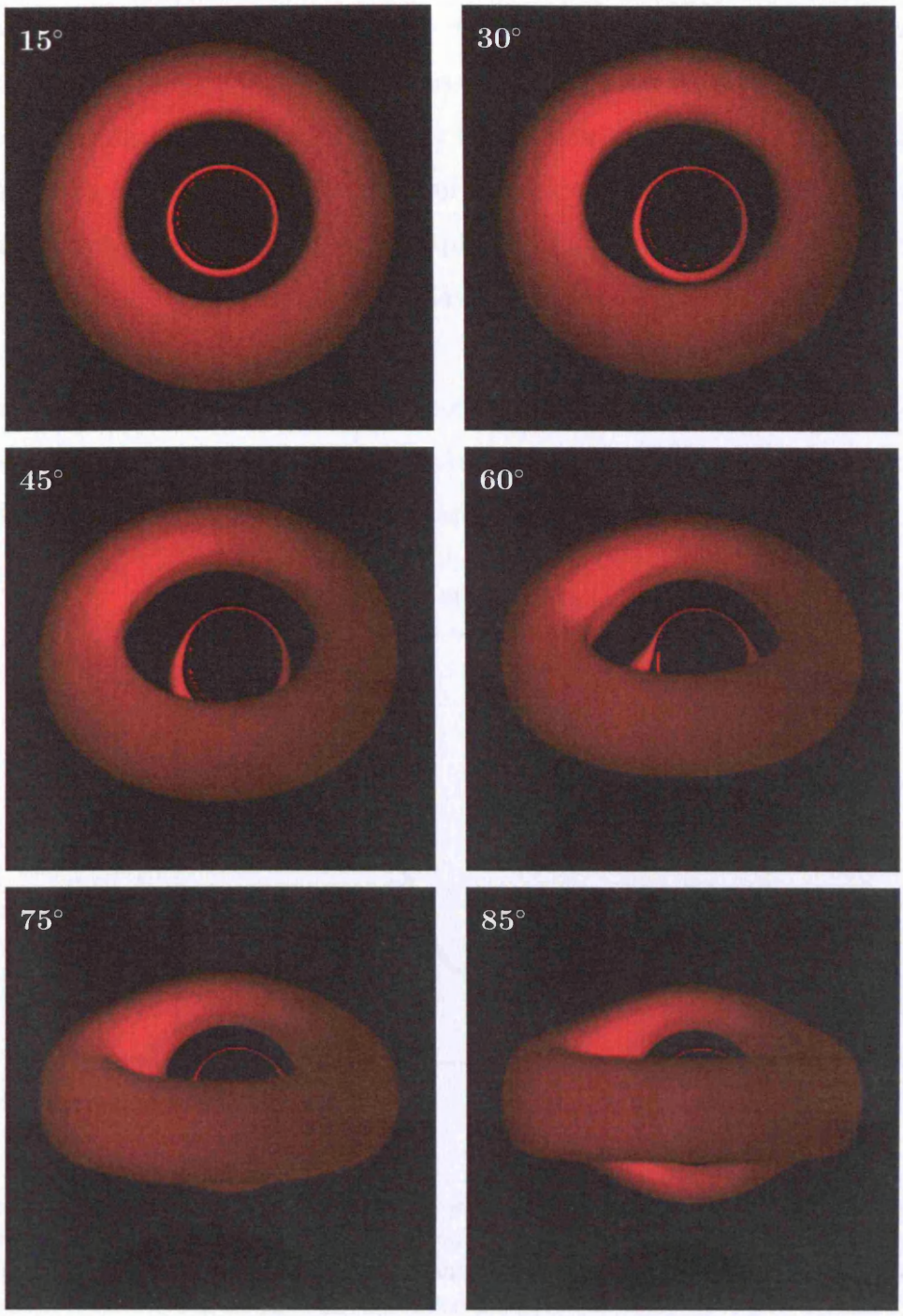


Figure 5.5: Surface brightness images of semi opaque accretion tori around a Kerr black holes viewed at inclination angles of 15°, 30°, 45°, 75°, 85° and 89°. Both line and continuum emission is included (see §5.4) The black holes have a spin parameter $a = 0.998$. Note that due to dynamic range issues, the images have been normalized such that the brightest pixel in each image is the same intensity.

electron rest mass, and $\rho$ is the density. Also assume that there is line emission as well, and use the same relative line ratios as the previous section.

The resulting spectra are dominated by the low energy flux. This causes the images to appear very red in false-colour compares to the line-only images. The spectral profiles in figure 5.6. have been placed in log-log form also for this reason - the line emission and underlying power law would be otherwise completely invisible on the graph.

The tori in this section differ from those in the previous section only in that the emissivity and opacities have changed. As can be seen in figure 5.5., this causes a large difference in the observed images, and in figure 5.6. the observed flux.

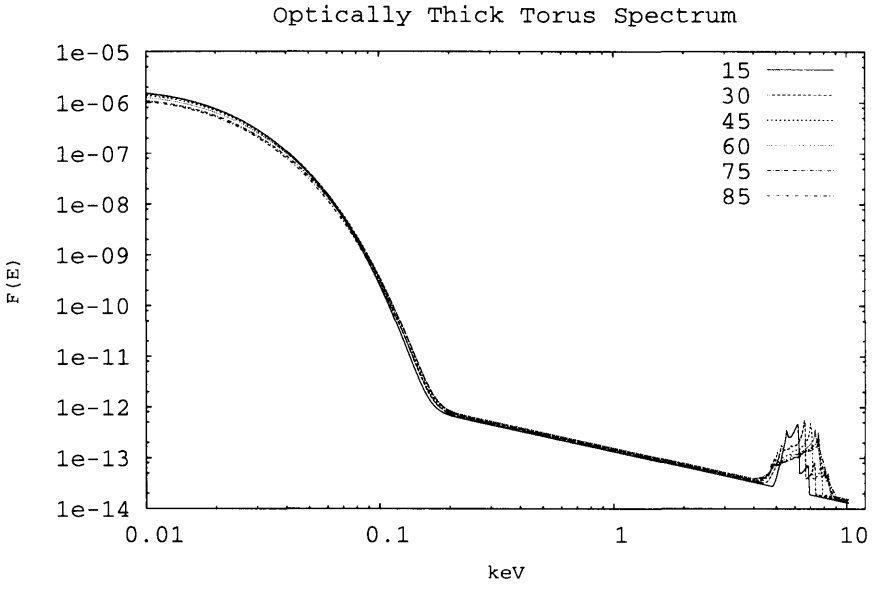


Figure 5.6: Model spectra from accretion tori with an optically thin thermal free-free continuum, a power-law with spectral index 1.5, and two Iron K lines. (See §5.4) This plot shows that altering the inclination angle does not alter the continuum significantly, and shows how important the line emission is in determining the parameters of astrophysical systems.

As in §5.3, these tori appear to be limb-darkened. However, instead of being purely density-driven emission as in the previous section, there is also temperature dependence. Oblique rays do not penetrate very far into the torus, and thus they

mainly sample the surface. However, nearly perpendicular rays penetrate much more deeply on average and reach the hotter sub-surface layers. This temperature stratification means that surfaces oriented face-on to the observer will appear much brighter than those viewed at high inclination.

This section shows how an ad-hoc model of the spectral features of a central engine of an AGN may be constructed. However, the results are essentially dependent on the assumed details of the emissivity function. There is very little physics behind the absolute normalisation of the components, and the results here have just used features that give reasonable results by eye. An improved model of what is observable requires a link between the atomic physics in the emission and absorption (scattering) processes and the global physics of the accretion flow. The next chapter explores the first step in calculating a self-consistent continuum.

## 5.5 Discussion

I first investigate the line emission from optically thin tori to test to see whether the line profiles change from those of the optically thick tori. As can be seen by comparing figures 4.5. and 5.3. there are definite differences. The profiles from optically thick tori change from a 'hump' shape to doubly peaked shapes then back to 'humps' as the observers inclination angle is increased. The line profiles from the optically thin tori are doubly peaked at all inclination angles.

The difference is that the emission from the optically thin tori come from throughout the volume of the torus, whereas the emission from the optically thick torus can only come from its surface. Thus the obscuration which removes the red and blue wings of the line profile in the optically thick case does not happen in the optically thin case. This makes the line profiles from the optically thin torus similar to those from infinitesimally thin accretion disks at low inclination angles. However, at large inclinations the emitted spectrum doesn't look much like those of disks, and stays similar to the profile from a disk viewed at an inclination of 45°.

Since the tori do not extend as close to the black hole as thin disks due to the different location of the marginally stable orbit, the red wing of the line profiles are not as extended. The lack of red wing combined with the nearly invariant shape of the line profile at large inclination angles may mean that these optically thin torus models could emulate the emission from thin accretion disks with totally different parameters. For example, a torus around a Kerr black hole with $a = 0.998$, viewed at an inclination angle of 85° gives similar line profiles to a thin disk around a Schwarzschild black hole with $a = 0$, viewed at an inclination of 45°.

I also investigated changing the black hole spin to determine how sensitive the line profiles from the optically thin tori were to that change. Unfortunately, the lines do not change very much at all, so if these torus models are realistic, then there may be great difficulty in deriving the black hole spin from spectral information. Since line profiles are green functions, any spectral feature from the torus with the same radial emissivity law will have the same unfortunate property.

As well as investigating single lines, I looked at the effects of combining the emission from the iron K$\alpha$ and K$\beta$ lines. Adding in the K$\beta$ line causes a second hump to appear on blue wing of the spectral profile. Figure 5.4. shows how this feature exists at all inclination angles. Relativistic smearing does not remove it, and in general at all inclinations the spectrum has at least three peaks. (At high inclination there is an extra weak peak at around the line rest frequency.)

Finally, I looked at the effects of a more realistic opacity: electron scattering. Since scattering with optical depths larger than one cannot be easily included in ray tracing calculations, I simulated its effects by using an absorption term. At the electron densities typical for AGN accretion disks, this makes the torus optically thick, like those in chapter 4. However, there is a thin atmosphere above the photosphere of the torus where effects such as limb darkening occur which are not included in the simple emitting surface of chapter 4.

The line profiles from the absorbing optically thick torus were different from both the disk and other torus models. In common with the solid torus model, the

red and blue wings were strongly suppressed due to self-obscuration. However, at high inclination angles there was much more flux, and the line profile did not change much from 60° on upwards. This is similar to what happened in the optically thin torus, where the high inclination lines are also similar. However, the shape of the line was quite different to the optically thin case, being much more of a 'hump' than a 'wedge'.

# Chapter 6

# Moment Formalisms for General Relativistic Scattering

The ray-tracing method is not applicable in solving the radiative transfer equation when scattering is dominant. In this chapter, I present a new moment formulation and use it to solve the radiative transfer equation.

For calculation of emission from scattering dominated accretion tori around black holes, the classical moment method described in chapter 1 needs to be modified into a covariant form. Therefore we must expand the moments in terms of tensors. In principle, the more moment tensors we consider in the expansion, the better the result in approximating the "true" situation. The general relativistic moment method requires a closure condition as in the classical formulation, and this closure condition must also be covariant.

## 6.1 The Thorne (1981) Moment Method

An expansion was proposed by Thorne (1981), where the moment tensors are defined as

$$M_{\nu}^{\alpha_1\alpha_2\ldots\alpha_x} \equiv \int I_{\nu}(n^{\alpha_1}+u^{\alpha_1})\ldots(n^{\alpha_x}+u^{\alpha_x})d\Omega\ , \tag{6.1}$$

where $u^\alpha$ is the four-velocity of a preferred frame, usually the rest frame of the medium, $I_\nu$ is the intensity in that frame, and $n^\alpha$ is the directional unit vector of the photon in that frame. These tensors are symmetric as all indices are treated equally.

Consider the identities,

$$n^\alpha n_\alpha = 1, \tag{6.2}$$

$$u^\alpha n_\alpha = 0. \tag{6.3}$$

Consider also the fact that

$$n^\alpha \propto P^\alpha_\beta k^\beta. \tag{6.4}$$

It follows that

$$n^\alpha = \frac{k^\alpha}{E} - u^\alpha \ , \tag{6.5}$$

and

$$k^\alpha = E(n^\alpha + u^\alpha) = Em^\alpha \ , \tag{6.6}$$

where $E = -u^\alpha k_\alpha$, and $m^\alpha \equiv n^\alpha + u^\alpha$. Integration over the unit sphere defined by all possible values of $n^\alpha$ yields

$$\int \prod_i^x n_i^\alpha d\Omega = \begin{cases} 0 & \text{if } x \text{ is even} \\ \dfrac{4\pi}{x+1} P^{(\alpha_1\alpha_2} \ldots P^{\alpha_{x-1}\alpha_x)} & \text{if } x \text{ is odd} \end{cases} \tag{6.7}$$

Note that $M_\nu^{\alpha_1\alpha_2\ldots\alpha_x}$ contains redundant information, as can be seen by the following relations

$$\begin{aligned} M_\nu^{\alpha_1\alpha_2\ldots\alpha_{x-1}}{}_{\alpha_1} &= 0, \\ M_\nu^{\alpha_1\alpha_2\ldots\alpha_x} u_{\alpha_x} &= -M_\nu^{\alpha_1\alpha_2\ldots\alpha_{x-1}} \ , \\ M_\nu^{\alpha_1\alpha_2\ldots\alpha_x} P_{\alpha_{x-1}\alpha_x} &= M_\nu^{\alpha_1\alpha_2\ldots\alpha_{x-2}} \ . \end{aligned} \tag{6.8}$$

The moment tensor of order $x$ therefore contains all the lower order moment tensors. Thorne (1981) removed this redundancy by taking the projected trace-free part of

the moment tensors. The result is known as a projected, symmetric, trace-free tensor moment:

$$\mathcal{M}_\nu^{\alpha_1\alpha_2\ldots\alpha_x} = (M_\nu^{\alpha_1\alpha_2\ldots\alpha_x})^{\mathrm{PSTF}} \ . \tag{6.9}$$

The intensity in the $u^\alpha$ frame is then given by

$$I_\nu = \sum_{x=0}^{\infty} \frac{(2x+1)!!}{4\pi x!} \mathcal{M}_\nu^{\alpha_1\alpha_2\ldots\alpha_x} \ . \tag{6.10}$$

## 6.2 A New Moment Method

Notice that what we need in the radiative transfer calculation is a simple description of $\mathcal{I}_\nu$, the relativistic intensity at each point in space. If equation (6.10) can be simplified, then the calculations can be simplified. This can be achieved by choosing new moments, with a trade-off that more complicated forms than equations (6.1) and (6.9) are required.

I consider an expansion of the intensity $\mathcal{I}(x^\alpha, k^\alpha)$:

$$\mathcal{I} = a_0 J + a_1 J_\alpha n^\alpha + a_2 J_{\alpha_1\alpha_2} n^{\alpha_1} n^{\alpha_2} + a_3 J_{\alpha_1\alpha_2\alpha_3} n^{\alpha_1} n^{\alpha_2} n^{\alpha_3} + \ldots \tag{6.11}$$

where these $J$'s are an orthogonal set of symmetric tensors. (From here on in this chapter, the $\nu$ dependences in $\mathcal{I}$, and $J$ are treated as implicit, to avoid cluttering the notation.) Any antisymmetric component of the moment tensors cancels out due to the symmetry in the definition (6.11). Orthogonality demands

$$\frac{1}{4\pi} \int J_{\alpha_1\ldots\alpha_x} J_{\alpha_{x+1}\ldots\alpha_y} n^{\alpha_1} \ldots n^{\alpha_y} d\Omega = 0, \tag{6.12}$$

i.e.

$$J_{\alpha_1\ldots\alpha_x} J_{\alpha_{x+1}\ldots\alpha_y} P^{(\alpha_1\alpha_2} \ldots P^{\alpha_{y-1}\alpha_y)} = 0. \tag{6.13}$$

By means of the "pigeon-hole principle", the above holds if

$$J^{\alpha_1\alpha_2\alpha_3\ldots} P_{\alpha_1\alpha_2} \equiv 0. \tag{6.14}$$

When one of the $J$'s has an odd number of indices and the other even, then the total will be odd, so the result of the integral in equation (6.12) will be zero. Therefore, the

only interesting case is where the difference in the number of indices is a multiple of two. Now, suppose equation (6.14) holds, only when the projection tensors operate on indices from two different $J$'s will the result be non-zero. This can only happen if they have the same number of indices. Thus equation (6.14) is sufficient for equation (6.12) to hold.

The projection identity and orthogonality condition also hold for the projected symmetric trace-free tensors in Thorne (1981). In the method described here, only the result of adding the two terms together is zero. This gives an extra degree of freedom which allows the series expansion of $\mathcal{I}$ to be summed explicitly.

Noting that only the part of the $J$'s which has been projected perpendicular to $u^\alpha$ is used in equation (6.11), we are free to arbitrarily set $\mathcal{J}^{\alpha_1\alpha_2\alpha_3\cdots}u_{\alpha_1}$, where we may define a set of new $\mathcal{J}$'s which still satisfy all the above equations for the $J$'s. I.e. if

$$\mathcal{J}^{\alpha_1\alpha_2\alpha_3\cdots}u_{\alpha_1} \propto \mathcal{J}^{\alpha_2\alpha_3\cdots}, \tag{6.15}$$

then equation (6.11) telescopes, where these new $\mathcal{J}$'s refer to those in the truncated series with $x$ indices and $x+1$ terms. Different truncations will give differing values for the projected part of the $\mathcal{J}$'s. However, since the $\mathcal{J}$'s are linear objects and the resulting binomial expansion contains a term of every order up to $x$th, one may use for the $x$th order approximation

$$\mathcal{I}_x = \mathcal{J}_{\alpha_1\alpha_2\alpha_3\ldots\alpha_x} m_1^\alpha m_2^\alpha m_3^\alpha \ldots m_x^\alpha \ . \tag{6.16}$$

Thus the intensity can be expressed simply in terms of $\mathcal{J}$ instead of a sum of the moments. The trade-off is that the definitions of the $\mathcal{J}$'s in terms of integrals of the intensity are more complex. This is the major difference between my moment method and that in Thorne (1981), which has simple expressions for the moments in terms of integrals of the intensity.

The new method here does not require the that the moments be evaluated directly as they are included implicitly in the calculation. However it is possible to show that expressions for them can be obtained. First set $\mathcal{J}^{\alpha_1\alpha_2\alpha_3\cdots}u_{\alpha_1} = \mathcal{J}^{\alpha_2\alpha_3\cdots}$.

(In fact we may consider any linear combination of lower order $\mathcal{J}$'s, so long as no zero terms appear in the binomial expansion). Thus

$$\mathcal{I}_x = \sum_{i=0}^{x} a_i \mathcal{J}_{\alpha_1\alpha_2\alpha_3\ldots\alpha_i} n_1^\alpha n_2^\alpha n_3^\alpha \ldots n_i^\alpha \ , \tag{6.17}$$

where

$$a_i = \frac{x!}{i!(x-i)!} \ . \tag{6.18}$$

Integrating the intensity multiplied by appropriate powers of $n^\alpha$ yields expressions for the $\mathcal{J}$'s:

$$\begin{aligned} \frac{1}{4\pi}\int \mathcal{I}_x n_1^\alpha n_2^\alpha n_3^\alpha \ldots n_j^\alpha d\Omega &= \sum_{i=0}^{j} \frac{a_i}{4\pi}\int \mathcal{J}_{\alpha_1\alpha_2\alpha_3\ldots\alpha_i} n_1^\alpha n_2^\alpha n_3^\alpha \ldots n_{i+j}^\alpha d\Omega \qquad (6.19)\\ &= \sum_{i=0}^{j} \frac{a_i}{i+j+1} \mathcal{J}_{\alpha_1\alpha_2\alpha_3\ldots\alpha_i} P^{(\alpha_1\alpha_2} \ldots P^{\alpha_{i+j-1}\alpha_{i+j})} \ . \end{aligned}$$

Since $P^\alpha_\beta = \delta^\alpha_\beta + u^\alpha u_\beta$,

$$\begin{aligned} \mathcal{J}_{\alpha_1\alpha_2\alpha_3\ldots\alpha_i} P^{(\alpha_1\alpha_2} \ldots P^{\alpha_{2i-1}\alpha_{2i})} &= \mathcal{J}_{\alpha_1\alpha_2\alpha_3\ldots\alpha_i} P^{\alpha_1\alpha_{i+1}} P^{\alpha_2\alpha_{i+2}} \ldots P^{\alpha_i\alpha_{2i}} \\ &= \mathcal{J}^{\alpha_{i+1}\alpha_{i+2}\ldots\alpha_{2i}} + \text{ lower order } \mathcal{J} \text{ terms.} \end{aligned} \tag{6.20}$$

Hence the $i$th order $\mathcal{J}$ can be calculated in terms of the $i-1$ lower order $\mathcal{J}$'s and a weighted integral of $\mathcal{I}$.

## 6.3 The Radiative Transfer Equation

By evaluating the total derivative of $\mathcal{I}_x$ and substituting it into the radiative transfer equation, we obtain the $x$th order approximation. This requires some identities, namely

$$\frac{Dk^\alpha}{d\lambda} = k^\alpha{}_{;\beta} k^\beta = k^\alpha_{;\beta} k^\beta = 0, \tag{6.21}$$

since covariant derivatives commute in empty space, and $k^\alpha = \Phi^{,\alpha}$, where $\Phi$ is the phase of the light ray. Using this result, the total derivative of $E$ simplifies to

$$\frac{DE}{d\lambda} = -\frac{D}{d\lambda}(k^\alpha u_\alpha)$$

$$
\begin{aligned}
&= -k^{\alpha}u_{\alpha;\beta}k^{\beta} \\
&= -E^2 m^{\alpha}u_{\alpha;\beta}m^{\beta} \\
&= -E^2\left(u^{\alpha}n_{\alpha;\beta}n^{\beta} + n^{\alpha}u_{\alpha;\beta}u^{\beta}\right) \\
&= -E^2\xi, \qquad (6.22)
\end{aligned}
$$

where

$$
\xi = \frac{-1}{E^2}\frac{DE}{\partial\lambda} = u^{\alpha}n_{\alpha;\beta}n^{\beta} + n^{\alpha}u_{\alpha;\beta}u^{\beta}\ . \qquad (6.23)
$$

We then evaluate the total derivative of the normalised photon momentum:

$$
\begin{aligned}
\frac{Dm^{\alpha}}{d\lambda} &= \frac{D}{d\lambda}\left(\frac{k^{\alpha}}{E}\right) \\
&= \frac{-1}{E^2}k^{\alpha}\frac{DE}{d\lambda} \\
&= \frac{-1}{E}m^{\alpha}\frac{DE}{d\lambda} \\
&= Em^{\alpha}\xi\ . \qquad (6.24)
\end{aligned}
$$

Therefore

$$
\begin{aligned}
\frac{D\mathcal{J}^{\alpha_1\alpha_2\alpha_3\ldots\alpha_x}(E)}{d\lambda} &= \mathcal{J}^{\alpha_1\alpha_2\alpha_3\ldots\alpha_i}{}_{;\beta}k^{\beta} + \frac{\partial\mathcal{J}^{\alpha_1\alpha_2\alpha_3\ldots\alpha_x}}{\partial E}\frac{DE}{d\lambda} \\
&= E\left(\mathcal{J}^{\alpha_1\alpha_2\alpha_3\ldots\alpha_x}{}_{;\beta}m^{\beta} - \xi\frac{\partial\mathcal{J}^{\alpha_1\alpha_2\alpha_3\ldots\alpha_x}}{\partial\ln E}\right)\ . \qquad (6.25)
\end{aligned}
$$

Hence the expression on the left hand side of the radiative transfer equation can finally be evaluated yielding the $x$th order approximation

$$
\begin{aligned}
\frac{D\mathcal{I}_x}{d\lambda} &= \frac{D}{d\lambda}\left(\mathcal{J}^{\alpha_1\alpha_2\ldots\alpha_x}m_{\alpha_1}m_{\alpha_2}\ldots m_{\alpha_x}\right) \\
&= m_{\alpha_1}m_{\alpha_2}\ldots m_{\alpha_x}\frac{D\mathcal{J}^{\alpha_1\alpha_2\ldots\alpha_x}}{d\lambda} + x\mathcal{J}^{\alpha_1\alpha_2\ldots\alpha_x}\frac{Dm_{\alpha 1}}{d\lambda}m_{\alpha_2}\ldots m_{\alpha_x} \qquad (6.26) \\
&= Em_{\alpha_1}m_{\alpha_2}\ldots m_{\alpha_x}\left[\mathcal{J}^{\alpha_1\alpha_2\alpha_3\ldots\alpha_x}{}_{;\beta}m^{\beta} + \xi\left(x\mathcal{J}^{\alpha_1\alpha_2\alpha_3\ldots\alpha_x} - \frac{\partial\mathcal{J}^{\alpha_1\alpha_2\alpha_3\ldots\alpha_x}}{\partial\ln E}\right)\right].
\end{aligned}
$$

The meaning of the equation above is as follows. The first term in (6.26) describes how the moments vary with space-time. It contains the effects due to the curvature via the covariant derivative. The second term describes "Doppler" effects, where an acceleration in the velocity field $u^{\alpha}$, or in the unit vectors $n^{\alpha}$, will alter the energy and direction of the photons seen in the rest frame. This equation shall be applied to investigate scattering in relativistic tori orbiting Kerr black holes.

## 6.4 Radiative Transfer with Relativistic Thomson Scattering

Before proceeding to solve the equation, we need to specify the scattering kernel in the radiative transfer equation. The correct form of scattering to use is Compton scattering and the Klein-Nishina cross section. This cross section is energy dependent, and very complex analytically. However, this makes it very difficult to solve the integrals.

Do to the analytic difficulty with investigating Compton scattering, I investigate a relativistic form of Thomson scattering instead. This gives the correct bulk-motion relativistic effects, but ignores the thermal motion of the electrons. If the electrons are "cold", as is the case here where the temperature is much less than their rest mass, this is a good approximation.

This assumption of elastic scattering is very good. However, it ignores the cumulative effects of the small energy shifts in the real slightly inelastic process. The energy redistribution causes thermalisation of the photon spectrum, and without it the spectrum is incorrect. However, images produced will be more or less right, as the Thomson cross section is a good approximation in an energy-averaged sense for cold electrons.

In the case of relativistic Thomson scattering, the $x$th order expression for the integrated kernel is

$$\kappa_{\mathrm{T}x} = \frac{3\rho\sigma_{\mathrm{T}}}{16\pi}\int \mathcal{I}_x{}'(1 + n^\alpha n'_\alpha n^\beta n'_\beta)d\Omega'. \tag{6.27}$$

The use of this kernel is justified if the electrons are 'cold', i.e. that the bulk velocities are much higher than the thermal velocities. The flow in an accretion disk is supersonic, and so the condition that the bulk velocity is larger than the thermal velocity is satisfied.

To 0th order, the kernel is $\rho\sigma_{\mathrm{T}}\mathcal{J}$, and to first order $\rho\sigma_{\mathrm{T}}\mathcal{J}^\alpha u_\alpha$. At second order,

the quadrapole term in the cross-section appears

$$\kappa_{\mathrm{T}2} = \rho\sigma_{\mathrm{T}}\left(\mathcal{J}^{\alpha\beta}u_\alpha u_\beta + \frac{1}{10}\mathcal{J}^{\alpha\beta}n_\alpha n_\beta\right). \tag{6.28}$$

The 0th order equations assume that the intensity is isotropic, and thus there is no net flux. This is only valid when there is no temperature variation. The 1st order equation is the lowest order which gives physically meaningful results. The corresponding radiative transfer equation is

$$\begin{aligned} m_\alpha\left[\mathcal{J}^\alpha{}_{,\beta}n^\beta + \Gamma^\alpha_{\delta\beta}\mathcal{J}^\beta m^\delta + \xi\left(\mathcal{J}^\alpha - \frac{\partial\mathcal{J}^\alpha}{\partial(\ln E)}\right)\right] & \\ = -\left(\sigma_{\mathrm{ff}} + \sigma_{\mathrm{T}}\right)\rho\mathcal{J}^\alpha m_\alpha + \sigma_{\mathrm{ff}}\rho\mathcal{B} + \sigma_{\mathrm{T}}\rho\mathcal{J}^\alpha u_\alpha\ , & \end{aligned} \tag{6.29}$$

when terms for free-free absorption and emission are included. In the equation, $\mathcal{B} = B/\nu^3$ is the relativistically invariant Planck function. The use of the single-index moment tensors here is equivalent to using the Eddington approximation, see §6.5. Note that the energy normalisation here requires that everything be measured in the gas rest frame, as opposed to energy at infinity used in previous chapters.

The 2nd order radiative transfer equation contains a quadrapole term in the Thomson cross section:

$$\begin{aligned} m_\alpha m_\beta\left[\mathcal{J}^{\alpha\beta}{}_{,\gamma}n^\gamma + 2\Gamma^\alpha_{\delta\gamma}\mathcal{J}^{\gamma\beta}m^\delta + \xi\left(2\mathcal{J}^{\alpha\beta} - \frac{\partial\mathcal{J}^{\alpha\beta}}{\partial(\ln E)}\right)\right] & \\ = -\left(\sigma_{\mathrm{ff}} + \sigma_{\mathrm{T}}\right)\rho\mathcal{J}^{\alpha\beta}m_\alpha m_\beta + \sigma_{\mathrm{ff}}\rho\mathcal{B} & \\ +\sigma_{\mathrm{T}}\rho\left(\mathcal{J}^{\alpha\beta}u_\alpha u_\beta + \frac{1}{10}\mathcal{J}^{\alpha\beta}n_\alpha n_\beta\right)\ . & \end{aligned} \tag{6.30}$$

The higher order equations do not gain any more terms due to the scattering kernel, but the moment tensors have more indices. The higher the order, the more accurate the approximation to the solution. The number of distinct tensor components goes up as the square of the order because the symmetry, projection and orthogonality conditions reduce the number of free components in the $\mathcal{J}$'s.

## 6.5 Eddington Approximation in New Moment Method

We may pick $(x+1)^2$ $n^\alpha$'s to obtain enough equations to solve for the $(x+1)^2$ distinct components of the $x$th order $\mathcal{J}$ tensor. For instance in first order, we may choose a tetrahedral basis - which can be done by using the non-adjacent corners of a cube; see Fig. 6.1.

Consider the case of a flat-space plane geometry with Thomson scattering and free-free absorption and emission using the new moment method. Thus

$$a^\alpha = 0, \tag{6.31}$$

$$\frac{\partial}{\partial x} = \frac{\partial}{\partial y} = 0. \tag{6.32}$$

The simplified first order radiative transfer equation is

$$m_\alpha \mathcal{J}^\alpha{}_{,\beta} n^\beta = \kappa_{\rm ff} \left(\mathcal{B} - \mathcal{J}^\alpha u_\alpha\right) - \left(\kappa_{\rm ff} + \kappa_{\rm T}\right) \mathcal{J}^\alpha n_\alpha, \tag{6.33}$$

where the opacities, $\kappa_x = \rho\sigma_x$

Choosing the tetrahedral basis set gives four unit vectors

$$n_1 = \frac{1}{\sqrt{3}}\begin{pmatrix} 0 \\ 1 \\ 1 \\ 1 \end{pmatrix},\ n_2 = \frac{1}{\sqrt{3}}\begin{pmatrix} 0 \\ 1 \\ -1 \\ -1 \end{pmatrix},\ n_3 = \frac{1}{\sqrt{3}}\begin{pmatrix} 0 \\ -1 \\ 1 \\ -1 \end{pmatrix},\ n_4 = \frac{1}{\sqrt{3}}\begin{pmatrix} 0 \\ -1 \\ -1 \\ 1 \end{pmatrix}. \tag{6.34}$$

By substituting them equation (6.33), we obtain four equations for the four unknowns $\mathcal{J}^\alpha$:

$$\begin{aligned} \frac{1}{\sqrt{3}}\frac{\partial \mathcal{J}^0}{\partial z} + \frac{1}{3}\frac{\partial}{\partial z}\left(\mathcal{J}^1 + \mathcal{J}^2 + \mathcal{J}^3\right) &= -\left(\kappa_{\rm ff} + \kappa_{\rm T}\right)\left[\mathcal{J}^0 + \frac{1}{\sqrt{3}}\left(\mathcal{J}^1 + \mathcal{J}^2 + \mathcal{J}^3\right)\right] \\ &\quad + \kappa_{\rm T}\mathcal{J}^0 + \kappa_{\rm ff}\mathcal{B}, \end{aligned} \tag{6.35}$$

$$\begin{aligned} -\frac{1}{\sqrt{3}}\frac{\partial \mathcal{J}^0}{\partial z} + \frac{1}{3}\frac{\partial}{\partial z}\left(-\mathcal{J}^1 + \mathcal{J}^2 + \mathcal{J}^3\right) &= -\left(\kappa_{\rm ff} + \kappa_{\rm T}\right)\left[\mathcal{J}^0 + \frac{1}{\sqrt{3}}\left(\mathcal{J}^1 - \mathcal{J}^2 - \mathcal{J}^3\right)\right] \\ &\quad + \kappa_{\rm T}\mathcal{J}^0 + \kappa_{\rm ff}\mathcal{B}, \end{aligned} \tag{6.36}$$

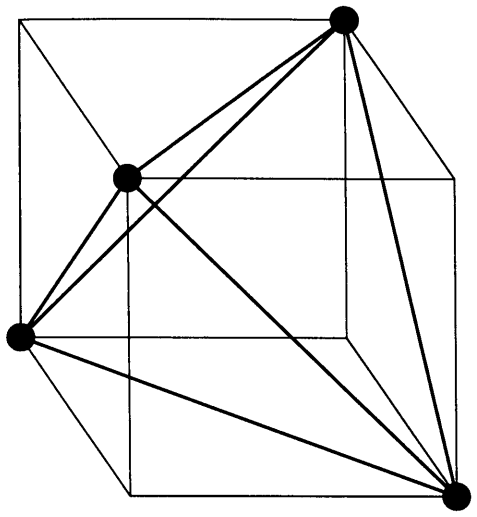

Figure 6.1: Illustration of the tetrahedral basis set used in the numerical algorithm used to solve the radiative transfer equation. Opposite vertexes of a cube form a tetrahedral basis set. This shows the tetrahedron formed by connecting these points.

$$-\frac{1}{\sqrt{3}}\frac{\partial \mathcal{J}^0}{\partial z}+\frac{1}{3}\frac{\partial}{\partial z}\left(\mathcal{J}^1-\mathcal{J}^2+\mathcal{J}^3\right) = -\left(\kappa_{\rm ff}+\kappa_{\rm T}\right)\left[\mathcal{J}^0+\frac{1}{\sqrt{3}}\left(-\mathcal{J}^1+\mathcal{J}^2-\mathcal{J}^3\right)\right], \\ +\kappa_{\rm T}\mathcal{J}^0+\kappa_{\rm ff}\mathcal{B}, \tag{6.37}$$

$$\frac{1}{\sqrt{3}}\frac{\partial \mathcal{J}^0}{\partial z}+\frac{1}{3}\frac{\partial}{\partial z}\left(-\mathcal{J}^1-\mathcal{J}^2+\mathcal{J}^3\right) = -\left(\kappa_{\rm ff}+\kappa_{\rm T}\right)\left[\mathcal{J}^0+\frac{1}{\sqrt{3}}\left(-\mathcal{J}^1-\mathcal{J}^2+\mathcal{J}^3\right)\right] \\ +\kappa_{\rm T}\mathcal{J}^0+\kappa_{\rm ff}\mathcal{B}. \tag{6.38}$$

Equations "(6.35) + (6.36) + (6.37) + (6.38)" gives

$$\frac{\partial \mathcal{J}^3}{\partial z}=3\kappa_{\rm ff}\left(\mathcal{B}-\mathcal{J}^0\right); \tag{6.39}$$

Equations "(6.35)) - (6.36) - (6.37) + (6.38)" gives

$$\frac{\partial \mathcal{J}^0}{\partial z}=-\left(\kappa_{\rm ff}+\kappa_{\rm T}\right)\mathcal{J}^3. \tag{6.40}$$

By differentiating with respect to $z$, and substituting for $\partial\mathcal{J}^3/\partial z$ we obtain the radiation diffusion equation from the Eddington approximation:

$$\frac{\partial^2 \mathcal{J}^0}{\partial z^2}=-3\left(\kappa_{\rm ff}+\kappa_{\rm T}\right)\kappa_{\rm ff}\left(\mathcal{B}-\mathcal{J}^0\right). \tag{6.41}$$

## 6.6 Numerical Algorithm

The radiative transfer equation in the moment representation is an advection-reaction equation. It can be solved by using a second order implicit upwind method, through an expansion of the spacial and energy derivatives into the one-sided approximation

$$\frac{df}{dx} \approx \left(3f(x) - 4f(x+h) + f(x+2h)\right)/2h + O(h^3), \tag{6.42}$$

where $h$ is the grid step size. This formula is derived from the Taylor expansion

$$\begin{aligned} f(x+h) &\approx f(x) + h\frac{df}{dx} + \frac{h^2}{2}\frac{d^2f}{dx^2} + \frac{h^3}{6}\frac{d^3f}{dx^3} \ldots \\ f(x+2h) &\approx f(x) + 2h\frac{df}{dx} + 2h^2\frac{d^2f}{dx^2} + \frac{4h^3}{3}\frac{d^3f}{dx^3} \ldots, \end{aligned} \tag{6.43}$$

yielding a error term of

$$\frac{2h^3}{3}\frac{d^3f}{dx^3}\,. \tag{6.44}$$

For more accuracy, a third order method was tried with

$$\frac{df}{dx} \approx \left(11f(x) - 18f(x+h) + 9f(x+2h) - 2f(x+3h)\right)/6h + O(h^4). \tag{6.45}$$

However this proved to be numerically unstable in practise. Replacing it with a fourth order method interior to the boundary region restored stability:

$$\frac{df}{dx} \approx \left(25f(x) - 48f(x+h) + 36f(x+2h) - 16f(x+3h) + 3f(x+4h)\right)/12h + O(h^5). \tag{6.46}$$

In the calculation, a hybrid algorithm is used. The fourth order method is used in the interior points, and the second and third order methods is used near the boundary. This yields a formally second order numerical scheme, with the extra accuracy in the interior preventing instabilities.

Outgoing flux boundary conditions are then required to completely specify the problem. Since the differential equation is linear, components of the solution are linearly additive. We proceed by dividing the flux into several parts, each travelling in a certain direction. For example, in the one dimensional case (imagine a one

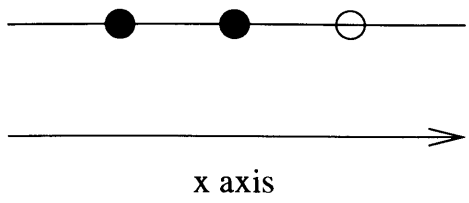


Figure 6.2: This schematic diagram describes the solution of the one dimensional second upwind numerical scheme. The derivative at the open circled point is calculated from the known values at the filled circled points together with the future values at the open circled point. The radiative transfer equation closes the system allowing the open circled points moment vector to be obtained. In general, more than one moment is calculated per point, so a matrix of size $n$ needs to be inverted, where $n$ is the number of moments. By scanning in the direction away from the boundary, only one unknown moment vector per point is required. This ordering of solving for values at the points reduces the implicit problem into one which is nearly explicit. Thus the time taken to solve this case is linear in the number of points, but proportional to the cube of the number of moments used.

dimensional star) we may define

$$\mathcal{I} = 1/2\,(\mathcal{I}_- + \mathcal{I}_+)\,, \tag{6.47}$$

where $\mathcal{I}_-$ is left-going, and $\mathcal{I}_+$ right-going flux. Note that the right-going flux must be zero on the left boundary due to the zero incoming flux condition. Similarly, the left-going flux must be zero on the right boundary.

As the radiative transfer equation has an energy derivative term as well as spatial derivatives, an energy boundary condition is also required. At high energies, $\mathcal{B}$ tends to zero, thus the energy derivative tends to zero. This implies that the flux must tend to a constant value of $\mathcal{I}$, which also must be zero; otherwise there would be an infinite amount of energy in the flux.

The 2D case is similar to the 1D case, except that there are two spatial boundary conditions. Unfortunately, decomposing the problem into "sub-problems" which are zero along the boundary does not work. The reason is that if integration proceeds away from a zero-flux boundary, the opposite boundary may have regions with negative flux going outwards. This negative outwards flux is the same as positive flux heading into the computational grid, breaking the outgoing flux boundary condition; see Fig. 6.4.

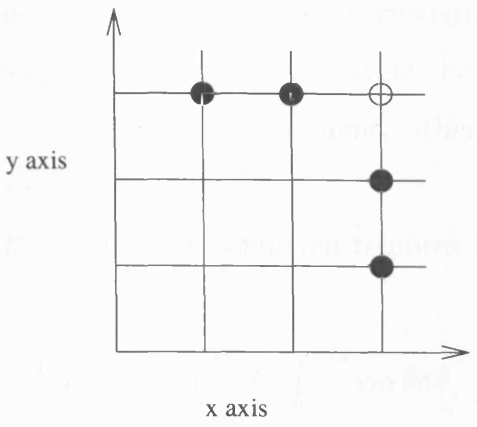


Figure 6.3: This schematic portrays the solution of the two dimensional, second order upwind numerical scheme. Just like the one dimensional case, the derivative at the open circled point is calculated from the known values at the filled circled points together with the future values at the open circled point. Due to the lack of axisymmetry, many more moments are required, which makes the two dimensional case slower. Fortunately, the trick of ordering the points works like it does in the 1D case. By scanning in the $x$ direction and $y$ direction away from the boundary, it is possible to have only one unknown set of values per point, thus making the solution linear in the number of points.

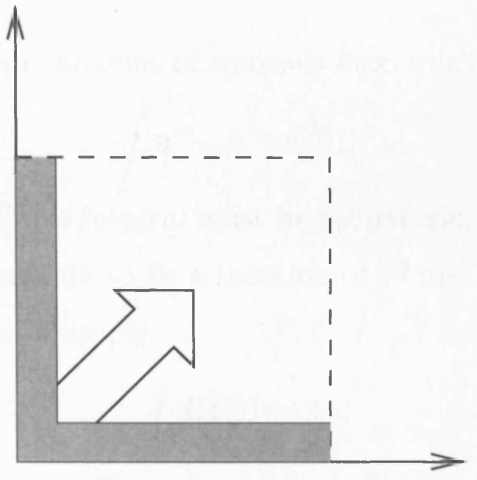

Figure 6.4: Illustration of the integration of the 2D moment equation with the outgoing flux boundary condition. The integration proceeds away from two adjacent edges. Once it reaches the far boundaries, the flux may be negative. This corresponds to a positive flux ingoing into the region, thus breaking the boundary conditions. To satisfy the outgoing flux condition perturbations must be added along the initial boundary to cancel this negative flux.

To resolve this inconsistency, we need to find perturbations of the 'left' boundary that will cancel the spurious ingoing flux on the 'right' boundary. These perturbations must not have any outgoing flux component, otherwise the 'left' boundary condition will then be broken.

Solving the outgoing flux boundary condition requires the definition of the half-space integral operator

$$\int d(\tfrac{1}{2}\Omega) \equiv \int_0^{2\pi} d\phi \int_0^{\pi/2} \sin\theta d\theta, \tag{6.48}$$

where the hemisphere normal is defined to be $z^\alpha$ such that

$$\begin{aligned} z^\alpha z_\alpha &= 1, \\ z^\alpha n_\alpha &= \cos\theta, \\ z^\alpha u_\alpha &= 0. \end{aligned} \tag{6.49}$$

Also useful, is an arbitrary unit vector $x^\alpha$ perpendicular to $z^\alpha$ and $u^\alpha$ such that

$$x^\alpha n_\alpha = \sin\theta \sin\phi. \tag{6.50}$$

In order to solve for the amount of spurious flux, solution of

$$\int n^{\alpha_1} ... n^{\alpha_x} d(\tfrac{1}{2}\Omega). \tag{6.51}$$

is required. The result of this integral must be symmetric, and perpendicular to $u^\alpha$. By symmetry, it must evaluate to be a function of $z^\alpha$ and $P^{\alpha\beta}$, but not $x^\alpha$.

The zeroth order case is simply

$$\int d(\tfrac{1}{2}\Omega) = 2\pi. \tag{6.52}$$

The first order case must be a linear function of $z^\alpha$:

$$\int n^\alpha d(\tfrac{1}{2}\Omega) = A_0 z^\alpha \ , \tag{6.53}$$

which can be solved by multiplying both sides by $z_\alpha$

$$\begin{aligned} \int z_\alpha n^\alpha d(\tfrac{1}{2}\Omega) &= A_0 \ , \\ 2\pi \int_0^{\pi/2} \cos\theta \sin\theta d\theta &= \pi = A_0 \ . \end{aligned} \tag{6.54}$$

Hence,

$$\int n^\alpha d(\tfrac{1}{2}\Omega) = \pi z^\alpha \ . \tag{6.55}$$

The second order case must be a linear combination of $z^\alpha z^\beta$ and $P^{\alpha\beta}$:

$$\int n^\alpha n^\beta d(\tfrac{1}{2}\Omega) = A_0 z^\alpha z^\beta + A_1 P^{\alpha\beta} \ . \tag{6.56}$$

Multiplication of equation (6.56) by $z_\alpha z_\beta$ and $x_\alpha x_\beta$ provides two equations for the two unknowns

$$\begin{aligned} \int (n^\alpha z_\alpha)^2 d(\tfrac{1}{2}\Omega) &= A_0 + A_1 \ , \\ \int (n^\alpha x_\alpha)^2 d(\tfrac{1}{2}\Omega) &= A_1 \ . \end{aligned} \tag{6.57}$$

It follows that

$$\int n^\alpha n^\beta d(\tfrac{1}{2}\Omega) = \frac{2\pi}{3} P^{\alpha\beta} \ . \tag{6.58}$$

The third order case is slightly more complicated. The symmetry requirement imposes that

$$\int n^\alpha n^\beta n^\gamma d(\tfrac{1}{2}\Omega) = A_0 z^\alpha z^\beta z^\gamma + A_1 P^{(\alpha\beta} z^{\gamma)} \ . \tag{6.59}$$

$A_0$ and $A_1$ can be obtained by using

$$\int (z^\alpha n_\alpha)^3 d(\tfrac{1}{2}\Omega) = A_0 + A_1 \ , \tag{6.60}$$

and

$$\int (x^\alpha n_\alpha)^2 z^\beta n_\beta d(\tfrac{1}{2}\Omega) = \frac{1}{3} A_1 \ , \tag{6.61}$$

which yields

$$\int n^\alpha n^\beta n^\gamma d(\tfrac{1}{2}\Omega) = \frac{\pi}{4} \left( 3P^{(\alpha\beta} z^{\gamma)} - z^\alpha z^\beta z^\gamma \right) . \tag{6.62}$$

Similarly, the result for the fourth order equation is

$$\int n^\alpha n^\beta n^\gamma n^\delta d(\tfrac{1}{2}\Omega) = \frac{2\pi}{5} P^{(\alpha\beta} P^{\gamma\delta)} \ . \tag{6.63}$$

The outgoing flux boundary condition is

$$\int \mathcal{I} d(\tfrac{1}{2}\Omega) = 0. \tag{6.64}$$

Substituting in the different approximations of $\mathcal{I}$ yields the boundary condition suitable for each order. For 0th order,

$$\begin{aligned} \int \mathcal{J} d(\tfrac{1}{2}\Omega) &= 0, \\ 2\pi \mathcal{J} &= 0, \\ \mathcal{J} &= 0. \end{aligned} \tag{6.65}$$

For 1st order,

$$\begin{aligned} \int \mathcal{J}^\alpha m_\alpha d(\tfrac{1}{2}\Omega) &= 0, \\ \int \mathcal{J}^\alpha u_\alpha + \mathcal{J}^\alpha n_\alpha d(\tfrac{1}{2}\Omega) &= 0, \\ \mathcal{J}^\alpha u_\alpha + \frac{1}{2}\mathcal{J}^\alpha z_\alpha &= 0. \end{aligned} \tag{6.66}$$

For 2nd order,

$$\begin{aligned} \int \mathcal{J}^{\alpha\beta} m_\alpha m_\beta d(\tfrac{1}{2}\Omega) &= 0, \\ \mathcal{J}^{\alpha\beta} u_\alpha u_\beta + \mathcal{J}^{\alpha\beta} u_\alpha z_\beta &= 0. \end{aligned} \tag{6.67}$$

For 3rd order,

$$2\mathcal{J}^{\alpha\beta\gamma} u_\alpha u_\beta u_\gamma + 3\mathcal{J}^{\alpha\beta\gamma} u_\alpha u_\beta z_\gamma - \frac{1}{4}\mathcal{J}^{\alpha\beta\gamma} z_\alpha z_\beta z_\gamma = 0. \tag{6.68}$$

and for 4th order,

$$\mathcal{J}^{\alpha\beta\gamma\delta} u_\alpha u_\beta u_\gamma u_\delta + 4\mathcal{J}^{\alpha\beta\gamma\delta} u_\alpha u_\beta u_\gamma z_\delta - \mathcal{J}^{\alpha\beta\gamma\delta} u_\alpha z_\beta z_\gamma z_\delta = 0. \tag{6.69}$$

Note that the $\mathcal{J} = 0$ condition for the 0th order case is another reason why the simplest realistic case is that of first order. No flux escapes to the observer at zeroth order.

The perturbation made at the boundaries must not break the corresponding condition. This means that it must be perpendicular to $z^\alpha$ as well as $u^\alpha$. Also, due to axisymmetry in the torus problem, the $\hat{\phi}$ component of the perturbation must be zero. Thus on the boundaries of maximal and minimal $r$, the perturbation is in the $\hat{\theta}$ direction, and vice-versa.

By perturbing each individual boundary cell, and collating the effects on the opposite boundaries in a matrix. A direct process of inversion calculates the perturbation required to remove the boundary condition violating flux. By solving for the perturbations required on all the boundaries, the appropriate corrections are added to the resulting flux. This is possible due to the fact that the moment form of the radiative transfer equation is a linear PDE, and solutions can be superimposed.

Assuming that the energies decouple, which is true for Thomson scattering, the total time to complete the calculation is the sum of the time taken for the required number of 'sweeps' with given perturbed boundary conditions, together with the matrix inversion needed to determine the correct outgoing flux. This is proportional to

$$t \propto N_e(N_x + N_y)N_xN_yN_m^3 \ , \tag{6.70}$$

for the total time for all the 'sweeps', where $N_e$ is the number of energy points, $N_x$ and $N_y$ the number of points along the axis, and $N_m$ the number of moments required. For the matrix inversion of the boundary conditions,

$$t \propto N_e(N_x + N_y)^3N_m^3 \ . \tag{6.71}$$

Thus the total time is dominated by the boundary conditions solver. (Note that $N_m = (\text{order} + 1)^2$, so that high orders take very much longer than the first order case investigated in this thesis.)

In order to avoid numerical instability, the physical transport described by the equations (6.29) or (6.30) needs to be inherent within the numerical scheme. For the 1D case, this is trivial: The computation must upwind in the correct direction, i.e. away from the zero-flux boundary. The 2D case is complicated by the fact that without a careful choice of the normal vectors $n^\alpha$, the method is unstable. However, it is possible to rotate the four tetrahedral vectors given in the previous section so that they are aligned along the coordinate axis in the 2D projection, yielding a

stable scheme. This yields

$$n_1 = \frac{1}{\sqrt{3}}\begin{pmatrix} 0 \\ \sqrt{2} \\ 0 \\ 1 \end{pmatrix}, \; n_2 = \frac{1}{\sqrt{3}}\begin{pmatrix} 0 \\ -\sqrt{2} \\ 0 \\ 1 \end{pmatrix}, \; n_3 = \frac{1}{\sqrt{3}}\begin{pmatrix} 0 \\ 0 \\ \sqrt{2} \\ -1 \end{pmatrix}, \; n_4 = \frac{1}{\sqrt{3}}\begin{pmatrix} 0 \\ 0 \\ -\sqrt{2} \\ -1 \end{pmatrix}. \tag{6.72}$$

If any other tetrahedral set of vectors is chosen, then information outside the numerical template is required, causing instability. Note that if the finite difference scheme is made symmetrical so that information from the 'wrong' direction can flow in, then upwinding is lost. This causes either instability, or huge amounts of dispersion which destroy the solution.

Unfortunately, the numerical coincidence of finding an alignment of the basis vectors that just happens to work in the 2D case, does not carry over to the 3D case. Also, this upwinding technique does not work for the second order (two index) moments, where at least nine vectors are required. Improving the numerical algorithm to solve these cases remains an problem yet to be solved.

## 6.7 Emission from a Scattering Torus

We now apply the formulation to calculate the emission from an accretion torus where Thomson scattering dominates over free-free opacity. Free-free emission is assumed to be the dominant emission process. The density, temperature and velocity structure of the tori are the same as those in chapter 5.

The first order approximation for the intensity, requires a single index on the $\mathcal{J}$ tensor in the radiative transfer equation. The calculation of the $\mathcal{J}^\alpha$ is carried out via the finite-difference method described in the previous section, on a $60 \times 60 \times 40$ grid in $r, \theta, \log(E)$ space. A one-sided fourth-order method is used to calculate the derivatives.

Nonlinear advection-reaction equations are notoriously hard to solve numerically

due to the formation of false 'shocks' in the solution. These appear as linear structures along the coordinate axis directions in this particular case. They are caused by large gradients in the emissivity making the boundary condition solver produce unphysical solutions. They appear when the central density is too large, or when the torus is too compact. Other 'sawtooth' instabilities also appear when the numerical scheme itself starts to break down. Overshoot appears in the derivative finite differencing, and this increases exponentially as the simulation proceeds, overwhelming the wanted solution. Fortunately, these problems do not appear for the range of parameters investigated here, where the torus straddles the regimes of being optically thin and optically thick.

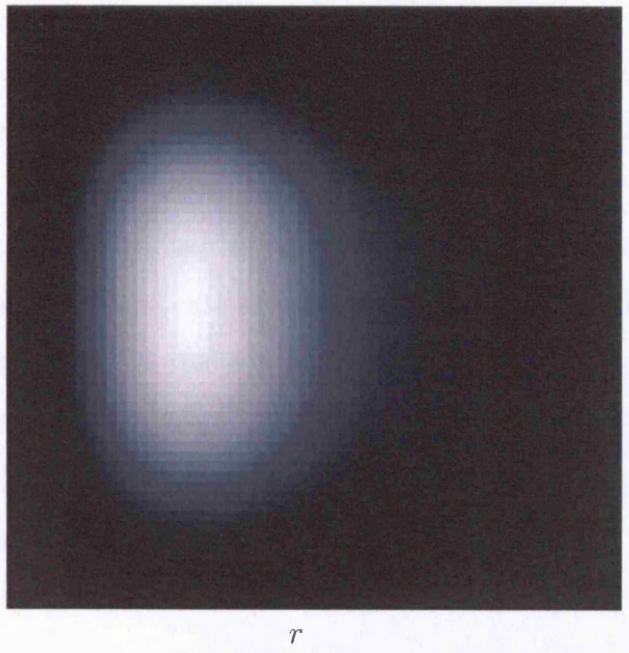


Figure 6.5: Greyscale image of the gas rest-frame averaged intensity $\mathcal{J}_\alpha u^\alpha$ for the median energy in the model. The torus acts like a 'bag of light' trapping the radiation in its centre. Images like this are used to detect numerical instabilities in the radiative moment calculation. The torus used here is the $R_G = 10^{13}$cm one shown in Fig. 6.8.

To ensure numerical stability, the image of emissivity $\mathcal{J}_\alpha u^\alpha$ (as a function of $r$ and $\theta$) is plotted and examined. (Figure. 6.5. shows an example where the solution is stable, i.e. a smooth image with no discontinuities.) A convergence test was also

performed by adjusting the resolution of the grid.

Figures 6.6., 6.7. and 6.8. show surface brightness images of semi-transparent tori where electron scattering is the main source of opacity. The corresponding maximal scattering optical depths are approximately 0.1, 1, and 10 in the three cases.

For realistic parameters for the black hole and torus, if the opacity is purely due to free-free absorption then the torus is optically thin. If scattering is approximated by absorption with the Thomson cross-section as was done in chapter 5, then the radiation field is incorrect. The edges of the torus would have excessive limb darkening, and the high energy photons from the torus interior do not escape. When scattering is treated explicitly such false effects are removed.

Note that the Thomson scattering opacity we used in the transfer equation does not lead to energy redistribution. Unlike Compton scattering, the power-law continuum observed in AGN cannot be reproduced. This could be rectified by using the Compton scattering kernel in the moment formulations presented in §6.1 and §6.2. However, to generalise the case of Thomson scattering to the case of Compton scattering would require the derivation of a covariant Compton scattering kernel, and evaluation of the multidimensional integral for the covariant moments. The additional procedures are conceptually straightforward, in spite of the computational complexity. This generalisation is left for future study.

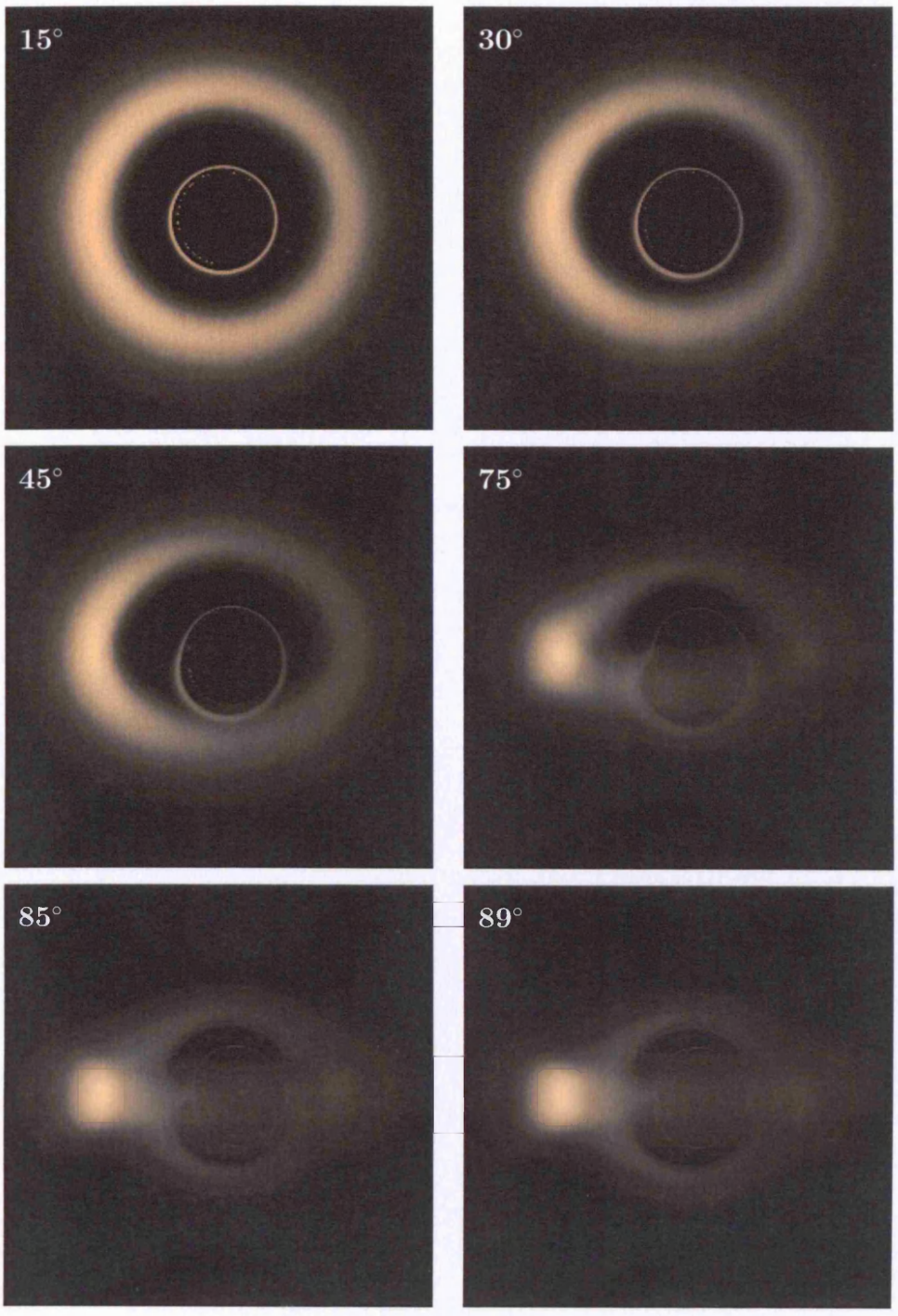


Figure 6.6: Surface brightness images of scattering dominated accretion tori around Kerr black holes viewed at inclination angles of 15°, 30°, 45°, 75°, 85° and 89°. The spin of the black hole $a = 0.998$. The torus is constructed using the velocity law in §4.2. The gravitational radius of the black hole is $10^{11}$ cm. The central number density of the torus is $10^{11}$ cm$^{-3}$, and the ratio of gas to total pressure is $10^{-5}$. Note that due to dynamic range issues, the images have been normalized such that the brightest pixel in each image is the same intensity.

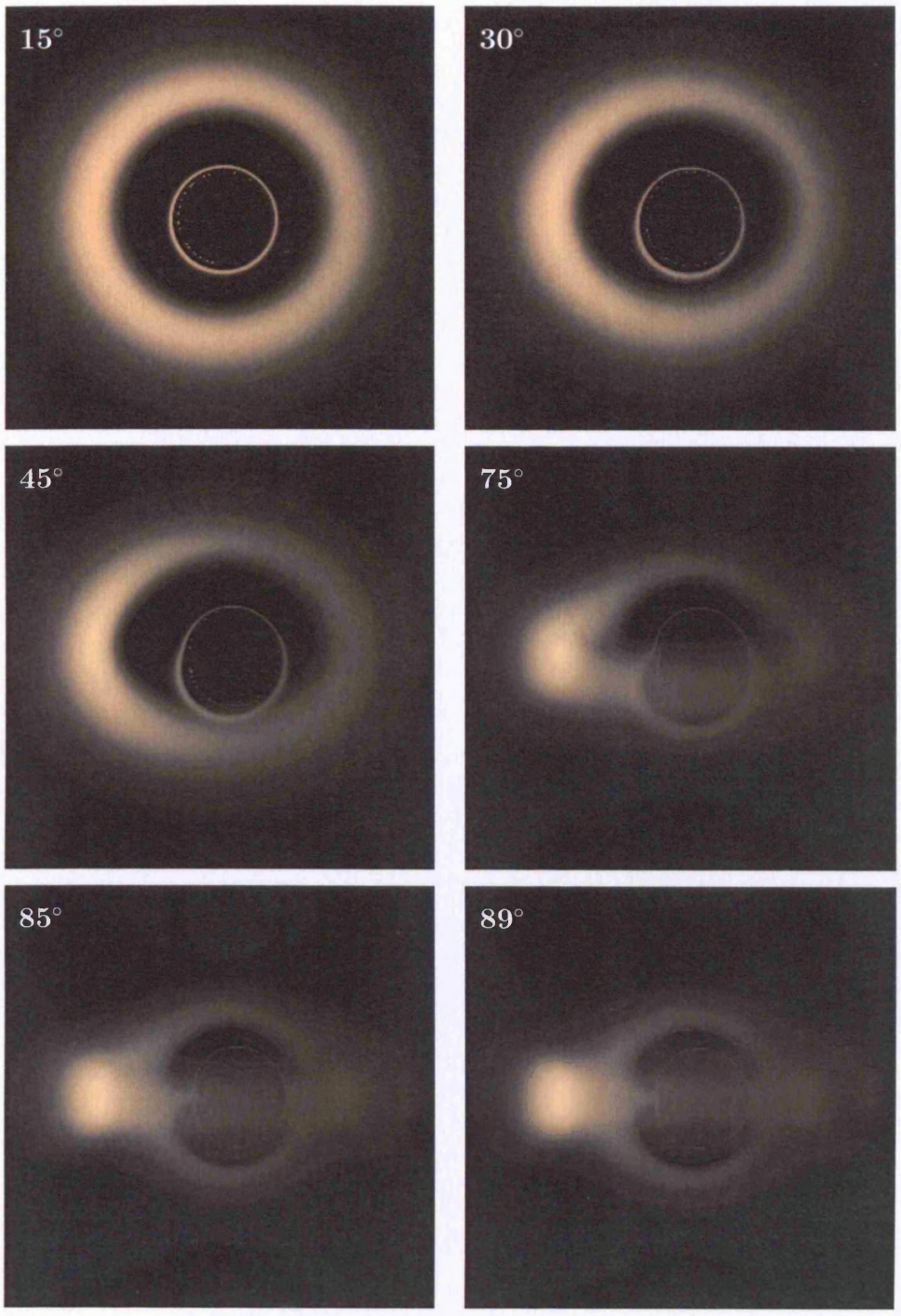


Figure 6.7: Surface brightness images of scattering dominated accretion tori around a Kerr black holes viewed at inclination angles of 15°, 30°, 45°, 75°, 85° and 89°. The spin of the black hole $a = 0.998$. The torus is constructed using the velocity law in §4.2. The gravitational radius of the black hole is $10^{12}$ cm. The central number density of the torus is $10^{11}$ cm$^{-3}$, and the ratio of gas to total pressure is $10^{-5}$. Note that due to dynamic range issues, the images have been normalized such that the brightest pixel in each image is the same intensity.

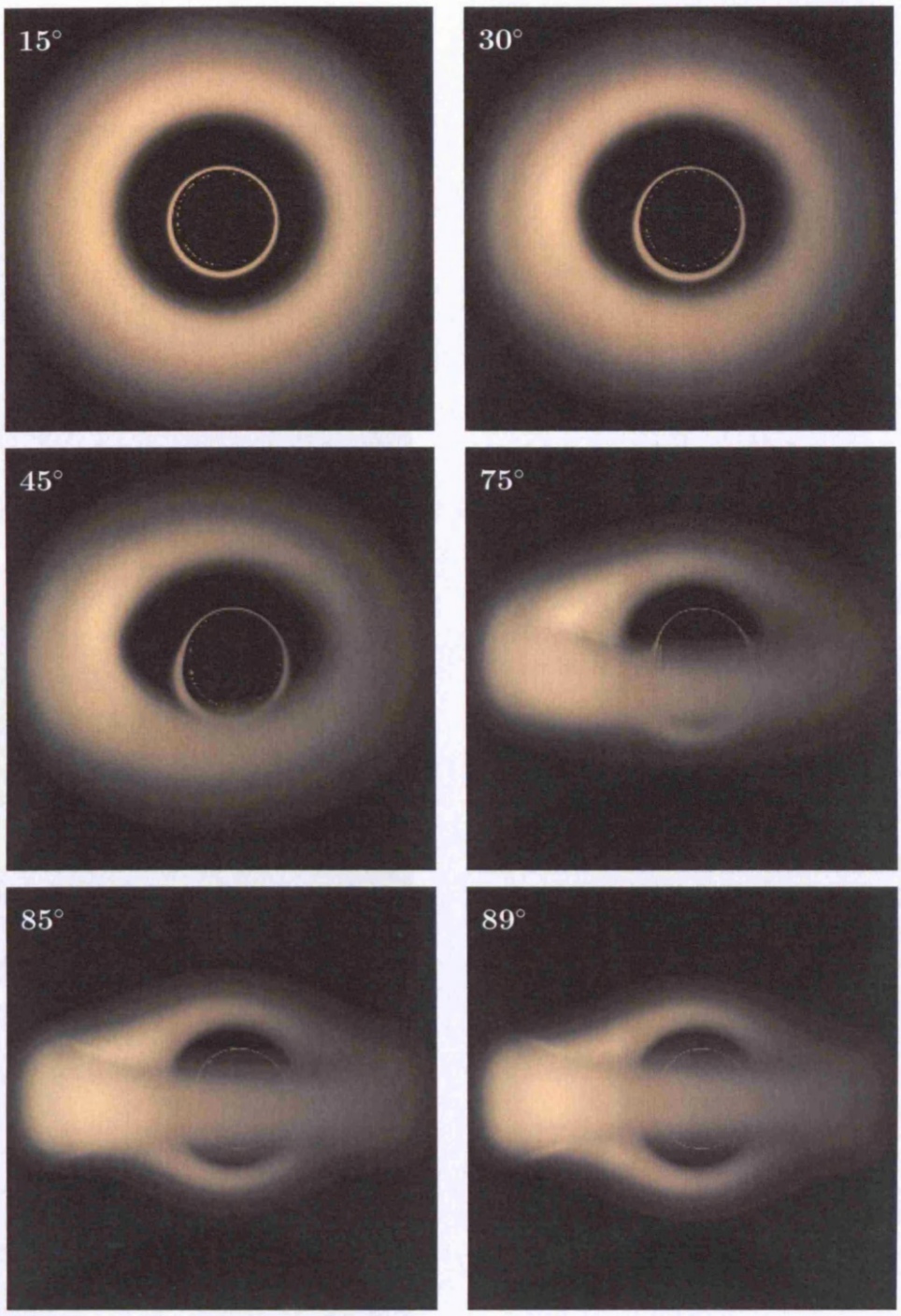


Figure 6.8: Surface brightness images of scattering dominated accretion tori around a Kerr black holes viewed at inclination angles of 15°, 30°, 45°, 75°, 85° and 89°. The spin of the black hole $a = 0.998$. The torus is constructed using the velocity law in §4.2. The gravitational radius of the black hole is $10^{13}$ cm. The central number density of the torus is $10^{11}$ cm$^{-3}$, and the ratio of gas to total pressure is $10^{-5}$. Note that due to dynamic range issues, the images have been normalized such that the brightest pixel in each image is the same intensity.

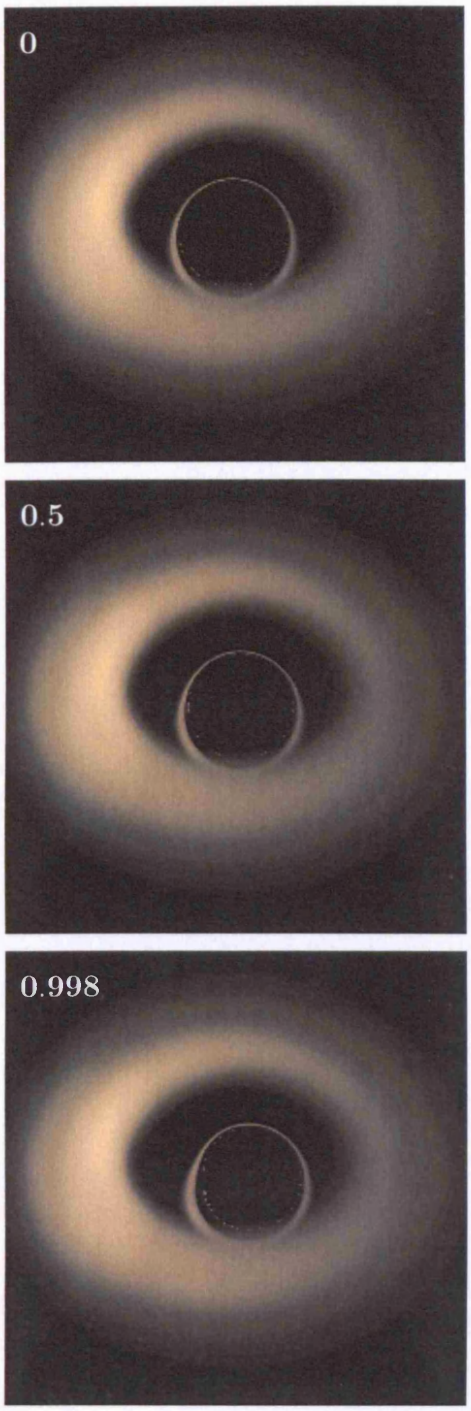


Figure 6.9: Surface brightness images of scattering dominated accretion tori around Kerr black holes viewed at an inclination angle of 45°. The spin of the black hole is $a = 0, 0.5$, and 0.998 (top to bottom). The tori are constructed using the velocity law in §4.2. The gravitational radius of the black hole is $10^{13}$ cm. The central number density of the torus is $10^{11}$ cm$^{-3}$, and the ratio of gas to total pressure is $10^{-5}$. Note that due to dynamic range issues, the images have been normalized such that the brightest pixel in each image is the same intensity.

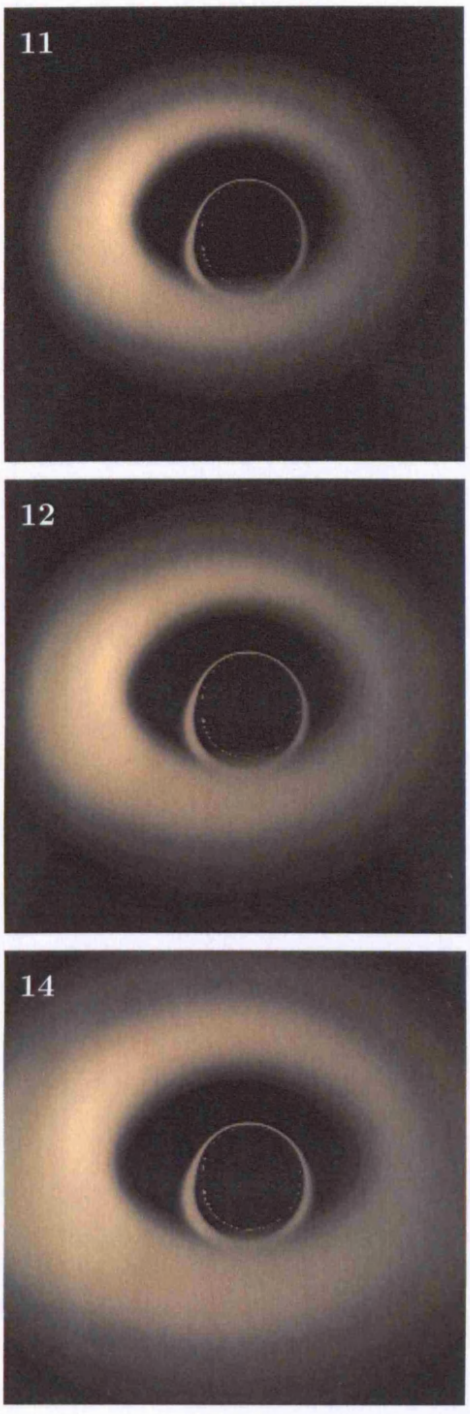


Figure 6.10: Surface brightness images of scattering dominated accretion tori around Kerr black holes viewed at an inclination angle of 45°. The spin of the black hole is $a = 0.998$. The tori are constructed using the velocity law in §4.2. The location of Keplerian motion, $r_{\rm K}$, is 11, 12, and $14R_G$ (top to bottom). The gravitational radius of the black hole is $10^{13}$ cm. The central number density of the tori is $10^{11}$ cm$^{-3}$, and the ratio of gas to total pressure is $10^{-5}$. Note that due to dynamic range issues, the images have been normalized such that the brightest pixel in each image is the same intensity.

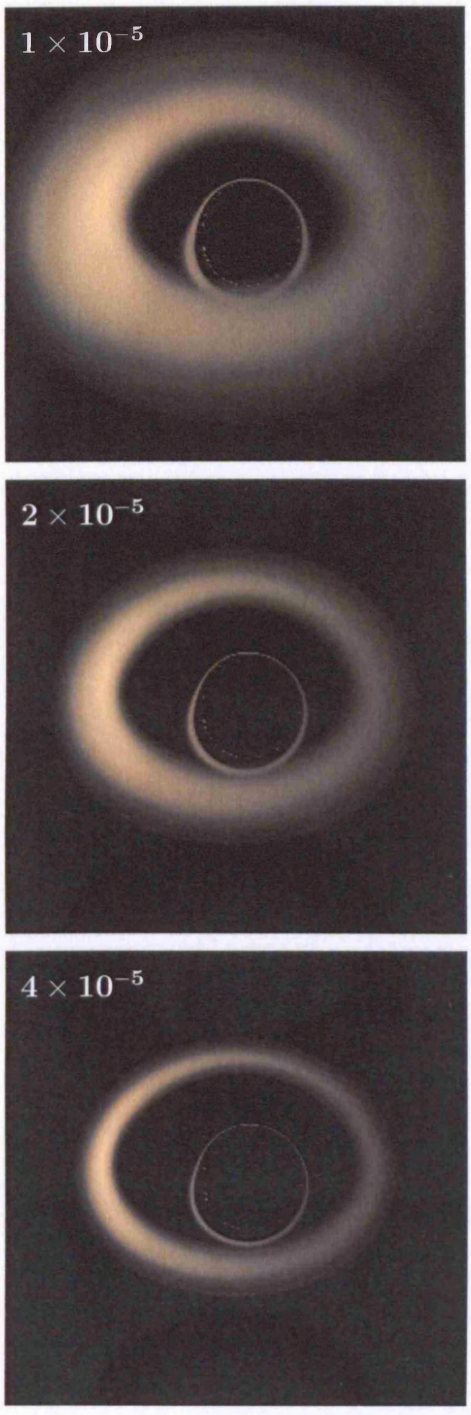


Figure 6.11: Surface brightness images of scattering dominated accretion tori around a Kerr black holes viewed at an inclination angle of 45°. The spin of the black hole is $a = 0.998$. The tori are constructed using the velocity law in §4.2. The ratio of gas to total pressure is $10^{-5}$, $2 \times 10^{-5}$, and $4 \times 10^{-5}$ (top to bottom). The gravitational radius of the black hole is $10^{13}$ cm. The central number density of the torus is $10^{11}\text{cm}^{-3}$. Note that due to dynamic range issues, the images have been normalized such that the brightest pixel in each image is the same intensity.

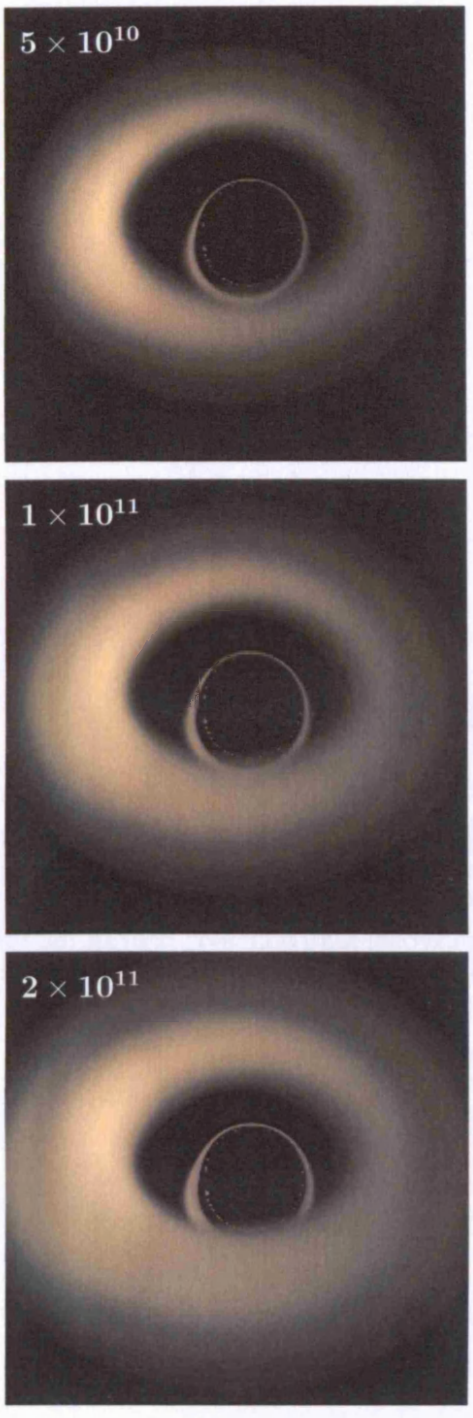


Figure 6.12: Surface brightness images of scattering dominated accretion tori around a Kerr black holes viewed at inclination angle of 45°. The spin of the black hole is $a = 0.998$. The tori are constructed using the velocity law in §4.2. The gravitational radius of the black hole is $10^{13}$ cm. The central number density used is $5 \times 10^{10}$, $10^{11}$, and $2 \times 10^{11}$ cm$^{-3}$ (top to bottom). Note that due to dynamic range issues, the images have been normalized such that the brightest pixel in each image is the same intensity.

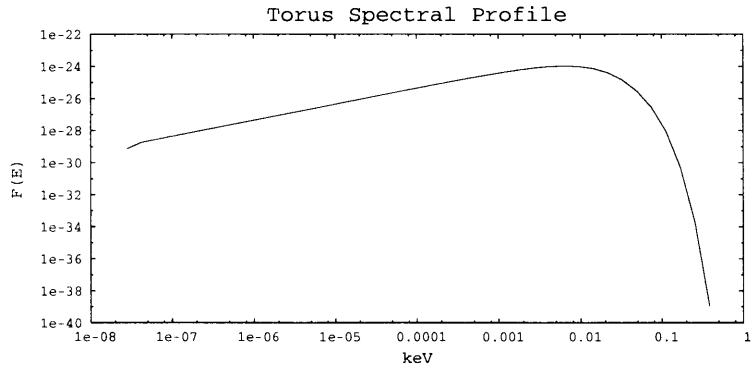


Figure 6.13: Spectrum from an accretion torus around a Kerr black hole with an opacity denominated by thermal free-free emission and electron scattering. The viewing inclination angle is 45°. The angular momentum of the black hole is $a = 0.998$. The torus is constructed using the velocity law in §4.2. The gravitational radius of the black hole is $10^{13}$ cm. The central number density used is $10^{11}$ particles per cubic centimetre.

# Chapter 7

# Conclusion

## 7.1 Equations of Motion

In chapter 2, I derive a covariant radiative transfer formulation. The formulation preserves the same form as the classical radiative transfer equation. The formulation is applicable to investigations of spectral formation in AGN environments where space-time curvature could be important. I also derived the equations of motion of particles under implicit external forces. The equations are used for the construction of accretion disks/tori and for the absorbing clouds model.

The relativistic version of the radiative transfer equation is a generalisation of the classical version: with the inclusion of a Lorentz transformation factor; and replacing the specific intensity and the opacity with the corresponding Lorentz invariant quantities. The ray tracing algorithm works by following individual rays along their paths backwards in time from the observer to the emitter. This is applicable in models where the scattering term is ignorable.

The equations of motion of photons were required to determine the photon trajectory. They were derived from the Euler-Lagrange equation in the Kerr metric. The second order equations for the radial and azimuthal coordinates are used instead of using the first order equations typically used by others. The equations

used in other studies involve squares of the first derivatives, which cause problems in determining the sign around turning points. By using second derivatives, this degeneracy is removed, simplifying the numerical algorithm.

The equations of motion for particles undergoing 'powered orbits' in the Kerr metric are derived. They describe the motion of matter outside the equatorial plane, and are used in modelling tori like those in chapter 4, and in the absorbing clouds model used in chapter 3. A relatively simple analytic expression for the time and azimuthal components of the four-velocity of the matter was derived. The light circularization radius and the radius of marginal stability for the pressure supported matter was calculated. These are the critical surfaces which I use to determine the inner boundary of the accretion tori.

## 7.2 Accretion Disks

In chapter 3, I construct models of geometrically thin accretion disks, generate energy shift images and calculate the profile of their emission lines. I reproduce the previous calculations of other groups using the same setting, namely the asymmetric double horn profile. I consider a more complicated setting with absorption as well as emission. The absorption is due to a distribution of virialized clouds. The resonant absorption condition is derived analytically. Absorbed continuum and line spectra are presented.

I derived an analytic formula for the line absorption from a relativistic gas. A model of line-of-sight absorptive clouds which are thermally cold and kinematically hot is used. The bulk velocity of the clouds matches that of the disk at its surface.

The higher order images are important in determining the line shape at high inclinations. The indirect light can fill in the central depression in the double-peaked profile from the direct image, and may result in extra peaks around the line rest energies. When the accretion disk is optically thick, the higher order images are partially obscured by the direct image at all inclination angles. The regions of

the higher order images with the highest red and blue shifts are obscured, and thus their spectral contribution is mainly around the line rest energy.

The absorbing clouds tended to remove flux from around the line rest energy. This was because the clouds are far from the black hole and lower velocities compared to the flow in the accretion disk. The absorption profile was, however, asymmetric. Its broadening is due to the bulk motion of the clouds, and their kinematic dispersion.

## 7.3 Accretion Tori

In chapter 4, I construct a model for optically thick accretion tori. The emission surface is generated using the four-acceleration which is calculated from a parametric velocity field. A ray tracing algorithm is used to calculate the emission lines.

The line profiles from opaque tori differ from those of traditional thin disk models. Due to self-obscuration, the inner surface of the torus is invisible to observers at high inclination angles. At such orientations, line emission from the fastest moving gas is unobservable, curtailing the red and blue wings of the line profile. The result is a relatively featureless broad hump centred roughly on the line rest frequency.

The geometry together with the absorption as discussed in chapter 3 complicate the interpretation of line emission from AGN. A double peaked line may be due to a thin disk. Equally, it may be due to an accretion torus in which absorption at the line rest frequency produces a central dip. The characteristic red wing of the line profile from thin accretion disks depends strongly on the location of their inner edge.

A change in the red wing may result in an incorrect determination of the black hole spin. (Assuming that the inner edge of the accretion disk is at the marginally stable orbit, which is often done elsewhere, as well as being the assumption made in this thesis). A change in the sharp cut-off in the blue wing may seriously affect calculations of the inclination angle of the disk/torus. Diagnosis of accretion onto

black holes using X-ray spectra is not at all straightforward. If the basic parameters of the system cannot be determined reliably, it is more difficult than popularly envisaged to use the super-massive black holes in AGN as tests of general relativity itself.

## 7.4 Emission from Semi-Transparent Tori

In chapter 5, I construct model structures for accretion tori. The local density and temperature are calculated using the equation of state together with the hydrodynamic equations. I present two illustrative radiative transfer calculations. In the first case, I consider only line emission. Surface brightness images of the tori are generated. The line profiles are not identical with those from opaque accretion tori because there is no self-obscuration of the emission region. The lines, however, show some similarity with the lines from thin disks. I also calculate emission from two adjacent lines, Fe K$\alpha$ and Fe K$\beta$, as an illustration. While the two lines are still separable, the wings of the two lines are entangled.

The images of the tori show the differences between the optically thick and thin models. The optically thin models are transparent, and the higher order images are not obscured. At high inclination angles, the image orders merge, producing a complicated set of rings.

The line profiles produced by the semi-transparent tori are different from the disk models, and also from the solid torus models of chapter 4. The observed emission comes from throughout the whole volume of the torus. This means that there is no self-obscuration like what happens in the 'solid' models. This adds much more flux in the red and blue wings of the line profiles since the inner part of the torus is visible. The resulting line profiles look more like those from disks, and only show spectral 'humps' at low inclination.

The addition of the iron K$\beta$ line to the K$\alpha$ line added an extra peak to the profile. The blue peak is supplemented by a smaller bump on its shoulder. The red

wing along with the rest of the line stays much the same. The relativistic Doppler smearing is not strong enough to blend everything totally together, and the extra line stays distinct at all inclinations.

I calculate the line the presence of a continuum consisting of a thermal free-free component and a power-law component. I also include a grey absorber with an absorption coefficient given by the Thomson cross-section. Surface brightness images of the torus are generated, and spectra are calculated. Limb darkening effects can be seen in the images. The tori have similar appearance to the opaque tori, except the boundary is now fuzzy.

The continuum components are not affected by changing the viewing inclination, while the lines show obvious broadening and shifts. The power law is unaffected by the relativistic Doppler smearing and changes in viewing inclination. The Bremsstrahlung part of the spectrum was affected slightly, depending on inclination angle.

The high inclination tori show how the foreground atmosphere can absorb flux from the brighter Doppler-shifted gas behind. The self-obscuration is evident, and the higher order image rings tend to be small, or hidden behind the torus.

## 7.5 Relativistic Moment Formulation

In chapter 6, I derive a new moment method to solve covariant radiative transfer with scattering. The advantages of my formulation are (i) moments are not required to be evaluated explicitly, which greatly simplifies the computation. (ii) the physics is transparent and the equations can be compared with the classical form. The first order moment equation is equivalent to the Eddington approximation as in classical radiative transfer. Higher order moment methods are obtained directly. I propose a numerical scheme to solve the first order moment equation using a four-stream approximation. (c.f. the two-stream approximation in the classical Eddington approximation). I construct appropriate boundary conditions required

to solve the radiative transfer equation.

The moment method is simpler than the moment method suggested by Thorne (1981). I redefine the moments and express the radiative transfer equation in moment form. The kernel of the integration, i.e. the scattering term, is written in terms of sums of moments. This converts the integro-differential equation of radiative transfer into a system of partial differential equations, which is solvable.

To verify my moment formulation, I re-derive Eddington's approximation, and the radiative diffusion equation in the limit of flat space-time. This was done by substituting four unit-vectors for the $n^\alpha$ to obtain four equations for the $\mathcal{J}^\alpha$ of the first order moment truncated equation. This four-stream approximation yields the radiative diffusion equation in terms of $\mathcal{J}^0$, which is proportional to the isotropic intensity.

Using the partial differential equations for the first order truncated moments, I then created a two dimensional numerical scheme for calculations in the Kerr metric. It is a fourth-order implicit upwind scheme, and converges very rapidly. The only problems occur when there are extremely large optical depths, when the scheme would become oscillatory. However, for the parameters relevant for tori around AGN, this was not apparent.

## 7.6 Tori with Scattering

I generate surface brightness images of tori dominated by scattering. Cases with scattering depth from 0.1 to 10 are calculated to demonstrate the validity of the formulation. At first glance, the appearance of the torus is similar to those with the grey absorption, but the limb effects of the scattering tori are very different to the absorbing tori.

Using the radiation field from the moment formulation, I calculate the amount of light scattered into a given line of sight. Thus the scattering term can be correctly accounted for in the ray tracing method. I use a combined moment and ray tracing

method to construct a scheme which can handle emission, absorption and scattering in curved space-time. With that code I investigate the inner torus of AGN including the dominant radiative processes correctly.

The results of this are a combination of those from the optically thick and optically thin tori of chapter 5. However, instead of using the fake absorptive opacity, the correct scattering opacity is used. The difference between the two is that scattering doesn't 'destroy' the light, it just re-directs it. The flux from the interior of the torus escapes, albeit modified on its way out.

Using scattering instead of absorption alters the limb of the tori. Instead of being effectively an absorbing atmosphere on top of an emitting torus, the limb also scatters light into the line of sight. The difference between the limb and the rest of the image is due to the effective path length into the medium, and the stratified temperature in the torus. The perpendicular rays penetrate deeper into the torus where they sample hotter plasma, compared to the tangential rays which only sample the cooler surface gas.

The characteristic scale of the problem is changed by altering the mass of the black hole. The range in optical depths investigated, covered the optically thin through to very optically thick regimes. As can be seen, the numerical scheme developed from the relativistic moment method works well in all regimes.

## 7.7 Overview

I consider the highlight of this thesis the construction of a new moment formulation for radiative transfer equation. The formulation is simple, where increasing the computational order requires only an increase in the number of indexs in the moment tensors. Applying this formulation, a numerical scheme has been constructed for radiative transfer in the Kerr space-time. Previous schemes have been limited to spherically symmetric problems in practise, or to low order due to incorrectly using the stress-energy and flux tensors as approximations for the radiation field angular

distribution (see Mihalas & Mihalas 1984). Compared to previous methods for general relativistic radiative transfer, this is a major advance.

The moment formulation works very well when the optical depths are high, and the radiation field is nearly isotropic. The ray tracing formation which I use in other chapters works well in the free-streaming regime, where the optical depths are low. By combining the methods, we have a "complete" numerical scheme which contains the best of both.

Using this new formulation I propose, we can calculate emission from scattering dominated accretion disks in AGN. At present, a Thomson scattering kernel is used. The generalisation to include a Compton scattering kernel will allow us to produce proper continuum spectra from which it will be possible to make direct comparisons with observation. I conclude by stating that now we have a proper general relativistic radiative transfer treatment. What remains is the addition of proper atomic processes, which determine the terms on the right hand side of the equation. Further challenges include the treatment of polarisation, and to generalise to the case where the geometric optics approximation breaks down.

# Acknowledgements

Firstly I would like to acknowledge my supervisor, Dr Kinwah Wu, for being a steady hand and preventing me from presenting results before they had been fully checked. I would like to thank Dr Mat Page, for giving the observational point of view, and making sure my knowledge of AGN was up to scratch. I thank Dr Silvia Zane for lending me her thesis so I could try to understand the complexities of doing radiative transfer with Comptonization.

I need to thank the UCL graduate school for giving me a scholarship, otherwise this work would not have taken place. I also need to thank the UK government for giving me an overseas research student scholarship which allowed me to afford studying for a PhD in the UK.

I would like to thank my fellow students, you know who you are, especially those who have lived in the student flats during my long stay in room 007. I also have to mention the rest of the astro-solar lunch group, and that the social scene here has been wonderful.

Finally, I would like to thank Dr Curtis Saxton for taking the time to carefully read through my thesis, and especially looking at all the equations for errors. Also I would like to thank Dr Alex Blustin for providing hours of entertainment whilst at the same time being hyperbolic.

Last, but not least, I would like to thank my family for not worrying too much about me being on the other side of the world. I thank them for letting me have the time I have needed to get this work done.

# Bibliography


Abramowicz, M., Jaroszynski, M., Sikora, M., 1978, A&A, **62**, 221

Abramowicz, M., 2004, "Growing Black Holes", Eds. Merloni, A., Nayakshin, S., Sunyaev, R., ESO Astrophysics Symposia Series, Springer-Verlag, Berlin; `astro-ph/0411185`

Bao, G., 1992, A&A, **257**, 594

Bao, G., Hadrava, P., & Østgaard, E., 1994, ApJ, **435**, 55

Balbus, S. A., Hawley, J. F., 1991, ApJ, **376**, 214

Bardeen, J. M., Press, W. H., & Teukolsky, S., 1972, ApJ, **178**, 347

Baschek, B., Efimov, G. V., von Waldenfels, W. & Wehrse, R., 1997, A&A, **317**, 630

Blandford, R. D, Begelman, M. C., 2003, MNRAS, **349**, 68

Blustin, A. J., Page, M. J., Fuerst, S. V., Branduardi-Raymont, G., Ashton, C. E., 2005, A&A, **431**, 111

Bowers, R., & Deeming, T., 1984, "Astrophysics II", Boston: Jones and Barlett Publishers.

Branduardi-Raymont, G.,Sako, M., Kahn, S. M., Brinkman, A. C., Kaastra, J. S., Page, M. J., 2001, A&A, **365**, 140

Bromley, B. C., Chen, K., & Miller, W. A., 1997, ApJ, **475**, 57

Cadez, A., Fanton, C., & Calvani, M., 1998, New Astronomy, **3**, 647

Cadez, A., Brajnik, M., Comboc, A., Calvani, M., & Fanton, C., 2003, A&A, **403**, 29

Carter, B., 1968, Phys. Rev., **174**, 1559

Chakrabarti, S. K., 2002, Frontiers in Astrophysics, Ed. S.K. Chakrabarti, Allied Publishers, p. 145; `astro-ph/0402562`

Cunningham, C. T., 1975, ApJ, **202**, 788

Cunningham, C. T., 1976, ApJ, **208**, 534

Dabrowski, Y., Fabian, A. C., Iwasawa, K., Lasenby, A. N., & Reynolds, C. S., 1997, MNRAS, **288**, L11

De Villiers, J-P., Hawley, J. F., 2002, ApJ, **577**, 866

De Villiers, J-P., Hawley, J. F., 2003, ApJ, **592**, 1060

De Villiers, J-P., Hawley, J. F., Krolik, J. H., Hirose, S., 2005, ApJ, **620**, 878

Fabian, A. C., Rees, M. J., Stella, L., & White, N. E., 1989, MNRAS, **238**, 729

Fabian, A. C., Iwasawa, K., Reynolds, C. S., & Young, A. J., 2000, PASP, **112**, 1145

Fanton, C., Calvani, M., de Felice, F., & Cadez, A., 1997, PASJ, **49**, 159

Frank, J., King, A., Raine, D., 1985, "Accretion Power in Astrophysics", Cambridge University Press, Cambridge.

Fuerst, S. V., Wu, K., 2004, A&A, **424**, 733

Gammie, C. F., 2004, ApJ, **614**, 309

Gerbal, D., & Pelat, D., 1981, A&A, **95**, 18

Hawley, J. F., & Balbus, S. A., 2002, ApJ, **573**, 738

Hirose, S., Krolik, J. H., De Villiers, J-P., Hawley, J. F., 2004, ApJ, **606**, 1083

Hölzer, G., Fritsch, M., Deutsch, M., Härtwig, J., Förster, E., 1997, Phys Rev. A,

**56**, 4554

Kembhavi, A. K., Navliker, J. V., 1999, "Quasars and Active Galactic Nuclei", Cambridge University Press, Cambridge

Koide, S., 2003, Phys. Review D, **67**, 104010

Kojima, Y., 1986, Prog. Theor. Phys, **75**, 1464

Kojima, Y., 1991, MNRAS, **250**, 629

Kozlowski, M., Jaroszynski, M., Abramowicz, M., 1978, A&A, **63**, 209

Krolik, J. H., 1999, "Active Galactic Nuclei", Princeton University Press, Chichester.

Krolik, J. H., Hawley, J. F., 2002, ApJ, **573**, 754

Krolik, J. H., Hawley, J. F., Hirose, S., 2005, ApJ, **622**, 1008

Laor, A., 1991, ApJ, **376**, 90

Lee, J. C., Ogle, P. M., Canizares, C. R., Marshall, H. L., Schulz, N. S., Morales, R., Fabian, A. C., Iwasawa, K., 2001, ApJ, **554**, L13

Lindquist, R., 1966, Annals of Physics, **37**, 487

Marklund, M., 2005, J. Phys. A: Math. Gen, **38**, 4265

Maruta, D., Kaburaki, O., 2003, ApJ, **593**, 85

Matt, G., Perola, G. C., & Stella, L., 1993, A&A, **267**, 643

Mihalas, D., 1978, "Stellar Atmospheres" 2nd Edition, W. H. Freeman and Company, San Francisco

Mihalas, D., 1980, ApJ, **237**, 574

Mihalas, D., Mihalas, B. W., 1984, "Foundations of Radiation Hydrodynamics", Oxford University Press, Oxford.

Misner, C. W., Thorne, K. S., & Wheeler, J. A., 1970, Gravitation, W. H. Freeman,

San Francisco

Nandra, K., George, I. M., Mushotzky, R. F., Turner, T. J., Yaqoob, T., 1997, ApJ, **488**, L91

Nobili, L., Turolla, R., & Zampieri, L., 1991, ApJ, **383**, 250

Paczynski, B., 1998, Acta Astron., **48**, 667

Pariev, V. I., & Bromley, B. C., 1998, ApJ, **508**, 590

Park, M., 1990, ApJ, **354**, 64

Peraiah, A., 2002, "An Introduction to Radiative Transfer", Cambridge University Press, Cambridge

Pozdniakov, L. A., Sobol, I. M., Sunyaev, R. A., 1983, A&Sp.Phy.Rev., **2**, 189

Press, W. H., Teukolsky, S. A., Vetterling, W. T., & Flannery, B. P. 1992, "Numerical Recipes in Fortran, 2nd Ed.", Cambridge University Press, Cambridge

Reynolds, C. S., Young, A. J., Begelman, M. C., & Fabian, A. C., 1999, ApJ, **514**, 164

Ruszkowski, M., & Fabian, A. C., 2000, MNRAS, **315**, 223

Rybicki, G. B., & Lightman, A. P., 1979, "Radiative Processes in Astrophysics", Wiley, New York

Sako, M., Kahn, S. M., Branduardi-Raymont, G., Kaastra, J. S., Brinkman, A. C., Page, M. J., Behar, E., Paerels, F., Kinkhabwala, A., Liedahl, D. A., Herder, J. W., 2003, ApJ, **596**, 114

Salmeron, R., Wardle, M., 2004, Ap&SS, **292**,451

Shakura, N.I., Sunyaev, R.A., 1973, A&A, **24**, 337

Smak, J., 1969, Acta Astronomica, **19**, 155

Stella, L., 1990, Nature, **344**, 747

Sunyaev, R.A., Titarchuk, L. G., 1980, A&A, **86**, 121

Tanaka, Y., *et al.* 1995, Nature, **375**, 659

Thorne, K. S., 1981, MNRAS, **194**, 439

Usui, F., Nishida, S., Eriguchi, Y., 1998, MNRAS, **301**, 721

Viergutz, S. U., 1993, A&A, **272**, 355

Zane, S., Turolla, R., Nobili, L., & Erna, M., 1996, ApJ, **466**, 871